Cross-scale interactions and turbulent cascades in the North Atlantic Ocean

Adekunle Ajayi

THÈSE

Pour obtenir le grade de

DOCTEUR DE L'UNIVERSITÉ GRENOBLE ALPES

Spécialité : Océan, Atmosphère, Hydrologie (CEOAH)

Arrêté ministériel : 25 mai 2016

Présentée par

Adekunle AJAYI

Thèse dirigée par **Julien LE SOMMER**, Chargé de Recherche

préparée au sein du **Laboratoire Institut des Géosciences de l'Environnement**
dans **l'École Doctorale Terre, Univers, Environnement**

Interactions d'échelles et cascades turbulentes dans l'océan atlantique nord

Cross-scale interactions and turbulent cascades in the North Atlantic Ocean

Thèse soutenue publiquement le **13 janvier 2020**,
devant le jury composé de :

Monsieur JULIEN LE SOMMER
CHARGE DE RECHERCHE CNRS, CNRS DELEGATION ALPES, Directeur de thèse
Madame ANNE-MARIE TREGUIER
DIRECTEUR DE RECHERCHES CNRS, CNRS DELEGATION BRETAGNE PAYS DE LOIRE, Rapporteur
Madame ROSEMARY MORROW
PHYSICIENNE, OBSERVATOIRE MIDI-PYRENEES, Rapporteur
Monsieur ERIC CHASSIGNET
PROFESSEUR, UNIVERSITE D'ETAT - FLORIDE - ETATS UNIS, Examinateur
Monsieur JONATHAN GULA
MAITRE DE CONFERENCES, UNIVERSITE DE BRETAGNE OCCIDENTALE, Examinateur
Madame CHANTAL STAQUET
PROFESSEUR DES UNIVERSITES, UNIVERSITE GRENOBLE ALPES, Président

Contents

Chapter 1

Introduction

Contents

1.1 Kinetic energy distribution and cross-scale exchanges in the ocean

1.1.1 Oceanic kinetic energy

The ocean is a large body of water that covers approximately 70% of the planet Earth. Density stratification and the rotation of the Earth makes the ocean behaves differently compared to other bodies of fluid. The ocean is an integral part of the climate system. Climate change has been affirmed to be a direct consequence of anthropogenic carbon emission which is associated with human activities. 30% of this anthropogenic CO_2 is absorbed by the ocean. Also, the ocean absorbs most of the excess heat from greenhouse gas emissions, leading to a rise in ocean temperature. Climate projections are made based on numerical models that have an ocean component. So, better climate projection requires an ocean component that truly captures the properties and dynamics of the ocean.

The ocean is constantly in motion with most of its kinetic energy coming from the winds. This injection of wind energy at the surface has to be equilibrated by mixing and dissipation in order to have a statistically balanced ocean. About 10% of this energy is dissipated within the upper ocean (Ferrari and Wunsch, 2009), thereby leaving a gap as to how and where the remaining energy is dissipated. Mixing at small-scale can affect the uptake of heat and anthropogenic CO_2 by the ocean (Crueger et al., 2008). It can as well impact the meridional overturning circulation and the global biogeochemical cycle of the ocean. Therefore, understanding mixing and dissipation in the ocean is key for improving our knowledge of ocean circulation, ocean model development and thereby improving climate projections. The accurate representation of mixing in ocean (and climate) model is currently still a challenge for numerical ocean modelers. Oceanic mixing and dissipation is a direct consequence of scale interaction in the ocean that spans from microscale $O(1m)$ to large-scales $O(1000km)$. In fact, mixing and dissipation arise from the kinetic energy exchanges among different scales of motions. In summary, to better understand mixing and dissipation, we need to comprehend how kinetic energy is exchanged and redistributed in the ocean.

Over the years, much effort has been dedicated to understanding how kinetic energy is distributed in the ocean. At first glance, the partition of energy among different spatial (temporal) scale can be obtained through the wavenumber (frequency) spectral analysis of kinetic energy. The kinetic energy spectra in the frequency domain (Figure 1.1) separates the ocean into balanced motions ($< f$) (dominated by geostrophic eddies) and higher-frequency unbalanced motions ($> f$) (dominated by internal waves) where f is the Coriolis frequency. Both frequencies regime are

characterized by a power-law σ^{-r} where r is an empirical constant and σ is a radian frequency. In particular, frequency band $f < \sigma < N$ are controlled by gravity waves while $\sigma > N$ (N is the stratification frequency) are thought to be dominated primarily by small-scale turbulent motions resulting from breaking of internal waves. This qualitative separation of oceanic motion is consistent throughout the world ocean.

On the other hand, in the wavenumber domain, the kinetic energy spectrum still follows a power-law (k^{-r}) but without the distinctive feature seen in the frequency spectrum. In the wavenumber spectra, there is a peak of energy at the mesoscale and this energy generally decreases with wavenumber. Information from these two independent spectra has over the years provide a measure of how energy is distributed in the ocean. A joint frequency-wavenumber spectrum appears to be a more accurate representation of the variance of different scales of oceanic motions in the kinetic energy spectrum. Until recently, this was practically impossible due to the heavy computation this kind of analysis requires. Results based on this kind of spectral analysis (Figure 1.2) show that ocean kinetic energy is mostly concentrated at the geostrophically [1] balanced mesoscale motions.

1.1.2 Geostrophic kinetic energy

The kinetic energy spectrum predicts that most of the ocean kinetic energy is contained in geostrophic mesoscale motions with sub-inertial frequency and spatial scale of the order of $\sim$ 100km. The dominance of kinetic energy at the oceanic mesoscale was first documented in the early 1970s from the mooring and ship-going observations in the Western North Atlantic (Hua et al., 1986). A full characterization of the properties and distribution of the mesoscale motion has only been possible in the past 20 years when satellite altimeters provided the first global pictures of the geostrophic circulation at the ocean surface. These class of motions is associated with strong mean flow features and energetic coherent structures, also known as mesoscale eddies. Mesoscale eddies are mostly generated by baroclinic instability (Gill et al., 1974; Stammer and Böning, 1992), meandering of strong ocean currents and are by far the largest reservoir of ocean kinetic energy, accounting for over 90% of the ocean kinetic energy (Wunsch, 2007). They are more densely populated in major ocean currents such as, the Gulf stream, the Kuroshio currents and are pronounced in the Southern Ocean where they delineate the Antartic Circumpolar Current. They are characterized by small Rossby ($Ro = U/fl$) and Froude ($Fr = U/Nh$) where U is a characteristic horizontal velocity scale, f is the local Coriolis frequency for Earths rotation, N is stratification frequency, l is the horizontal length scale and h is the vertical length scale. Mesoscale eddies have a spatial scale that mostly follows the

[1] A geostrophic current is an oceanic current in which the pressure gradient force is balanced by the Coriolis force.

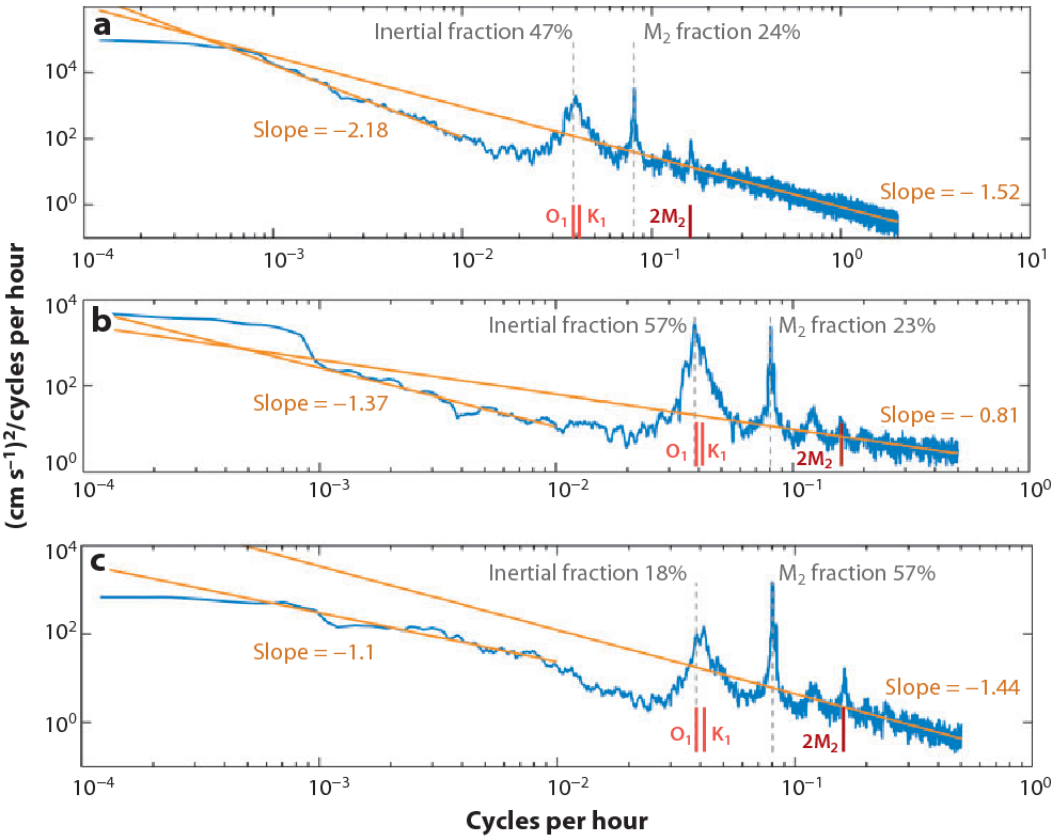

Figure 1.1: From Ferrari and Wunsch (2009). Kinetic energy spectral estimates for instruments on a mooring over the Mid-Atlantic Ridge near 27N (Fu et al. 1982). The inertial, principal lunar semidiurnal M2, and diurnal O1, K1 tidal peaks are marked, along with the percentage of kinetic energy in them and the kinetic energy lying between f and the highest frequency estimate. Least-squares power-law fits for periods between 10 and 2 h and for periods lying between 100 and 1000 h are shown. The approximate percentage of the energy of the internal wave band lying in the inertial peak and the M2 peak is noted. In most records, the peak centered near f is broader and higher than the one appearing at the M2 frequency. When f is close to the diurnal frequency, it is also close to one-half the frequency of M2, when the parametric subharmonic instability can operate. Some spectra show the first overtone, 2 M2 of the semidiurnal tide. Instrument at (a) 128 m, (b) 1500 m, and (c) 3900 m (near the bottom). The geostrophic eddy band is greatly reduced in energy near the bottom, as is the inertial band, presumably because of the proximity of steep topography. Note the differing axis scales.

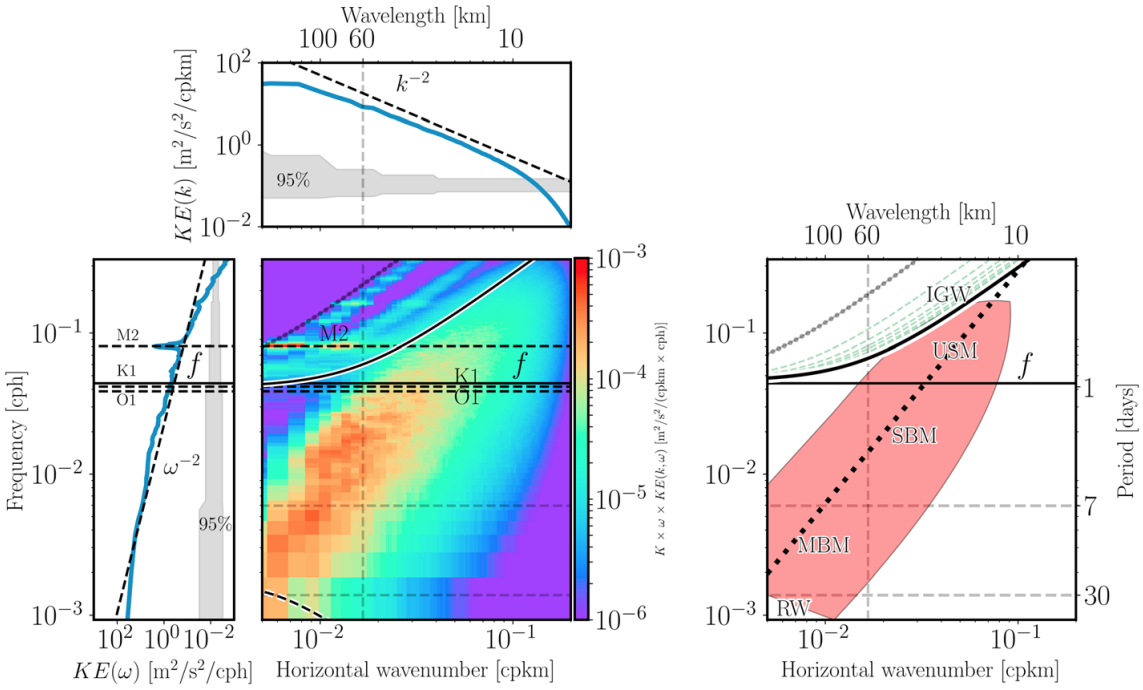

Figure 1.2: From Torres et al. (2018). Frequency-wave number spectra of KE (KE $[m^2/s^2]$) corresponding to the Kuroshio-Extension, during the January- February-March season. The spectrum is multiplied by k and ω, indicating the spectrum is variance preserved. The right panel is the frequency spectrum; the upper middle panel is the wavenumber spectrum; the bottom middle panel is the frequency-wave number spectrum; the left panel is the schematic frequency-wave number spectrum. The schematic spectrum displays the multiple dynamical regimes: RW stands for Rossby waves, MBM for mesoscale balanced motions, SBM for submesoscale balanced motions, USM for unbalanced submesoscale motions, and IGW for internal gravity waves. Additionally, the schematic spectrum shows the dispersion relation of the first ten baroclinic modes: mode-1 in gray dotted line, mode-2 to mode-9 green dashed lines, and mode-10 in black. Finally, the nondispersive line, $\omega - ck = 0$, is drawn with c corresponding to an eddy speed of 8.5 km/day (∼10 m/s). Gray band in right and upper panels denote the 95% confidence intervals.

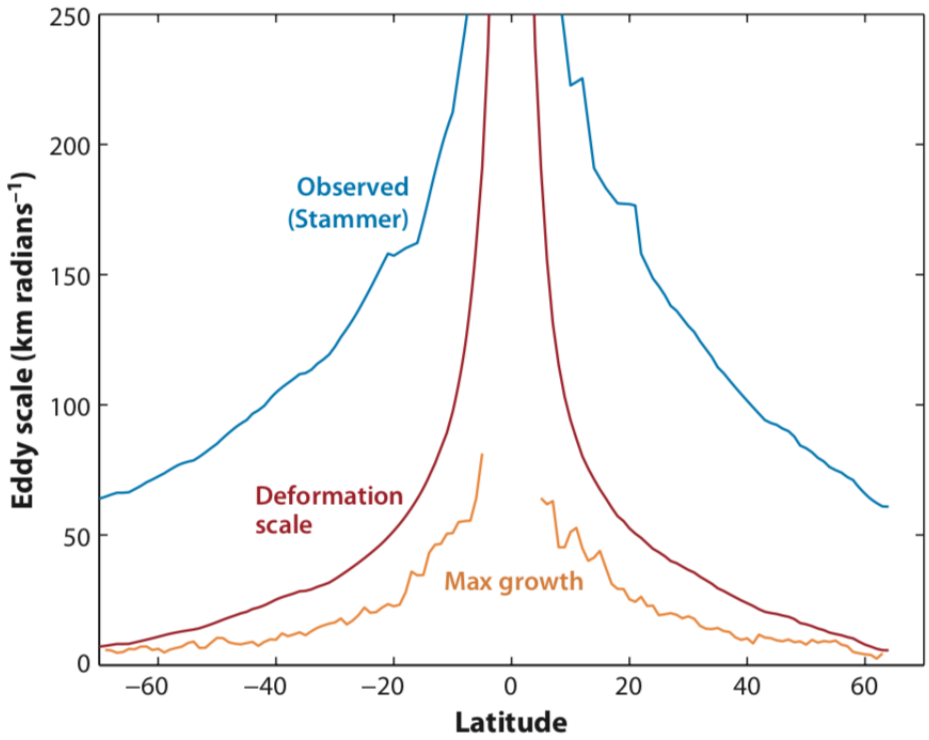

Figure 1.3: From Ferrari and Wunsch (2009) Zonally averaged scales (in kilometers) of the maximum growth rate of baroclinic instability of the main thermocline estimated from hydrography (Smith 2007), the spectral peak of eddy kinetic energy from the analysis of satellite observations by Stammer (1997), and the first deformation radius estimated from Levitus climatology (Chelton et al., 1998). The estimate of the spectral peak of eddy kinetic energy is uncertain. First, the altimetric signal is dominated by noise at scales below 10050 km, and the spectral energy is largest at the smallest wave numbers. Hence the spectral peak estimate is not independent of the choice of filter. Second, the spectral peak is evident only in a small fraction of satellite tracks that cross well-defined coherent eddy structures: The spectral peak does not characterize the background eddykinetic energy spectrum, which is close to white.

estimate of the Rossby radius of deformation. Results from direct observation of eddy size and the theoretical predictions from linear theory confirm this (Figure 1.3).

Despite being the largest reservoir of kinetic energy, geostrophic eddies do not contribute to oceanic vertical mixing. This is because baroclinic instability that generates these eddies results in the extraction of potential and kinetic energy from large scale circulation (Ferrari and Wunsch, 2009). This extraction of potential energy, in fact, limit the chances of vertical mixing, a process that requires potential energy. However, the dissipation of eddies by interacting with bottom topography can sometimes produce mixing (Molemaker et al., 2005).

1.1.3 Sinks and cascades of geostrophic kinetic energy

The rotation of the earth and density stratification strongly suppress vertical velocities for geostrophic eddies, and these motions are constrained to be quasi-two dimensions with a large horizontal scale and weak vertical scale. The nonlinear interactions among these two-dimensional eddies motions result in an inverse cascade of energy that progressively builds up to bigger eddy motions and subsequently merging into zonal jets (Salmon, 1980). That is to say, without a dissipation mechanism for geostrophic eddies, this inverse cascade of energy would result in the formation of eddies with a spatial scale of the size of the ocean basins.

The dynamics of geostrophic eddies are expected to follow the properties of geostrophic turbulence which was first proposed by Charney (1971) and have been well described by other authors (Rhines, 1975, 1979). For stratified rotating quasi-two-dimensional fluid motion, geostrophic turbulence theory predicts a direct cascade of energy for a baroclinic flow but an inverse cascade of energy for a barotropic flow. For the ocean with a surface intensified stratification, energy from higher baroclinic modes concentrates in the first mode and then undergoes a direct cascade towards the deformation scale (R_d) (Smith and Vallis, 2002). At R_d, baroclinic energy is converted to barotropic mode via a process called barotropization. At this point, most of the energy near the deformation scale cascade towards a larger scale while a small fraction undergoes direct cascade to dissipation.

The first estimates of kinetic energy flux in the real ocean based on altimeter (Scott and Wang, 2005) confirmed the existence of an inverse cascade of energy at the surface of the ocean with a little mismatch. First, the scale of the eddy source was found to be of higher magnitude than the prediction of the geostrophic theory. This shift in the scale of eddy source was attributed to the poor resolution of the altimeter dataset i.e the kinetic energy spectral estimates do not account for the unresolved smaller scales structures. This indicates that the magnitude and the range of kinetic energy spectral flux estimates are sensitive to the resolution of small scale oceanic motions. Secondly, the KE flux direction was contrary to geostrophic turbulence prediction for a baroclinic flow. The result was a bit ambiguous because the altimeter signal reflects only surface velocities, which are dominated by low baroclinic modes (Smith and Vallis, 2002). How then is the KE flux (estimated from surface velocities) dominated by an inverse cascade? Recent results from Scott and Arbic (2007) have shown that the inverse cascade of energy is not confined to the barotropic mode alone and that the kinetic energy associated with the first baroclinic mode also fluxes energy upscale. In summary, the inverse cascade observed at the surface of the ocean by altimeter is a combination of baroclinic and barotropic mode with the former having stronger contribution to the net cascade. Many recent results have equally confirmed this notion of an inverse cascade dominated ocean. Scott and

Wang (2005); Eden (2007); Sasaki et al. (2017); Tulloch et al. (2011); Aluie et al. (2017); Brüggemann and Eden (2015); Kjellsson and Zanna (2017); Khatri et al. (2018).

Since geostrophic motions (the largest reservoir of ocean kinetic energy) do not provide a route to kinetic energy dissipation by themselves, how then can energy be transferred from the large scale to small scale where viscous dissipation can act? Several processes have been proposed as potential sinks of geostrophic kinetic energy. Some of the mechanism that could damp geostrophic motions are;

- (a) *bottom drag* : dissipative interaction with bottom topography (Arbic and Flierl, 2004; Gille et al., 2000; Sen et al., 2008)
- (b) *wave emissions* : generation, radiation, and breaking of gravity waves by mesoscale eddies interacting with small-scale rough topographic (Naveira et al., 2004; Nikurashin and Ferrari, 2010; Nikurashin et al., 2013; Molemaker et al., 2010). This is particularly efficient in regions with rough topography such as the Southern Ocean
- (c) *loss of balance* : loss of geostrophic balance at the ocean surface boundary due to frontogenesis. Surface frontogenesis describes the formation of sharp density gradients as a result of eddy stirring at the ocean boundaries and this represents a direct cascade of baroclinic energy to scales smaller than the deformation radius (Molemaker et al., 2005; Hoskins and Bretherton, 1972)
- (d) *interactions with the internal wave field* : interaction between internal waves and geostrophic eddies can result in an irreversible extraction of kinetic energy from the geostrophic field. (Muller, 1976; Buhler and McIntyre, 2005)
- (e) *suppression by wind work* : wind stress act to spin down geostrophic eddies (Chris, 2016; Chi et al., 2016).

Most of these routes involve the transfer of energy from large scale to smaller scales where 3D turbulence can then cascade energy down to a dissipative scale. A review of these processes can be found in Ferrari and Wunsch (2009) and Barkan et al. (2017). In general, the flow of energy from large scale to dissipation is depicted in Figure 1.4. The middle regime in Figure 1.4 is currently a frontier in oceanography studies. New evidence from the investigation with numerous numerical simulations suggests that oceanic motions with spatial scale less than 100km (therein referred to as *fine-scales*) with Ro and $Fr \sim 1$ are playing a key role in the down-scale flux of kinetic energy towards dissipative scale. What exactly are these classes of motions at fine-scales?

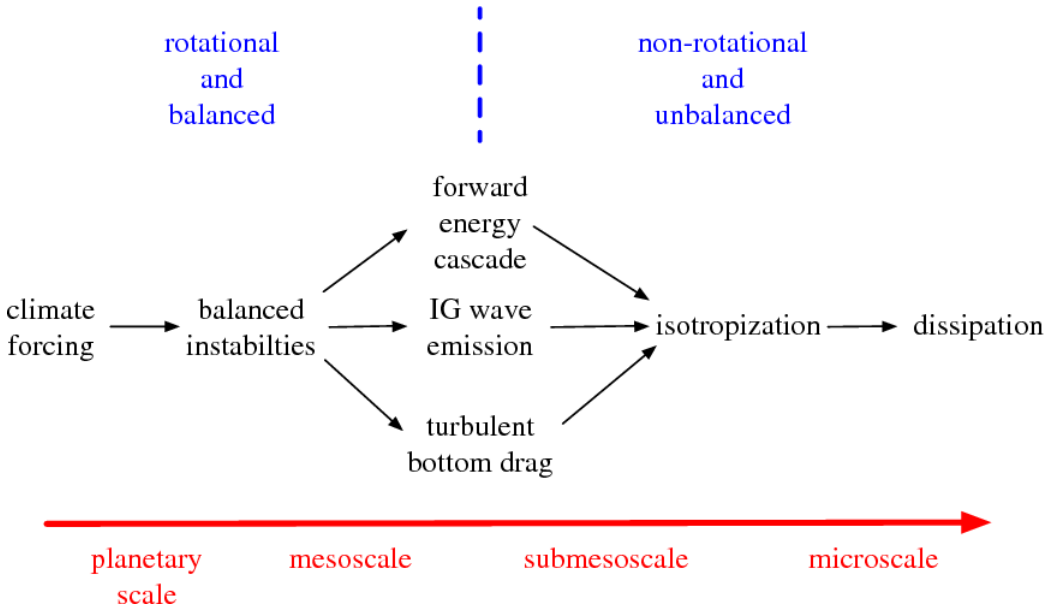

Figure 1.4: Image taken from McWilliams (2016). Stages in the oceanic general circulation from planetary-scale forcing to microscale dissipation and mixing. Indeed, we know much about the large scale balanced dynamics (LHS) where energy is injected into the ocean and the higher-frequency unbalanced motion (RHS) where this energy is been dissipated. The intermediate scale in between these two regimes is currently an area of ongoing research in the oceanography community.

1.2 Oceanic fine-scale motions: a key player in kinetic energy exchanges

1.2.1 Oceanic motions at fine-scale

Oceanic motion at fine-scale ($< 200km$) is dominated by *submesoscale balanced motions* ($< 50km$) (vortices, fronts, and filaments) and high-frequency *unbalanced internal gravity waves* ($< 100km$) (near-inertial waves, internal tides). These are two classes of motions that share similar spatial and temporal scales but with very different dynamical properties.

Submesoscales balanced motions are characterized by $O(1)$ Rossby number (a value much higher than mesoscale eddies) and large vertical velocity in the surface boundary layers. Nonlinear interactions within this class of motions yields the so called submesoscale turbulence. There is a wide variety of physical processes that can feed submesoscale turbulence. These mechanisms include strain-induced frontogenesis, topographic wakes, turbulent thermal winds, and mixed-layer instability (Thomas, 2008; Capet et al., 2008a; Mensa et al., 2013; Qiu et al., 2014; Sasaki et al., 2014; Callies et al., 2015b; Brannigan et al., 2015; McWilliams, 2016). Furthermore, observations from in-situ measurement (Shcherbina et al., 2013; Buckingham et al., 2016) and model simulations (Qiu et al., 2014; Sasaki et al., 2014; Brannigan et al., 2015; Rocha et al., 2016) have shown that submesoscale motions undergo a strong seasonality with stronger signature in wintertime. Many recent studies have argued that this seasonality is driven by mixed-layer instability with a deep mixed-layer in wintertime. This seasonality can be observed in form of a larger amplitudes of submesoscale buoyancy flux Mensa et al. (2013) and also in the skewness of the relative vorticity distribution in winter (Shcherbina et al., 2013; Buckingham et al., 2016).

There are suggestions that submesoscale motions have a strong impact on ocean circulation and the climate system as well. A recent result from Su et al. (2018) argues that submesoscale could be playing an essential role in the modification of momentum and heat exchange between the ocean and atmosphere and that the vertical velocities associated with submesoscales are strong enough to generate vertical fluxes of carbon and other biogeochemical tracers from the surface layer to the interior (Balwada et al., 2018). Chassignet and Xu (2017) also shows that resolving submesoscale motions in basin-scale ocean simulation has impacts on large scale circulation. The authors through a series of North Atlantic simulation with varying horizontal resolution ($1/12°$,$1/25°$,$1/50°$) show that the Gulf stream separation and its associated re-circulation gyres compare better with observation as the model's spatial resolution increases. Quantifying the impact of submesoscales in the global

ocean is currently an ongoing task in physical oceanography studies.

Of particular interest in this thesis are submesoscales coherent vortices therein referred to as submesoscale eddies. This kind of motions dominates oceanic eddy field at scales less than 100km. This class of eddy motions is less known due to the nature of their size. They are too small to be captured by our exiting satellite mission and they are also too big to be well resolved by shipboard instrument detection. Given that submesoscale motions (in general) undergo strong seasonality with large amplitude in winter. We do not know if this seasonality includes submesoscale eddies as well. In other words, *do submesoscale eddies vary seasonally? If they do, will this seasonality affect the distribution of the eddy length scale at the basin scale? Also, we don't know depth penetration of this class of eddy motions.*

As already mentioned, internal gravity waves (IGWs) co-exist with submesoscale balanced motions at fine scales. IGWs are a particular class of fast propagating unbalanced motions with frequencies equal to or larger than f and a spatial scale ranging from O(10m) to O(100km). IGWs include wind-induced near-inertial waves with a frequency near the Coriolis frequency and internal tides (generated by large scale barotropic tidal flow over topographic features) with diurnal and semidiurnal frequencies. The kinetic energy of internal gravity waves undergoes strong seasonality with large amplitude in summertime. This seasonality is due to shallower mixed-layer and the intensification of vertical normal mode in summertime (Rocha et al., 2016; Torres et al., 2018; Lahaye et al., 2019). *It is worth stressing that the seasonality of submesoscale balanced motions and unbalanced internal gravity waves is out of phase and that the implication of this seasonality on cross-scale kinetic energy exchanges is yet be explored.*

At fine-scales, submesoscale and internal gravity waves signals overlap. The task of separating these two classes of motion (with significantly different properties) is currently an ongoing research task (Qiu et al., 2018; Torres et al., 2018). There are indications that submesoscale motions and internal gravity waves motion do interact and that this interaction could leads to mixing in the interior of the ocean (Klein et al., 2003). Also, recent studies have emphasized that this interaction could provide a prominent pathway to kinetic energy dissipation. The reader can see Klein et al. (2019) for an up to date review on oceanic scale interaction.

1.2.2 Advancement in satellite missions and ocean models

The Surface Water and Ocean Topography (SWOT) altimetric mission (Fu and Ubelmann, 2014) which is scheduled for launch in 2021 is going to advance our knowledge of ocean dynamics at fine-scales by providing an unprecedented covered of the world ocean down to kilometric scale. SWOT will provide for the first time a

two dimensional (2D) map of Sea Surface Height (SSH) on a 1-2 km horizontal grid. The low noise level of the SWOT observation should allow us to resolve physical processes in the oceans down to a horizontal scale of 10km. This resolution is 10 times higher than existing conventional altimeters and observation from SWOT will bridge the existing gap in our knowledge of fine-scale dynamics particular at scales between 15km to 200km. This scale range which is dominated by fine-scale motions is important for the understanding of ocean dynamics and kinetic energy budgets particularly in terms of route to energy dissipation.

As promising as the information from SWOT would be for oceanographic study, some challenges come with the reliability of the information it provides at very fine-scales. At scale less than the Rossby radius, high-frequency and non-linear oceanic processes are likely to become more important and the degree of geostrophic balance is expected to fail. Like every other satellite, SWOT will provide velocities based on geostrophic approximations with no information on the ageostrophic component. Hence, *how accurate will the estimate of kinetic energy cascade at fine-scale be if its computation is based on geostrophic velocity ?*

In anticipation of SWOT, realistic numerical ocean models such as the NEMO based North Atlantic simulation with a horizontal resolution of 1/60° (NATL60), the Hybrid Coordinate Ocean Model of the Atlantic Ocean with a horizontal resolution of 1/50° (HYCOM50) and MIT General Circulation Model with horizontal resolution of 1/48° (MITgcm) have been designed in preparation for the upcoming altimeter mission. These state-of-the-art numerical experiments (with tidal forcing in some cases) can resolve explicitly oceanic motion at basin scale down to kilometric scale and can therefore provide virtual observations that anticipate the future SWOT data. This thereby provides an opportunity to investigate the dynamics of fine-scale oceanic motions by using basin scale realistic simulations.

1.2.3 A new route to kinetic energy dissipation

Many studies (e.g Sasaki et al. (2014) and Capet et al. (2008c)) by using submesoscale resolving simulations show that kinetic energy spectrum in high EKE region is shallower than expected i.e kinetic energy spectra slope changes from -3 (Philips regime) to -2 (Charney regime) move from eddy-resolving to submesoscale resolving numerical simulation (Figure 1.6). This result indicates that submesoscale motions play an active role in redistributing kinetic energy across scales. In a regime of energetic submesoscales, the inverse cascade of kinetic energy involves a broader scale-range that includes smaller scales and it also shows evidence of a stronger forward cascade of energy at smaller scales. These results provide evidence that submesoscales can feed large-scale motions via an inverse cascade of energy and can

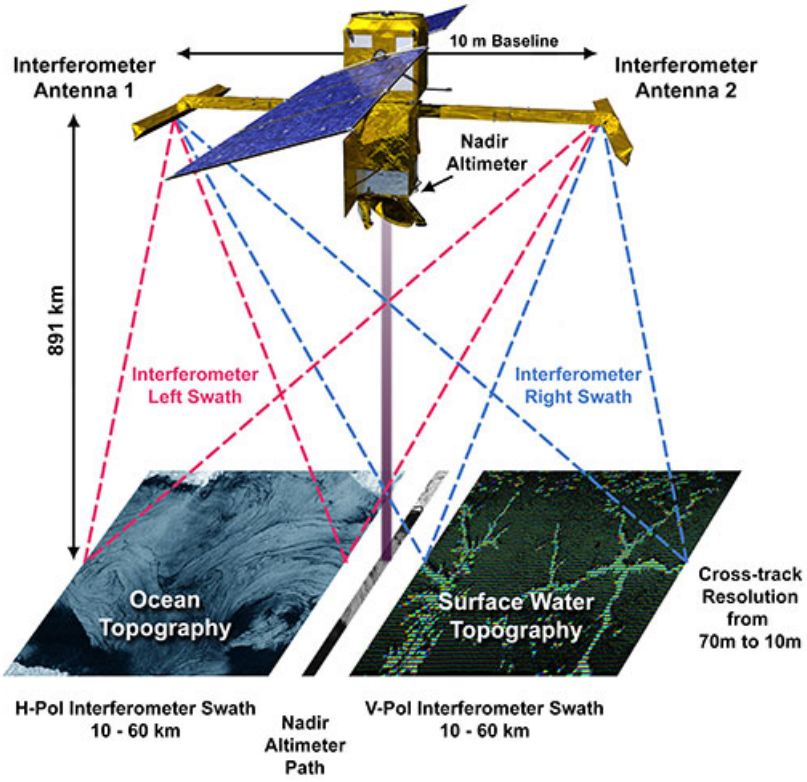

Figure 1.5: A schematic of the Surface Water and Ocean Topography satellite mission (SWOT) by NASA-JPL. SWOT is expected to go live in 2021 and will provide for the first time a two dimensional (2D) observation of the Sea Surface Height (SSH) on a 1-2 km grid. The low noise level of the SWOT observation should allow us to resolve physical processes in the oceans down to a horizontal scale of 10km. This resolution is 10 times higher than existing conventional altimeters.

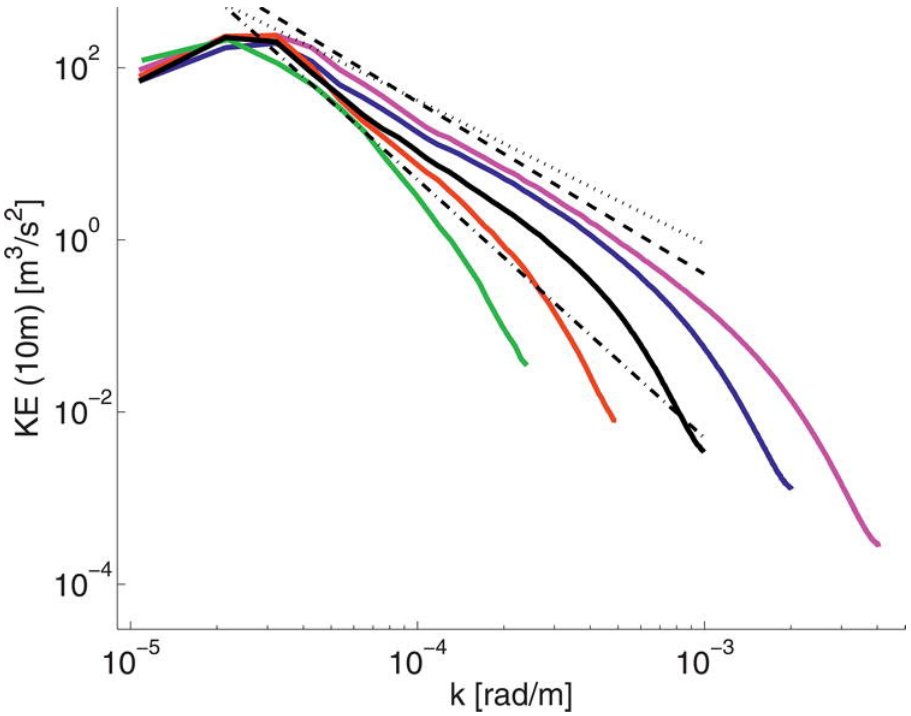

Figure 1.6: Image from Capet et al. (2008e). Kinetic energy at 10m depth as a function of horizontal wavenumber. The five solid lines correspond to spectra for the different simulations with horizontal grid scale decreasing from 12 to 0.75 km. The straight lines indicate $k^{-5/3}$ (dotted), k^{-2} (dashed), and k^{-3} (dotdash) spectrum slopes.

also trigger a direct cascade of energy from balanced motions down to dissipative scales (Capet et al., 2008e; Ferrari and Wunsch, 2009; McWilliams, 2016). *It is not clear if this forward cascade by submesoscales extends towards the interior of the ocean or is confined to the surface in the real ocean. We equally do not know if the forward cascade is sensitive to the seasonality of submesoscale turbulence throughout the ocean.*

There are new shreds of evidence based on idealized simulations that suggest that internal gravity waves (particularly near-inertial waves) can provide a route to kinetic energy dissipation. Wave emission has been reported to be leading order mechanisms for a direct cascade of energy at fine-scales (Brüggemann and Eden, 2015; Barkan et al., 2017). Results on the direct cascade of kinetic energy by wave emission can be classified into two mechanisms; (i) stimulated generation of a forward cascade of kinetic energy by near-inertial waves from balanced flows (Gertz and Straub, 2009; Rocha et al., 2018) and (ii) spontaneous generation of kinetic energy by near-inertial waves from balanced flows (Nagai et al., 2015; Shakespeare and Hogg, 2017). In a stimulated generation, near-inertial waves are first introduced by external forcing (e.g. wind) at the inertial frequency and then grow by extracting energy from the balanced flow (Barkan et al., 2017; Thomas, 2017; Gertz and Straub, 2009) while spontaneous generation is the emission of waves by unbalanced, large Rossby number

flow at density fronts without external forcing. Most of these studies have focused on the impact of wind-generated near-inertial waves on kinetic energy dissipation. Whereas little is known as to the role of internal tides on kinetic energy exchanges. We know that internal tides contribute to the building up of internal gravity waves continuum (Müller et al., 2015) and that they contribute to diapycnal mixing in the interior of the ocean (St. Laurent and Garrett, 2002; Chris, 2003; Vic et al., 2019). *Weather they could be playing a significant role in the down-scale transfer of kinetic energy is yet to be fully explored.*

1.3 North Atlantic ocean

My thesis will use the North Atlantic ocean as a typical mid-latitude ocean basin for studying cross-scale energy exchanges. To that end, we present in this section the North Atlantic Ocean. This is a well-studied region of the ocean and we do not intend to give a summary of the existing literature but rather to highlights and introduce this ocean basin has our region of study in this thesis. The North Atlantic Ocean as the name implies is the northern part of the Atlantic Ocean starting from around 8^oN up to the subpolar region. The North Atlantic ocean surface circulation (Figure 1.7) comprises of three major inter-connected currents; the Gulf stream, the North Atlantic current and the subpolar fronts. These currents are organized into two major gyres: the sub-polar and the sub-tropical gyres. The North Atlantic Subpolar Gyre plays a key role in climate variability, it forms an important part of the global overturning circulation serving as a region of deep water formation. Also, the Gulf stream is famous for transporting warm water from the subtropics to the polar regions and into Europe.

The North Atlantic ocean (like every other ocean) basin is baroclinically unstable and is therefore dominated by geostrophic eddy field. The Gulf stream, being a western boundary current is a major site for the generation of geostrophic eddies. Results from satellite observation and in-situ measurement have equally shown strong eddy energy along the North Atlantic Current and the Azores Current. The dynamics of this ocean basin, its impact on the world ocean circulation and its importance to climate can not be overemphasized and have therefore received much attention over the years.

The size of the North Atlantic ocean basin, existing knowledge about its circulation and cross-scale interaction makes it an ideal natural laboratory to study kinetic energy distribution and exchanges at fine-scales in the ocean. Recently Aluie et al. (2017) using 1/10th of degree numerical simulation investigated the cross-scale exchanges of kinetic energy in the Atlantic ocean. Their result (Figure 1.8) show that the North Atlantic ocean is dominated by an inverse cascade of eddy energy towards

larger-scale ocean circulation. This result is consistent with the findings of Schlösser and Eden (2007) who performed a similar analysis using an eddy-resolving model of the North Atlantic.

Similarly, the dynamical characteristics of eddy motions at large-scale (particularly scale of eddies) have been investigated in the North Atlantic. The typical scale of mesoscale eddies in the North Atlantic is between the Rosbby radius of deformation and the Rhine scale Eden (2007); Chelton et al. (2011). However, these aforementioned studies provide no information as to the nature of cross-scale kinetic energy exchanges and the scale of eddy motions at finer-scales. The focus in this thesis work is to extend on these existing literature by investigating the distribution of eddy scale and kinetic energy exchanges down to 10km scale in the North Atlantic ocean.

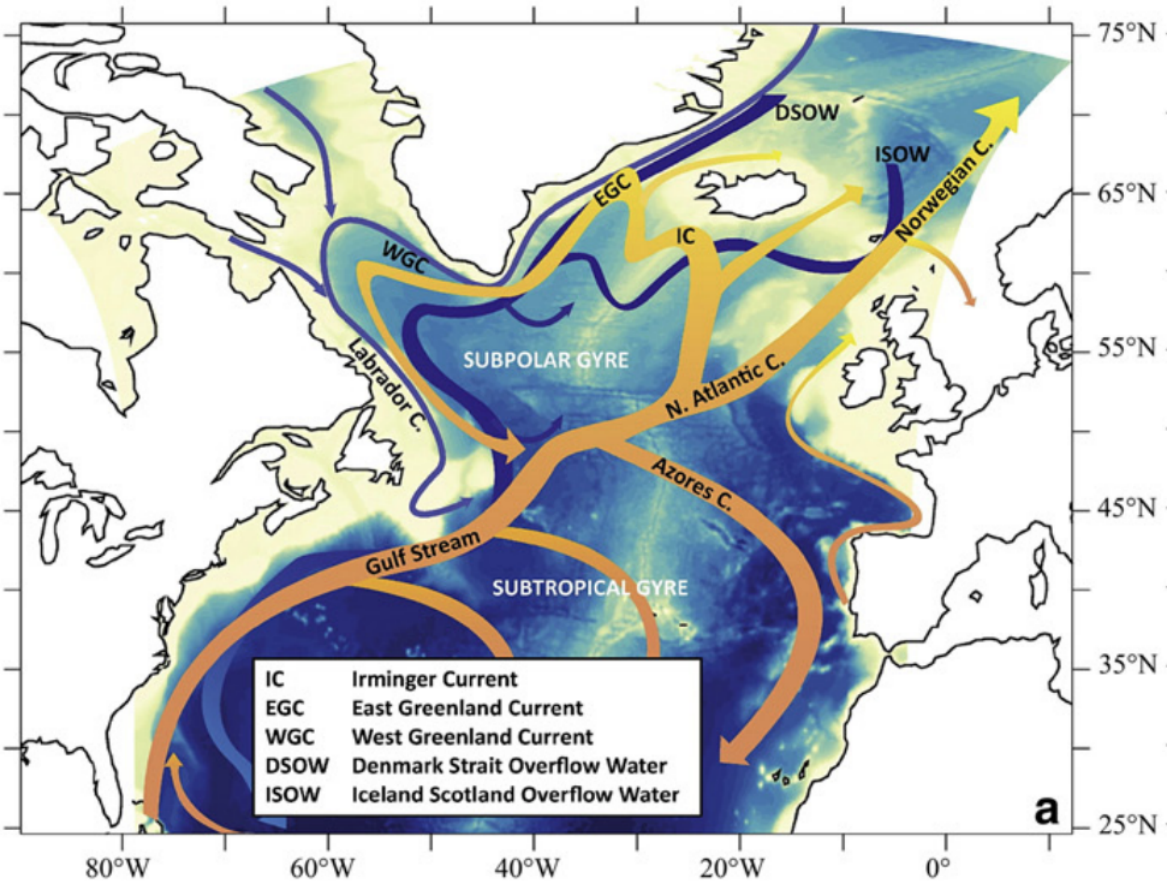

Figure 1.7: Schematic of the North Atlantic circulation pattern. Deeper currents are in blue, shallower ones in orange/yellow. Image taken from Alice et al. (2015)

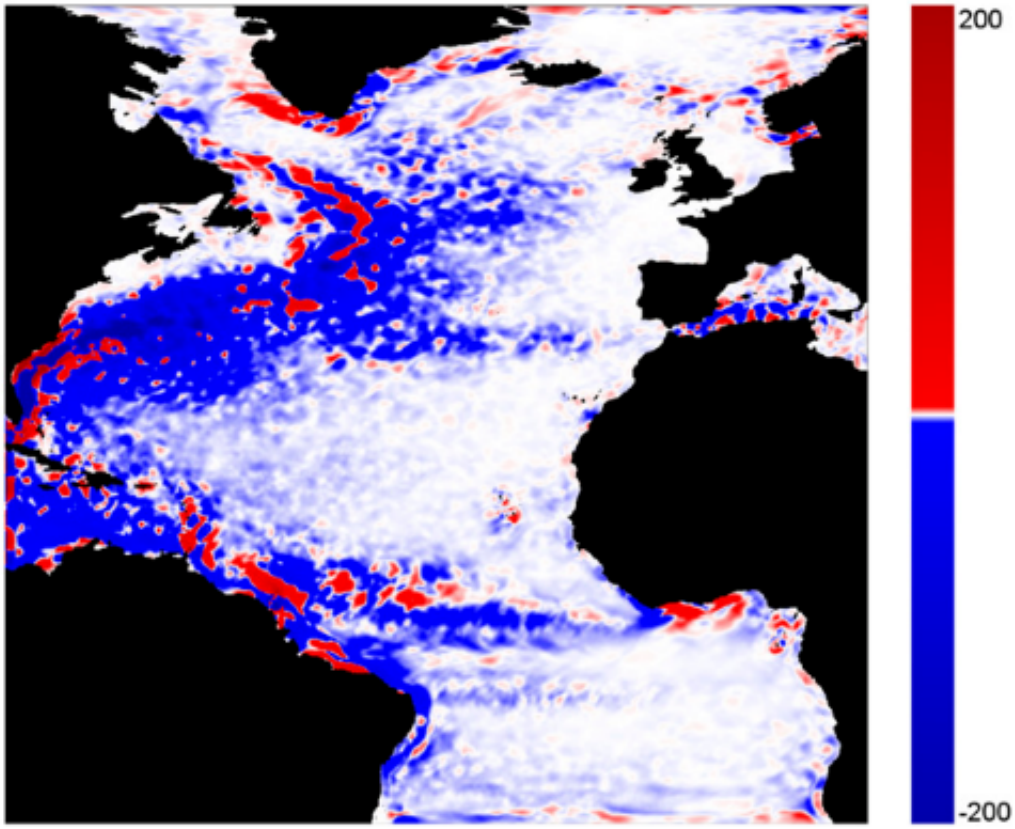

Figure 1.8: Figure from Aluie et al. (2017). Geographic maps of the cross-scale kinetic energy exchanges at the surface averaged over three years for scales > 200 km. The color map used, is not linear; most of the color shown has small values close to zero (white), and some blue/red regions exceed the maximum values on the color bar. We observe a downscale transfer in the current south of Florida, as the Gulf Stream turns northward, possibly indicative of eddy shedding or even just the small scale associated with the sharp turn in the trajectory. We also observe a strong (dark blue) upscale transfer in the Gulf Stream core east of Florida and the Carolinas. This persists well beyond the separation point (Cape Hatteras), indicating that energy is transferred from mesoscale eddies into the Gulf Stream, accelerating and focusing the current. Flanking both sides of this (dark blue) core, we see downscale transfer (red) most probably associated with barotropic instabilities resulting from strong shear. Overall, an upscale transfer dominates in the Gulf Stream, in accordance with QG.

1.4 Thesis Objective

In this introduction, based on recent literature, we have highlighted that submesoscales and internal gravity waves can provide a route to dissipate geostrophic kinetic energy. These classes of motions are more pronounced at fine-scales but we lack qualitative and quantitative information from observations at these scales. Our current knowledge of fine-scales is based mostly on kilometric numerical simulation of the ocean. These kilometric numerical simulations are computationally expensive to run at a global scale and have mostly been implemented for regional ocean basin. **In this thesis, our objective is to use high-resolution submesoscale permitting ocean models to investigate the impact of fine-scale motions on kinetic energy exchanges in the North Atlantic ocean**. This objective is divided into three themes with each theme addressing specific open questions.

A: Seasonal and regional distribution of fine-scale eddy structures in the North Atlantic.

Given that eddies are the largest reservoir of kinetic energy in the ocean, the goal of this theme is to investigate the spatial and temporal variability of oceanic eddies in the North Atlantic. In contrast to existing literature, we focus specifically on eddies with scales $< 100km$ and we attempt to answer the following questions;

- What are the scales of oceanic eddies at fine-scales??
- What is the depth penetration of submesoscale eddies?
- Is the scale of oceanic eddies sensitive to the seasonality of submesoscale turbulence?

B: Kinetic energy transfer at fine-scale in a regime of energetic submesoscale motions.

In this research theme, our aim is to understand how submesoscale turbulence affects kinetic energy exchanges at fine-scales both at the surface and in the interior of the ocean. The key questions in this theme are listed below.

- Does the seasonality of submesoscale turbulence affect cross-scale kinetic energy exchanges?
- Is the forward cascade due to submesoscales surface-confined?

- At fine-scale, (using geostrophic current), how accurate is the estimate of kinetic energy cascade?

C: Kinetic energy transfer at fine-scale in a regime of externally forced internal tides.

Based on recent pieces of evidence on the role of internal gravity waves on kinetic energy dissipation and particularly that of internal tides on mixing in the ocean. We aim to investigate whether internal tides impact kinetic energy dissipation. We aim to answer the following questions;

- Do internal tides affect the distribution of kinetic energy at a fine-scale?
- How do internal tides modify kinetic energy cascade?
- Can internal tides provide a route to kinetic energy dissipation?

In light of the objective of the thesis work, we organized this manuscript as follows: Chapter 2 provides a description and the evaluation of the North Atlantic numerical simulations used in this thesis work. In Chapter 3, we investigate the seasonal and regional variability of fine-scale eddy structures in the North Atlantic. Chapter 4 presents the impacts of submesoscale motions on cross-scale kinetic energy exchanges while in chapter 5, we investigate how externally forced internal tide can affect kinetic energy cascade at fine-scales. We conclude this thesis in Chapter 6 by providing a summary of our scientific findings, the key differences between the two major numerical simulations used in this thesis, and the implication of our results for future work.

Chapter 2

Description and Evaluation of North Atlantic Ocean Simulation

Contents

2.1 Introduction

Realistic ocean simulations have recently been designed and implemented in anticipation of the Surface Water and Ocean Topography satellite mission. These numerical simulations are capable of resolving oceanic motions down to kilometric scale. Due to the limitation in computational cost, these high-resolution ocean simulations have mostly been implemented for regional ocean basin. The results presented in this thesis are based on the analysis of three of such existing submesoscale permitting simulations of the North Atlantic ocean. Namely, these simulations are (i) the NEMO-based North Atlantic simulation with horizontal resolution of $1/60°$ (NATL60) (ii) the Hybrid Coordinate Ocean Model of the Atlantic Ocean with a horizontal resolution of $1/50°$ (HYCOM50) and (iii) the spatially extended version of NATL60 with/without tidal forcing thereafter referred to as eNATL60. These numerical simulations have been designed to explicitly resolve oceanic fine-scale motions, a class of motions that are currently less known in physical oceanography.

The key objective of this thesis is to investigate the role of fine-scale ($< 100km$) motions on cross-scale kinetic exchanges on the basis of these numerical simulations. We are equally interested in investigating the spatial and temporal variability of ocean eddies at fine-scales. Diagnosing kinetic energy exchanges at fine-scales partly depends on accurate estimates of velocity gradients at kilometric scale. To that end, the focus of this chapter is not to provide a full evaluation of these numerical simulations but rather to access the ability of these simulations to predicts the dynamics in the North Atlantic Ocean particularly at fine-scales and we would like to know to what extents we can trust these models in terms of their resolved;

- large-scale ocean circulation patterns,
- upper-ocean kinetic energy levels,
- and upper-ocean horizontal gradients of velocity and buoyancy.

The analysis presented in this chapter comprises of contributions from scientists that have used these numerical simulation for different studies. It is worth noting that eNATL60 simulation was performed recently and at the moment, we have limited materials as regards the evaluation of this simulation with observation. Also because NATL60 is performed in MEOM group, this model's output is easily accessible and therefore we have more materials on NATL60 evaluation compared to HYCOM50.

In concise, we compare the output of these simulations to observations from satellite and in-situ measurements. We focused on evaluating the ability of these simulations to reproduce kinetic energy levels across the North Atlantic at different spatial

scales and also on the ability of NATL60 to predicts the statistics of (horizontal) velocity and buoyancy gradients at fine-scales. In the next section, we provide a short description of these numerical simulations. In section 3 we present the evaluation of these models based on resolved meso and large scale dynamics while in section 4, we compare and contrast the statistics of horizontal gradients of NATL60 with in-situ measurements.

2.2 Description of North Atlantic Numerical Simulations

2.2.1 NATL60

NATL60 is a NEMO-based submesoscale permitting simulation of the North Atlantic with a horizontal resolution of 1/60° (NATL60). The simulation has a horizontal grid spacing of 1.6 km at 26°N and 0.9 km at 65°N. The grid has been designed so that the model explicitly simulates the scales of motions that will be observed by SWOT altimeter. i.e the simulation can resolve oceanic motion down to about 10 km in wavelength. The initial and open boundary conditions are based on GLORYS2v3 ocean reanalysis with a relaxation zone at the northern boundary for sea-ice concentration and thickness. The model has 300 vertical levels with a resolution of 1 m at the top-most layers. The atmospheric forcing is based on DFS5.2 (Dussin et al., 2018), the grid and bathymetry follow Ducousso et al. (2017). To implicitly adapt lateral viscosity and diffusivity to flow properties, a third-order upwind advection scheme is used for both momentum and tracers in the model simulation. The model spin-up is for a period of six months followed by a one-year simulation output from October 2012 to September 2013. A summary of the model parameter is presented in Table 2.1. NATL60 simulation outputs have been used in recent studies by Fresnay et al. (2018) and Amores et al. (2018). Figure 2.1 present a snapshot of surface relative vorticity for September 1st, well depicted in the plot is the ability of NATL60 to resolve both large and fine-scale oceanic motions. In particular, we see vortices, fronts, and filaments at fine-scales.

2.2.2 eNATL60

eNATL60 is a spatially-extended version of NATL60 with the same numerical configuration. eNATL60 spans the North Atlantic from about 6°N up to the polar circle and fully includes the Gulf of Mexico, the Mediterranean Sea, and the Black Sea. The model is spin-up for a period of 18 months, followed by a one-year sim-

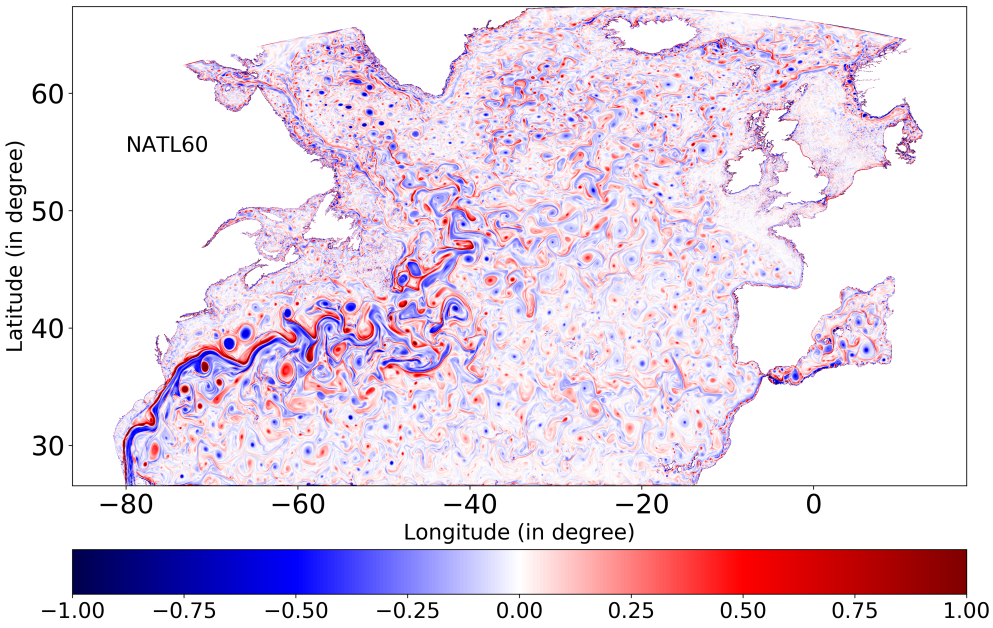

Figure 2.1: NATL60 : snapshot of surface relative vorticity field normalized by the Coriolis frequency on September 1st.

ulation output from July 2009 to June 2010. eNATL60 has two identical runs (i) eNATL60 with tidal forcing (M2, S2, N2, K1, O1) therein referred to as eN60-WT and (ii) eNATL60 with no tidal forcing eN60-NT. The two simulations have the same numerical configuration except for the inclusion of tidal motions in eN60-WT. The inclusion of tides in eN60-WT run provides conversion of tidal energy into the internal wave field through, both, flow-topography interactions and wave-balanced motions interactions. A plot of surface relative vorticity is presented in Figure 2.2. Like NATL60, eNATL60 resolves both mesoscale motions, submesoscale motions, and Internal Gravity Waves. Very visible from the plot is the famous North Atlantic Gulf stream and its separation. The tidal motions are equally visible in the English Channel and the North sea in a snapshot of the surface speed (`https://vimeo.com/300943265`). A summary of the model parameter is presented in Table 2.1.

2.2.3 HYCOM50

The Hybrid Coordinate Ocean Model of the Atlantic Ocean with a horizontal resolution of 1/50° (HYCOM50) is a simulation with a climatological forcing. The simulation was integrated for 20 years and the last year of the simulation output is used in this thesis work. HYCOM50 has a horizontal resolution of 2.25 km at the equator and (~ 1.5 km in the Gulf Stream region) and like NATL60 can resolve oceanic motion down to 10km in wavelength. The model extends from 28°S to 80°N, but in this study, we consider the outputs of HYCOM50 for exactly the same region covered by NATL60 to have comparable results. The vertical coordinate is hybrid and it has 32 layers. The atmospheric forcing is based on ERA-40 and the initial and boundary conditions are based on GDEM. The horizontal viscosity operator is a combination of Laplacian and Biharmonic. The bathymetry is based on the Naval Research Laboratory (NRL) digital bathymetry database. The model configuration and a detailed evaluation of the model results in the Gulf Stream region with observation are documented in Chassignet and Xu (2017). A summary of the model parameter is presented in Table 2.1 and a snapshot of the surface relative vorticity is presented in Figure 2.3.

Model comparison strategy

In the introduction, we established that the objective of this thesis work is to use the above described numerical simulations to investigate fine-scale oceanic motions. Given that our simulations differ in terms of numerical configuration and period of spin-up, we would not be surprised to see differences in the predicted dynamics of these simulations despite having a similar horizontal resolution. In this chapter, we

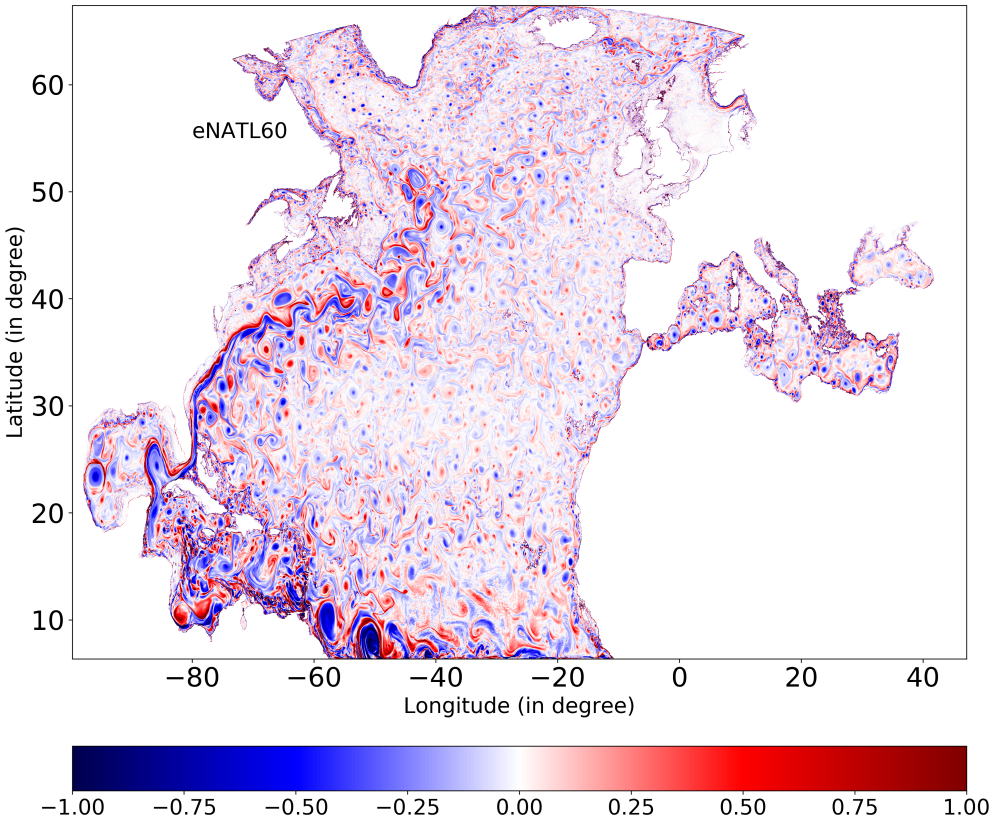

Figure 2.2: eNATL60 : snapshot of surface relative vorticity field normalized by the Coriolis frequency on September 1st.

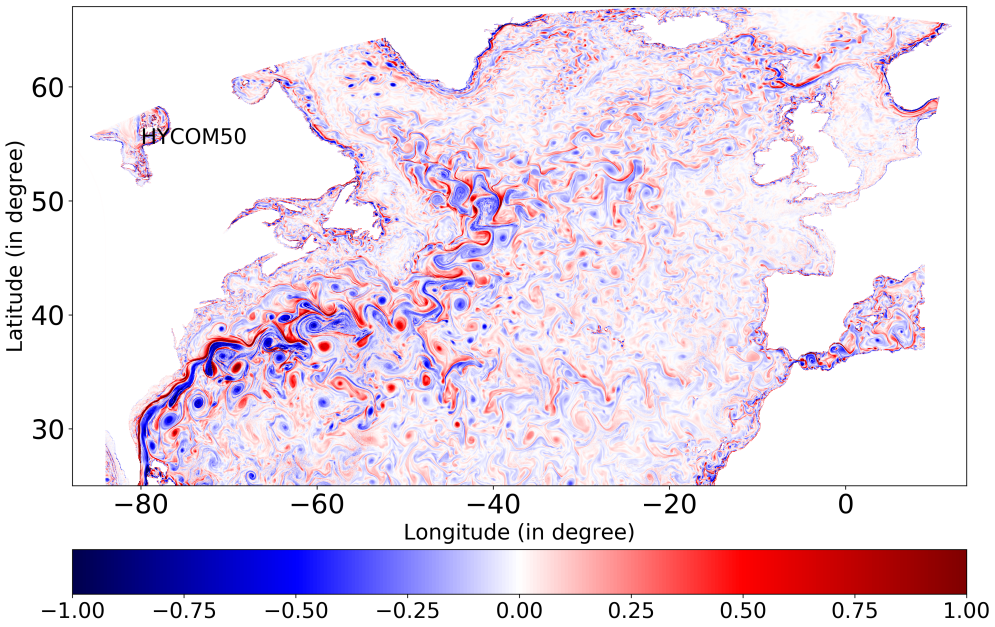

Figure 2.3: HYCOM50 : snapshot of surface relative vorticity field normalized by the Coriolis frequency on September. We show RV for the same region covered by NATL60 and not for the entire region of HYCOM50.

Table 2.1: Table of model parameters for NATL60, HYCOM50 and eNATL60.

	NATL60	eNATL60	HYCOM50
Domain	26.5N - 65N	9N - 65N	28S - 80N
Numerical Code	Nemo v.3.6	Nemo v.3.6	HYCOM
Horizontal grid	1/60: 0.9-1.6 km	1/60: 0.9-1.6 km	1/50:1.1-2.2 km
Vertical coordinate	Z partial cells	Z partial cells	Hybrid (Z & isopycnal)
Vertical grid	300 Levels : 1-50 m	300 Levels : 1-50 m	32 Layers
Boundary conditions	GLORYS2v3	GLORYS2v3	GDEM
Atmospheric forcing	DFS5.2	DFS5.2	ERA-40
Horizontal Viscosity	UPS	UPS	Laplacian & Biharmonic
Tidal constituents	–	M2, S2, N2, K1, O1	–

will not discuss the results of the model comparison. Our findings on the differences and similarity between these simulations based on the results of this thesis are presented in each study and a summary of these findings is documented in the concluding chapter of the thesis.

2.3 Evaluation of Resolved Large-scale Dynamics

In this section, we present a short comparison of the North Atlantic simulations with observational datasets. We do this by analyzing, the mean dynamical topography, the vertical profile of temperature and salinity, the root-mean-squared of sea surface height, SSH spectra density, the vertical distribution of the zonal velocity and eddy kinetic energy. Observation from satellite altimeter remains a major source of information about the ocean at global scale. In particular, we compare the output of these simulations with gridded AVISO product and SARAL AltiKa satellite altimeter data. This comparison focuses on evaluating large and mesoscale ($> 100km$) oceanic motions that are resolved in these numerical simulations. As previously highlighted eNATL60 was available only at the end of this thesis work and a thorough assessment of this dataset has not been performed yet at the time of writing this manuscript. Nonetheless, we believe that, the dynamics resolved by eNATL60 should be similar to NATL60 given that the eNATL60 is a spatially extend version of NATL60 with similar numerical configuration.

2.3.1 Large scale circulation and stratification

In this section, we evaluate the resolved large-scale circulation in NATL60. Large-scale ocean circulation is driven by global density gradient that is created by surface heat and freshwater fluxes. Large-scale ocean circulation has great impacts on tem-

perature (θ) and salinity (S) profiles both at the surface and in the interior. Thanks to measurements by Argo floats, our approach of assessing the representation of large scale flows in our model is to compare the observed vertical profiles of temperature and salinity in the real ocean with the prediction of the model. In Figure 2.4 and 2.5, we show the profiles of θ and S for NATL60 and EN4 datasets. These profiles are estimated within 10° x 10° boxes across the North Atlantic Ocean. In both plots, the black line represents observation from Argo float averaged over one year while the red (for temperature) and blue (for salinity) shade represents the 10th percentile, the mean and the 90th percentile that are estimated from NATL60. The observed profiles compare well with the predictions of NATL60. This agreement is particularly strong in the interior with a slight deviation at the surface layers within the subpolar gyres.

Another quick way to assess the representation of the resolved large scale circulation in our simulation is to compare the simulation output with information coming from AVISO in terms of the mean state of the geostrophic current and the mean dynamical topography. This analysis averaged over one year is presented in Figure 2.6. The magnitude of the geostrophic current and the mean dynamical topography predicted by NATL60 is identical with the observation from AVISO with the likelihood of a stronger current around and along the Gulf stream. This information coupled with the agreement between NATL60 and the observed temperature and salinity profiles validates the reliability of the resolved large scale circulation in NATL60.

2.3.2 Mesoscale variability

In this section, we assess the fidelity of our models to reproduce energy levels at different spatial scales by comparing their estimate of SSH spectral density with SARAL-AltiKa. We present in Figure (2.7) the SSH spectral density of NATL60, eNATL60 and SARAL/AltiKa in a region at the center of the North Atlantic gyre (50°W to 20°W,30°N to 50°N), both in wintertime (January. February and March) and summertime (July, August and September). The model spectra density is based on SSH values that were extracted from the model's hourly output following the 1D along-track coordinates of SARAL-AltiKa. The spectra results for the simulations and the observation show strong agreement. This agreement is robust for scales greater than 100km because spectral result below this scale is affected by the satellite instrument noise. The spectral density for eN60-NT (no tides) and NATL60 is identical across all scale both in winter and summer. As already highlighted, eNATL60 is a spatially extended version of NATL60 and we do not expect to see much difference between the two simulations. Also, there seems to be quite a robust agreement between eN60-WT (with tides) and eN60-NT (no tides) simulations at all scales in wintertime. However, of particular interest is the difference between the

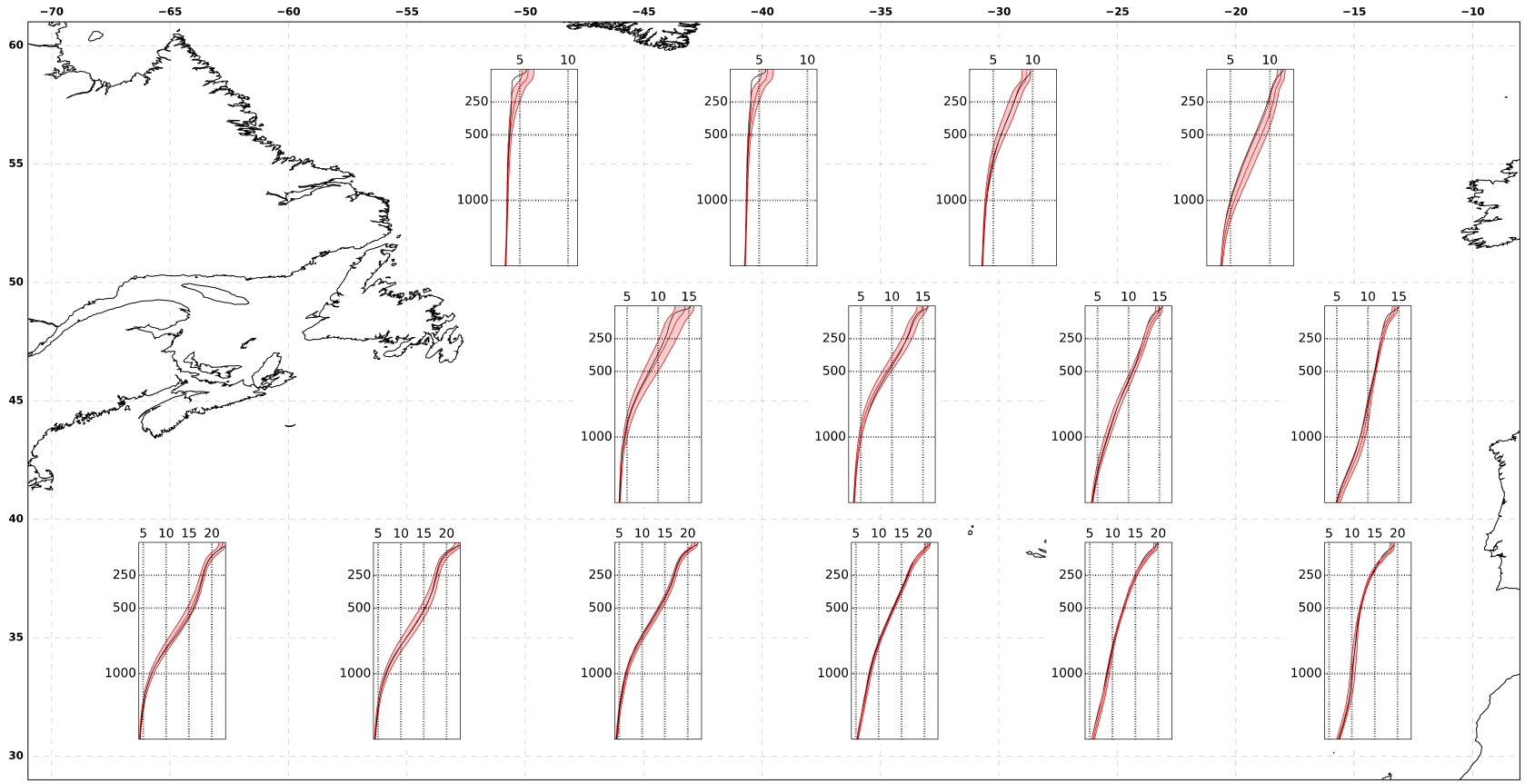

Figure 2.4: NATL60 and EN4 comparison of vertical profile of temperature at different regions in the North Atlantic. The black line represents the observed profile while the red line represents all the profiles at each model grid point within that 10∘ box region. The analysis presented in this plot was prepared by Aurelie Albert (MEOM, CNRS)

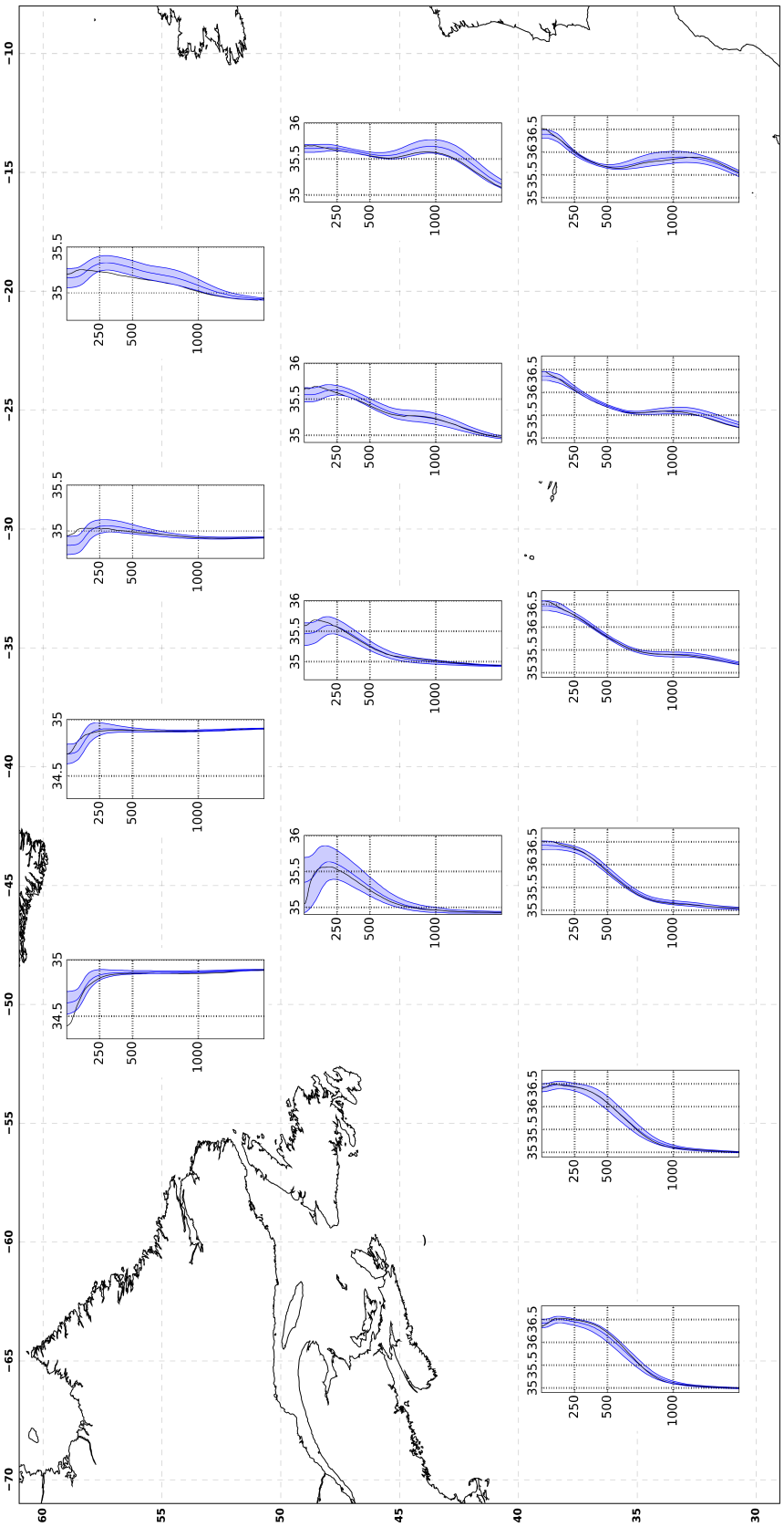

Figure 2.5: NATL60 and EN4 comparison of vertical profile of salinity at different regions in the North Atlantic. The black line represents the observed profile while the red line represents all the profiles at each model grid point within that 10o box region. The analysis presented in this plot was prepared by Aurelie Albert (MEOM, CNRS)

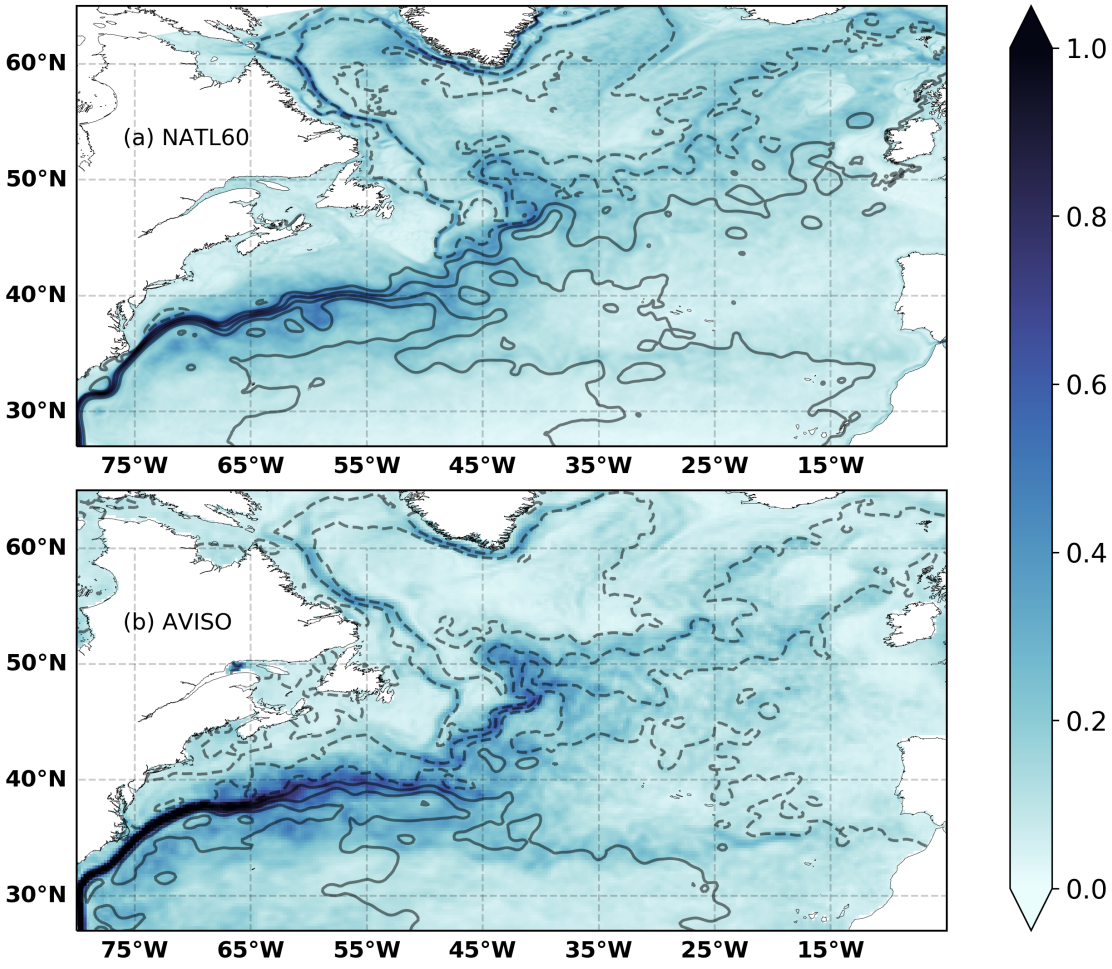

Figure 2.6: Mean surface geostrophic velocity intensity (ms^{-1}) in AVISO (top panel) and NATL60 (bottom panel), contours are mean absolute dynamical topography (contours every 20cm).

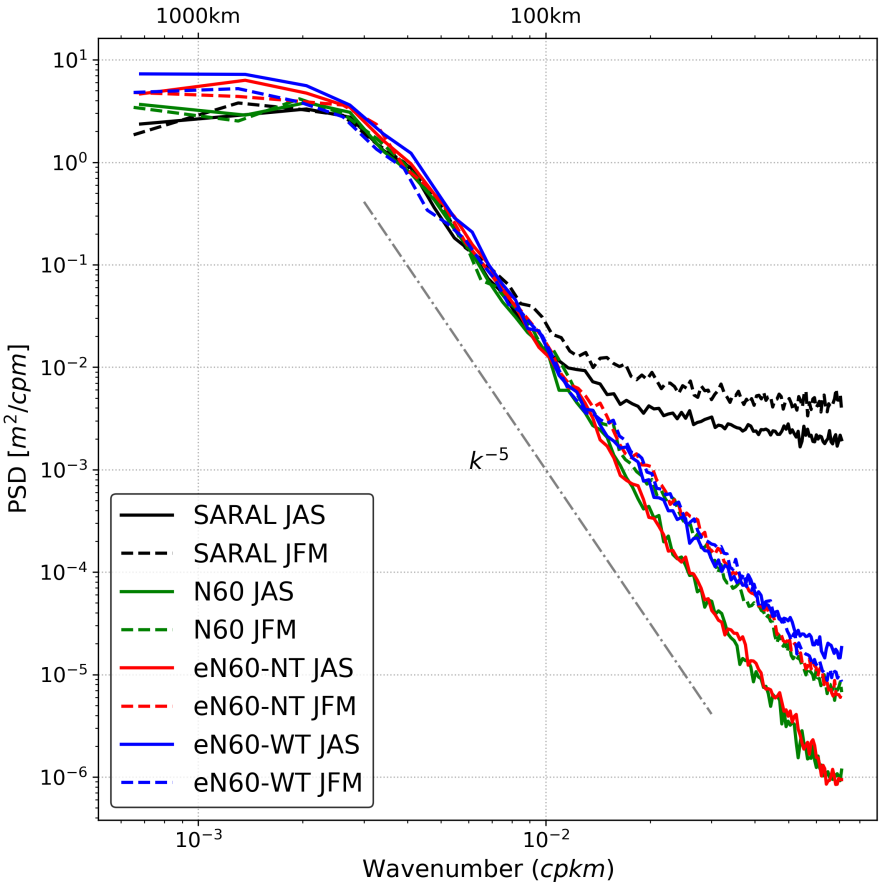

Figure 2.7: SSH wavenumber spectra for SARAL AltiKa (black line), NATL60 (green), eNATL60-NoTides (red line) and eNATL60-WithTides (blue line) in box at the middle of North Atlantic Gyre 50°W to 20°W,30°N to 50°N. The model spectra is estimated from along track SSH values based on SARAL AltiKa flight coordinates. The analysis presented in this plot was prepared by Laurent Brodeaux (Ocean-Next)

eN60-WT and eN60-NT in summertime where variance at fine-scales is of higher magnitude in eN60-WT. We shall see in Chapter 5 that this difference is due to enhanced internal wave activity due to internal tides in eN60-WT.

NATL60 and eNATL60 SSH spectra in Figure 2.7 is extracted using the hourly output of SSH fields. HYCOM50 SSH values are saved in daily averages and due to this, we could not reproduce this analysis for HYCOM50. To facilitate an accurate comparison between NATL60 and HYCOM50 in terms of SSH spectra, we present in Figure 2.8 a spectral density based on the 2D SSH field in a region around the Gulf stream for HYCOM50 and NATL60. The SSH spectra from the two models agree reasonably well. This indicates that the distribution of energy across scales in both models is similar, except that the variance at large scale is higher in HYCOM50 compared to NATL60. More in-depth analysis of the differences between the two simulations is provided later in this thesis work in chapter 3 and 4.

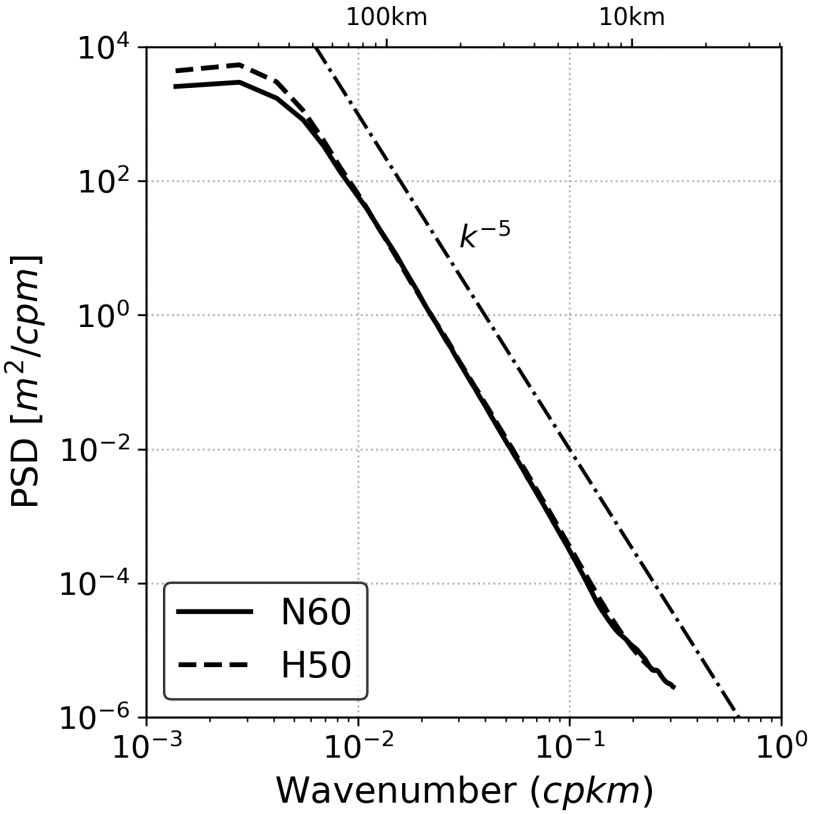

Figure 2.8: Seas Surface Hight (SSH) wavenumber spectra density for NATL60 (thick line) and HYCOM50 (dash line) in a region close to the Gulf Stream ($70°W$ to $60°W$, $30°N$ to $40°N$). This spectra is estimated using two dimensional SSH values for both model output.

The root-mean-square sea surface height computed from one year daily outputs of NATL60, HYCOM50, and AVISO is presented in Figure 2.9. The AVISO SSH field is derived from observations obtained by altimeter missions and then interpolated onto 0.25° mecartor grid. In this comparison, we have used AVISO mean dynamical topography dataset for October 2012 to September 2013. The SSH values from NATL60 and HYCOM50 are not degraded and the fields shown in Figure 2.9 are based on the models' original resolution. The comparison between the model output and AVISO data appears to be consistent in terms of geographical pattern of energetic oceanic motions except for the differences along the Gulf stream. The Gulf stream seems to be more energetic in HYCOM50 compared to NATL60 and AVISO. HYCOM50 has a spin-up of 20 years and this long spin-up allows for the full development of the Gulf stream energetics while NATL60 has a spin-up of 6 months. This difference in terms of spin-up strategy could be contributing a lot to differences in the energetics of the two simulations. We shall better discuss this in chapter 4.

The vertical distribution of the zonal velocity (upper panel) and eddy kinetic energy (lower panel) along the 55°W for both NATL60 and HYCOM50 is presented in Figure 2.10. The 55°W is a well-observed section with measurements taken during the POLYMODE experiments (Richardson, 1985) and SYNOP (Bower and Hogg, 1996). The level and the pattern of the vertical zonal velocity and eddy kinetic energy is fairly identical between the simulations and observation (Figure 2.11). However, between the two simulations, HYCOM50 shows a stronger penetration of eddy kinetic energy around 40°N - 42°N latitude. As stated above, differences in terms of energetics between the two simulations will be discussed later in this thesis work.

2.4 Evaluation of Resolved Fine-scale Dynamics in NATL60

In this section, we focus specifically on evaluating the ability of NATL60 to resolve fine-scale ($< 100km$) oceanic dynamics. In particular, we compare the distribution of upper ocean velocity and buoyancy gradients with measurements from satellite and in-situ measurements. Before going into this comparison with observation, we would like to emphasize that NATL60 is cable of capturing the seasonality of oceanic motions at fine-scales. Figure 2.12 reveals the emergence of strong and obvious seasonality in the surface relative vorticity field. This seasonality is pronounced almost everywhere in the North Atlantic and it is characterized by fine-scale motions with larger amplitudes of vorticity in winter compared to summer. In the next section, we will show that the statistics of the resolved relative vorticity (and the

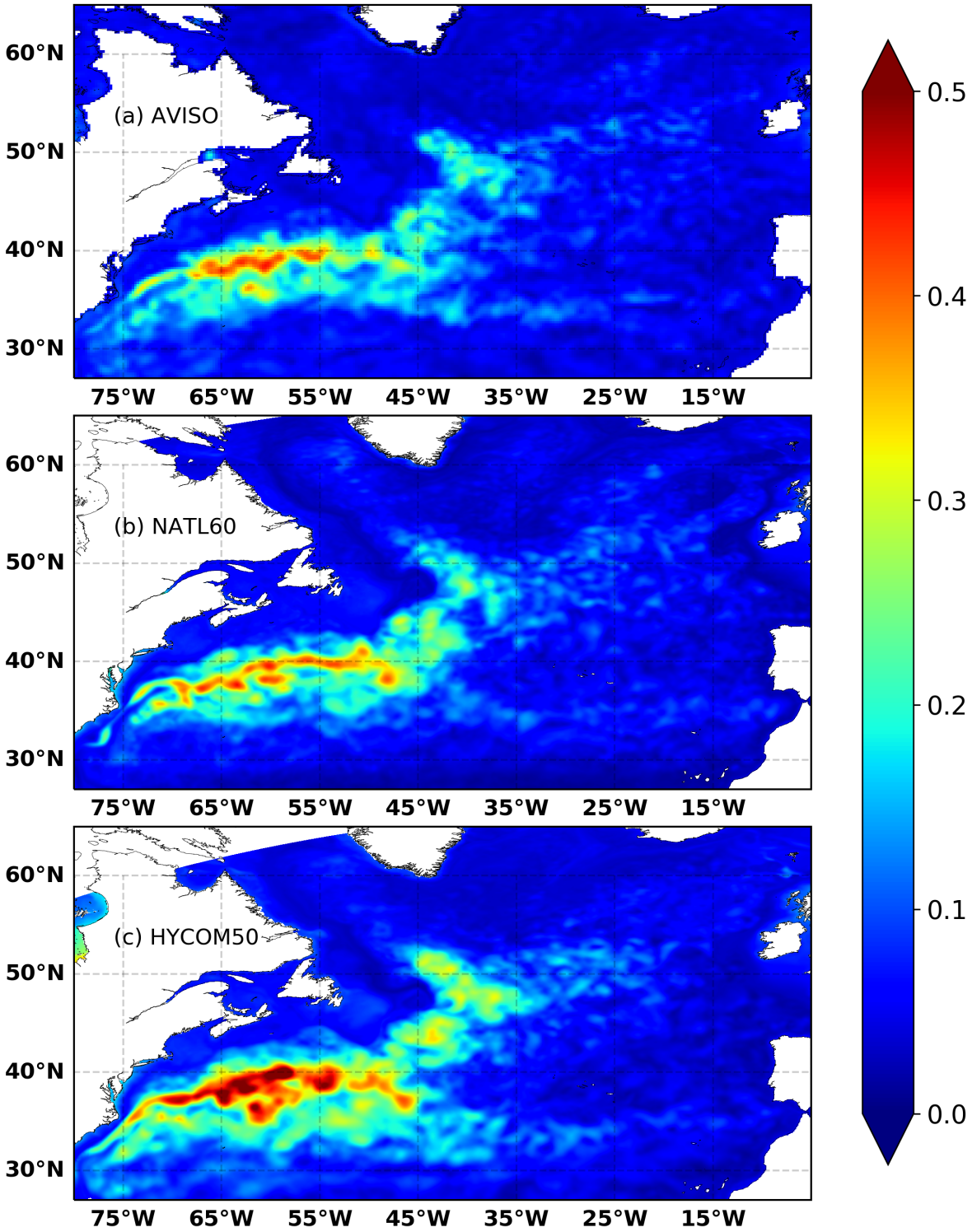

Figure 2.9: Standard deviation of sea surface height based on one year datasets for (a) AVISO, (b) NATL60 and (c) HYCOM50. The SSH values for NATL60 and HYCOM50 is not degraded.

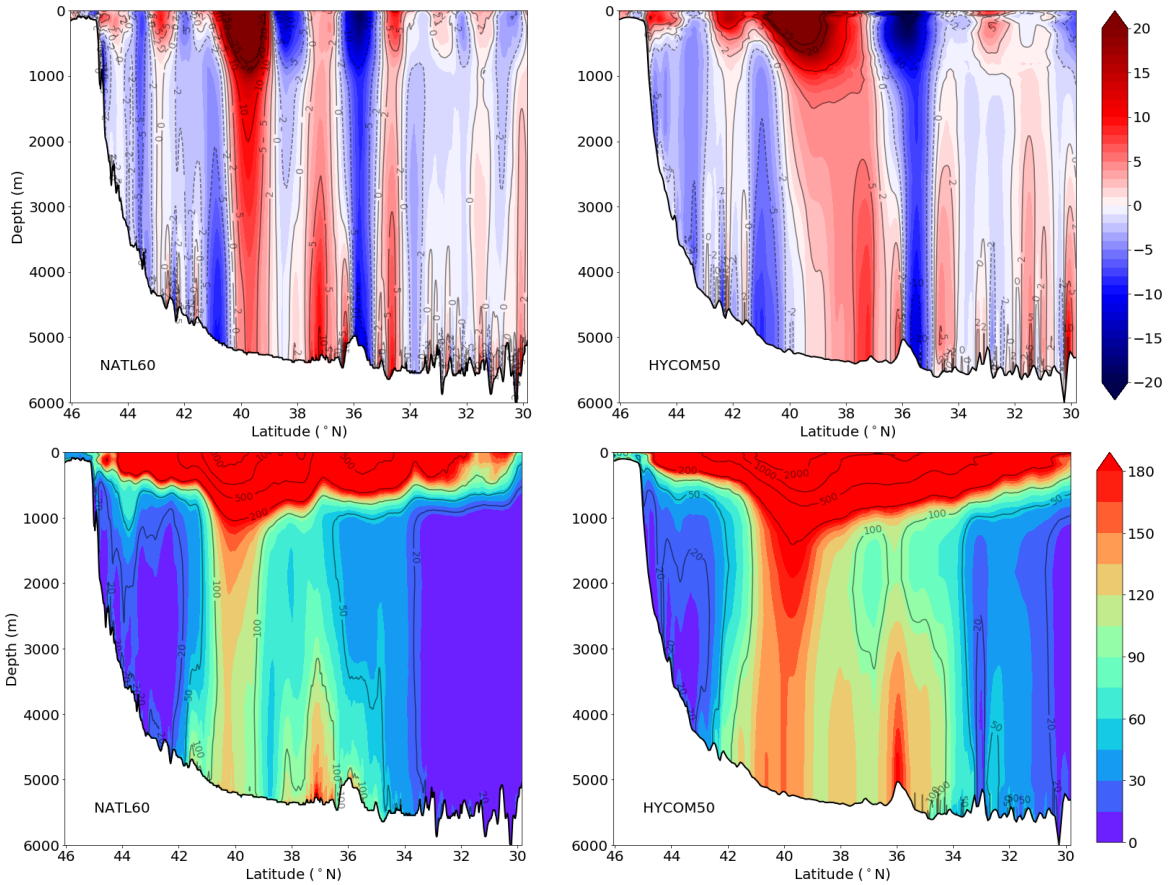

Figure 2.10: Vertical distribution of zonal velocity (upper panel) and eddy kinetic energy (lower panel) along 55°W for NATL60 and HYCOM50. The analysis presented in this plot was prepared by Aurelie Albert (MEOM, CNRS)

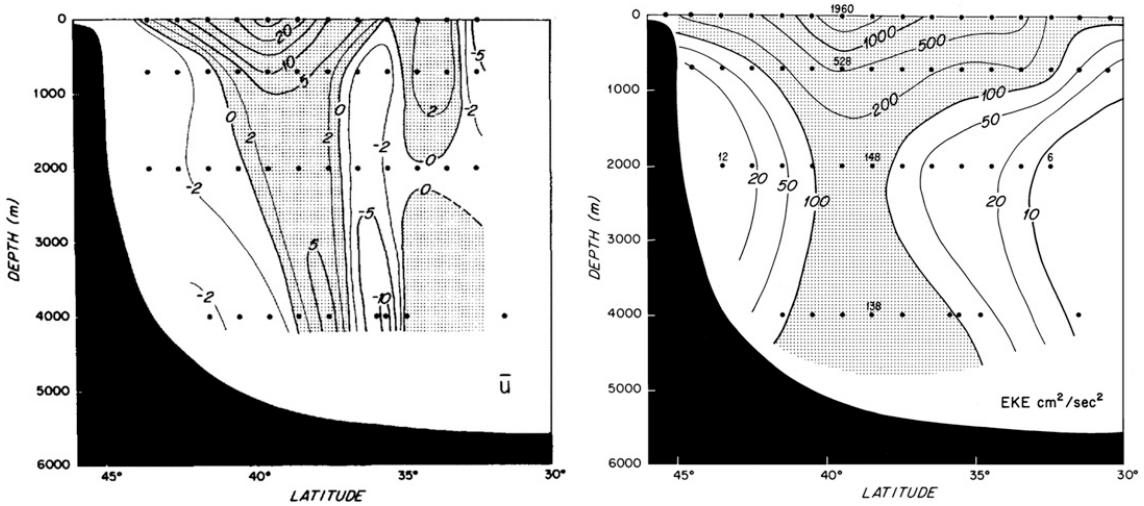

Figure 2.11: Vertical distribution of the observed (left) zonal velocity (cms^{-1}) and (right) eddy kinetic energy (cm^2s^{-2}) along 55°W based on current meter moorings and subsurface floats from (Richardson, 1985)

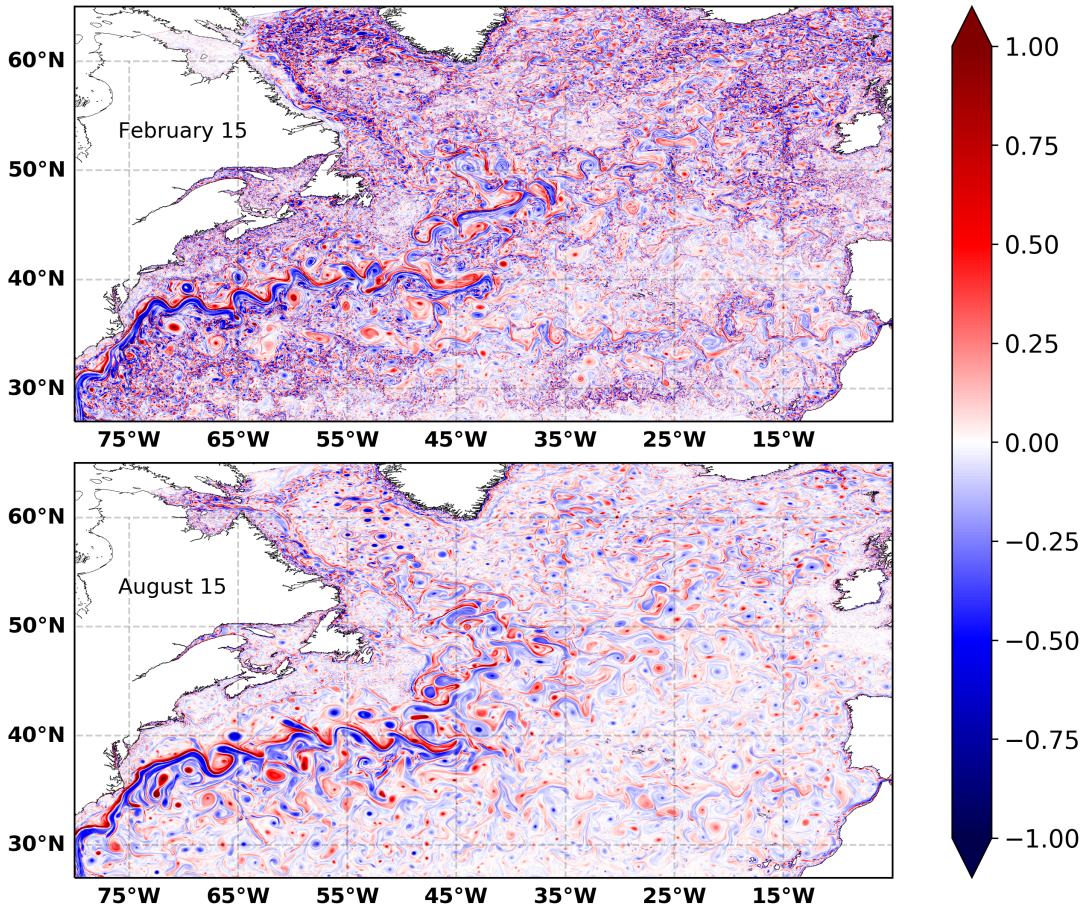

Figure 2.12: NATL60 : Snapshort of surface relative vorticity field normalized by the Coriolis frequency. Upper panel : February 15 and Lower panel : Augusts 15. Strong surface seasonality is due to the emergence of submesoscale fronts, filaments and vortices in winter.

horizontal gradient of velocities in general) is consistent with observations from the real ocean.

2.4.1 Upper ocean horizontal velocity gradients

Recent results from Shcherbina et al. (2013), Rocha et al. (2016) and Buckingham et al. (2016) have used the statistics of horizontal velocity tensor as a descriptor of the characteristics of submesoscale dynamics in the upper ocean. In this section, we use a similar approach to access the ability of NATL60 to capture the signature of fine-scale motions within the upper ocean. We do this by comparing the statistics of vorticity, divergence, and strain-rate with observation taking in the open ocean under the project called OSMOSIS. OSMOSIS (Buckingham et al., 2016) is an acronym for Ocean Surface Mixing, Ocean Sub-mesoscale Interaction Study. It is

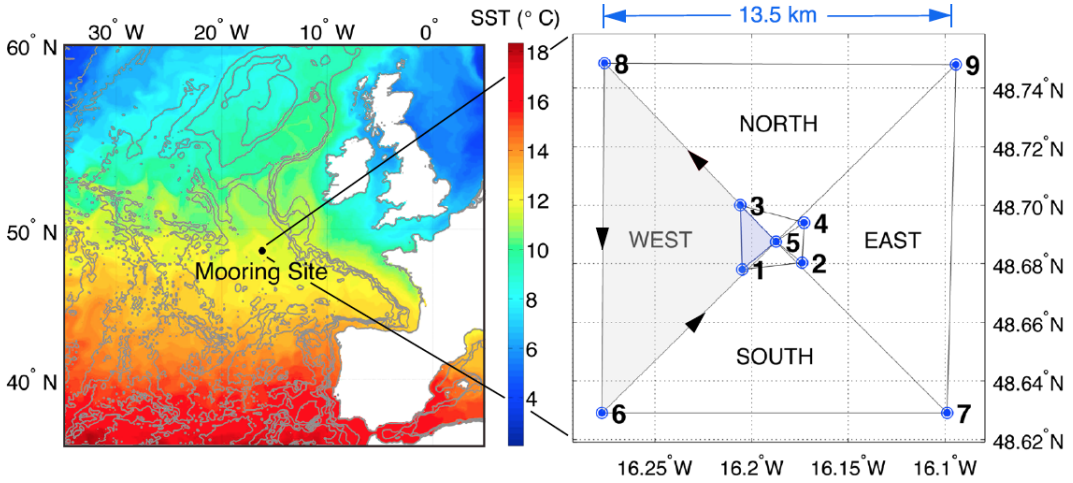

Figure 2.13: Geographical location of the OSMOSIS mooring array. Image from (Buckingham et al., 2016)

a research consortium formed to better understand the dynamics within the ocean surface boundary layer. Measurements of ocean quantities within the ocean surface boundary layer were taken in the North-east Atlantic Ocean (Figure 2.13) near (16° ,48°). This is a region where mean flows are weak and mesoscale eddies dominate the kinetic energy (Painter et al., 2010).

Nine (9) moorings and two (2) gliders were deployed in a two array formation as shown in Figure 2.14 and measurements of temperature, salinity, and horizontal velocity were taken for a period of one year from September 2012 to September 2013. This period of data acquisition corresponds to the same period of NATL60 production. On each mooring, Acoustics Current Metres (ACM) and MicroCAT Conductivity-Temperature-Depth (CTD) sensors were spaced 30m - 100m in the vertical. The time sampling interval for the CTD and ACM was 10 minutes for the outer mooring array and 5 minutes for the CTD attached to the center mooring. This dataset has been used in recently published articles to discuss the seasonality of submesoscale flows (Buckingham et al., 2016) and also the restratification effect of submesoscale vertical flow in the upper ocean (Yu et al., 2019).

In this thesis work, we used measurements taken by the outer mooring array because this array formation has a grid spacing that is consistent with the wavelength of oceanic motion that can be effectively resolved by NATL60. Horizontal velocities were obtained from the current meter while pressure, temperature, and salinity were obtained from the CTD. Prior to any computation, the dataset retrieved from these moorings were linearly interpolated in the vertical to get a well distributed vertical profile. To compare NATL60 and OSMOSIS datasets, horizontal velocity and potential density data were extracted from the model at the closet location to the coordinates of OSMOSIS outer mooring array. OSMOSIS time series is down-sampled to daily averages to facilitate accurate comparison with NATL60 daily

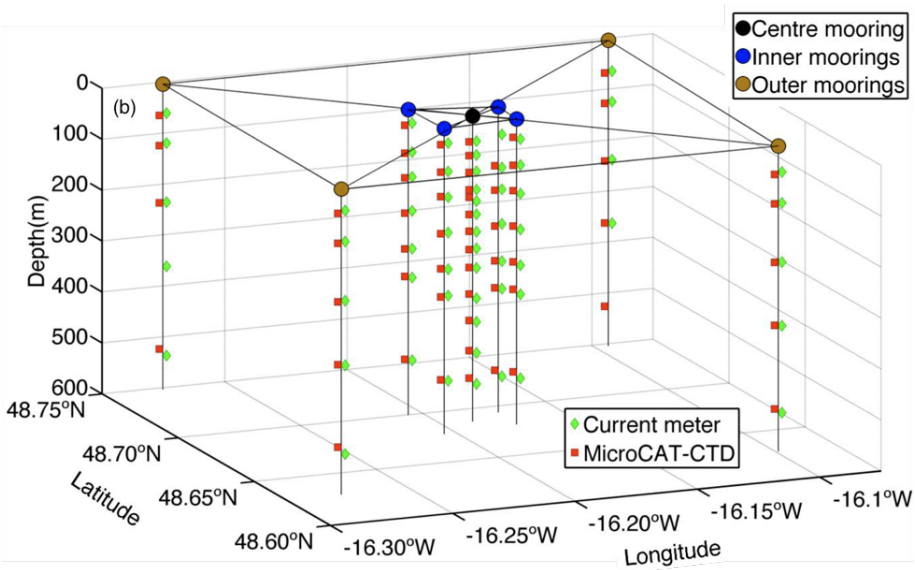

Figure 2.14: OSMOSIS mooring array and its vertical sections. The mooring array includes one central mooring (black), four inner moorings (blue) and four outer moorings (dark yellow). Current meters are shown as green diamonds, and MicroCAT-CTDs are shown as red squares. This image is taken from (Yu et al., 2019)

Location	Northeast Atlantic
Period	09/2012 - 09/2013
Instruments	Nine (9) Mooring and Two (2) gliders
Vertical levels	Moorings: 50m - 500m
Measurements	θ , S and $\mathbf{u}_h$

Table 2.2: Tabular description of OSMOSIS datasets.

outputs. A comparison of the time series of the mixed layer depth for both datasets is presented in Figure 2.15. From the plot we can deduce that NATL60 fairly reproduce the seasonality of mixed-layer depth as observed in the OSMOSIS region.

We compute the estimate of the horizontal velocity gradients from the five points mooring array by using a finite difference method (see Apendix B). A histogram of the vorticity, strain-rate, and divergence for the depth range of (60m - 180m) for a period of 11 months (Oct 2012 to August 2013) is presented in Figure 2.16. The distribution of the velocity gradients is fairly consistent between NATL60 and OSMOSIS. The model reasonably reproduced the statistics of vorticity, strain, and divergence at fine-scale as observed by the OSMOSIS outer mooring array. However, there is a likelihood of extreme divergent motions in OSMOSIS that is not captured by the model. That NATL60 underestimates divergent motions compare to observation isn't that surprising because NATL60 model simulation is without tidal forcing; one of the major sources of wave energy. This indicates that the simulation of submesoscales by NATL60 is consistent with observation in this region but

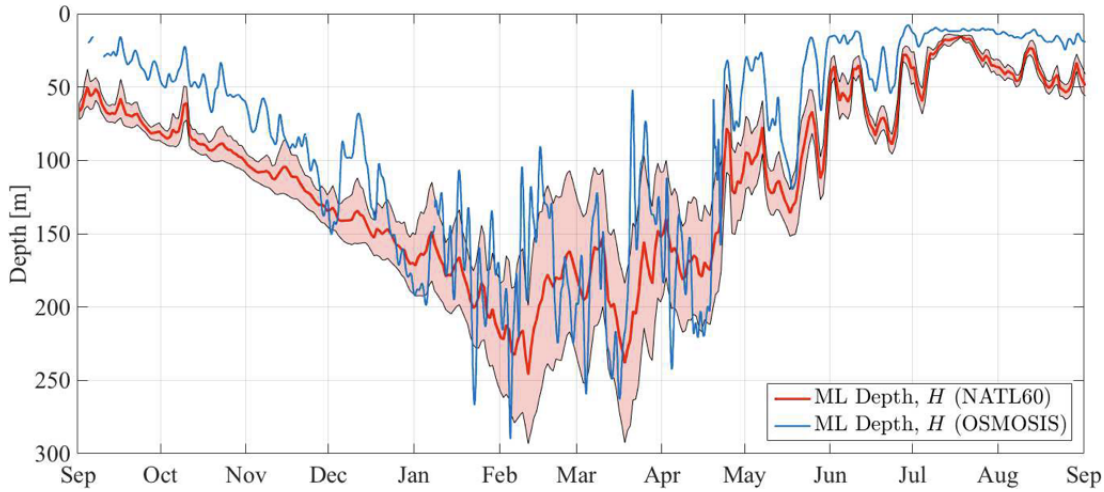

Figure 2.15: Time series of mixed layer depth for OSMOSIS and NATL60. The blue line depicts ML depths derived from OSMOSIS glider observations, while the red line and shaded region denote the NATL60 mean and ± standard deviation from the mean. Both were estimated as the depth at which the potential density exceeds its value at 10 m by 0.03 kgm^{-3}. This image is taken from Buckingham et al. (2019)

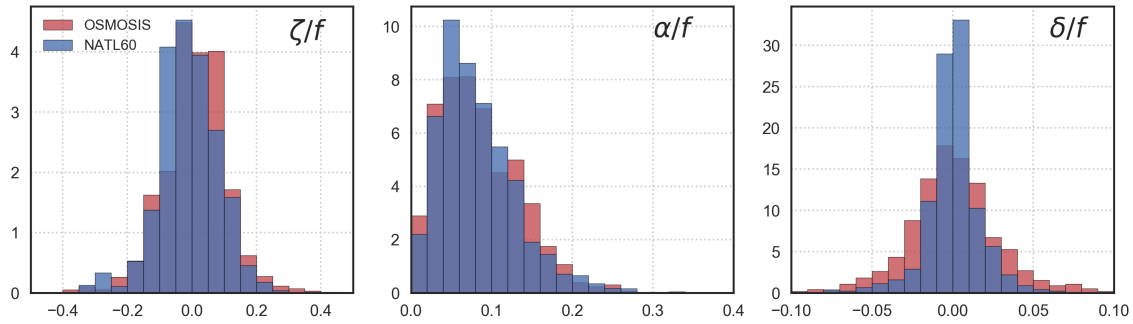

Figure 2.16: Distribution of upper ocean vorticity, strain-rate and divergence for NATL60 and HYCOM50. Depths covered : 60m - 180m.

with a weak signature of internal gravity waves.

2.4.2 Upper ocean lateral buoyancy gradients

Horizontal buoyancy gradients play a dynamical role in ocean energetic as they represent a source of available potential energy for mixed-layer instabilities and frontogenesis processes, that feed submesoscale motions (Capet et al., 2008e). In this section, we compare the statistics of horizontal buoyancy gradients in NATL60 with the observation TSG in order to evaluate the statistics of buoyancy gradients predicted by NATL60. The TSG dataset is extracted from the Global Ocean Surface Underway Data (GOSUD), which gathers three different databases: Sea Surface Salinity data from Voluntary Observing Ships Network (SNO-SSS), Sea Surface

Salinity from French RESearcH Vessels (SSS-FRESH), Sea Surface Salinity from Sailing ships (SSS-Sail).

NATL60 model has a grid size of about 2 km, which is likely to fully resolve lateral motions at scales of 10 km. Below this cutoff, the explicit dissipation already distorts motions and damps KE. TSG measurements are made every 15 seconds and delivered at 5-minute averages by taking the median. This operation yields an average spatial resolution of 2.5 km for a 20-knot cruise speed. Thus, TSG ship-track observations are able to capture temperature and salinity gradients at 10-km scales. To ensure that we focus only on 10-km horizontal gradients, NATL60 10-m depth outputs are filtered using a bi-dimensional Gaussian window with a standard deviation of $\sigma = \frac{\lambda}{2\pi}$, where λ is the cutoff wavelength set to 10 km in this case. A similar Gaussian filter is applied to ship-track TSG data to filter out smaller scales. The Gaussian kernel g is based on the distance between the coordinates at the center of the kernel (x_j, y_j) and surrounding observations (x_i, y_i), with a similar standard deviation as for NATL60 outputs. The weights of the kernel are thus defined as:

$$g_j(x_i, y_i) = e^{-\frac{(x_i - x_j)^2 + (y_i - y_j)^2}{2\sigma^2}}. \tag{2.1}$$

Only valid values are taken into account in the filtering and the kernel weights are normalized prior to the multiplication with the data. The gradients are then computed along-track and the median is taken over $1°x1°$ bins to produce maps of temperature, salinity and buoyancy gradients as shown in Figure 2.18.

The Gulf Stream pattern, associated with substantial surface tracer gradients from the US east coast to 35 W, is remarkably similar between NATL60 and TSG observations, albeit salinity and temperature gradients are weaker in observations. More interesting is the comparable amplitude of buoyancy gradients between NATL60 and TSG observations over the whole basin, suggesting that the dynamical role of temperature and salinity gradients is close between model and observations. However the amplitude of the gradients tend to be slightly underestimated in TSG dataset. This is because the ship tracks are not a priori aligned with the direction of the gradients. NATL60 also exhibits a coherent pattern of larger salinity gradients in the subtropical gyre which is not captured in TSG observations. The opposite is true around Europe - and particularly substantial around Norway and Sweden - where salinity gradients in TSG observations are larger than those estimated in NATL60. Freshwater fluxes might be underestimated in NATL60 run-off leading to weaker salinity gradients.

Overall, we find good consistency in the western side of the North Atlantic basin between NATL60 and TSG observations in terms of buoyancy gradients. There are also substantial differences between the center and the eastern side of the basin,

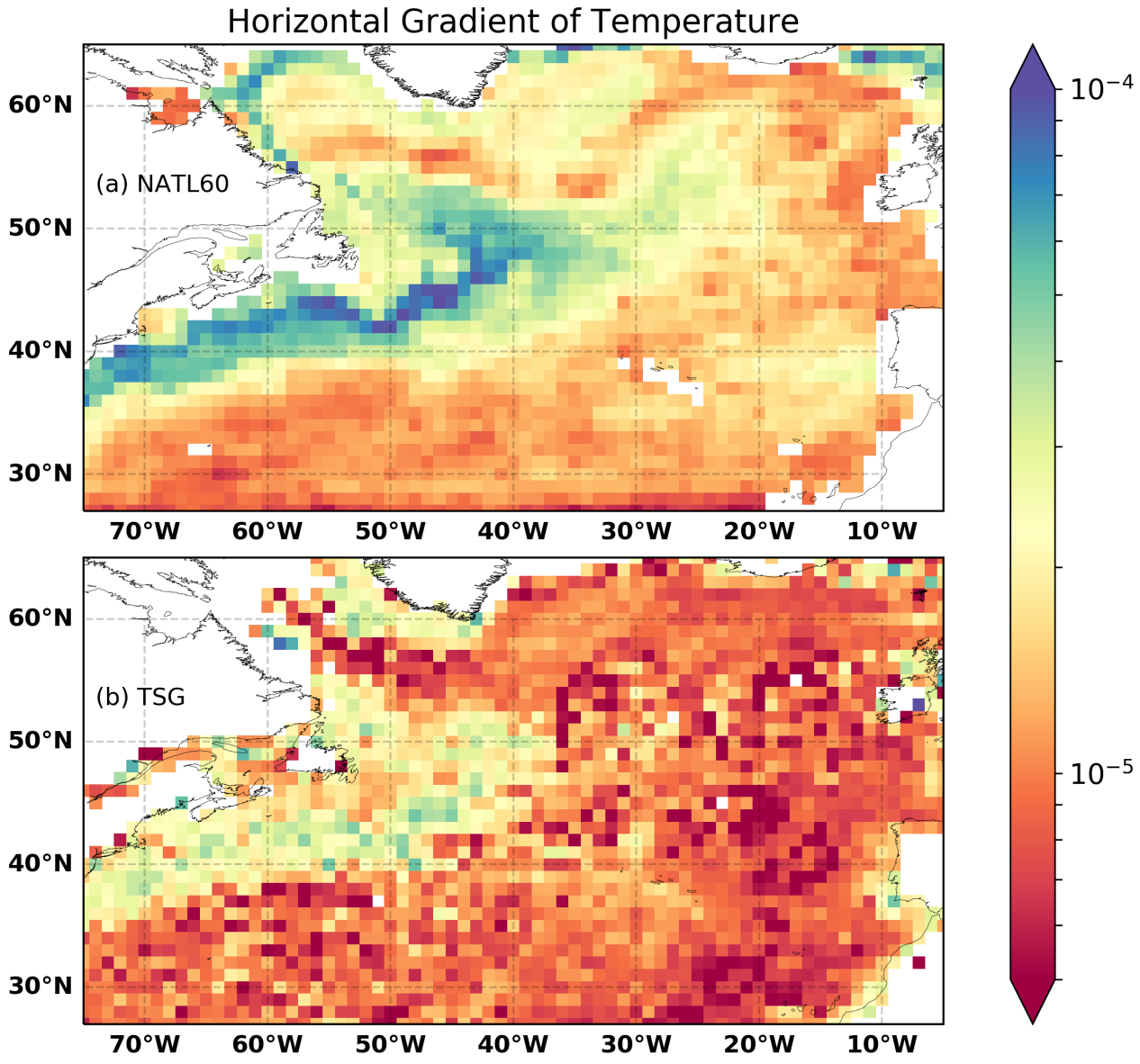

Figure 2.17: Horizontal gradient of temperature in a 2 x 2 degree boxes for (a) NATL60 and (b) TSG dataset. The analysis presented in this plot was prepared by Guillaume Serazin (UNSW)

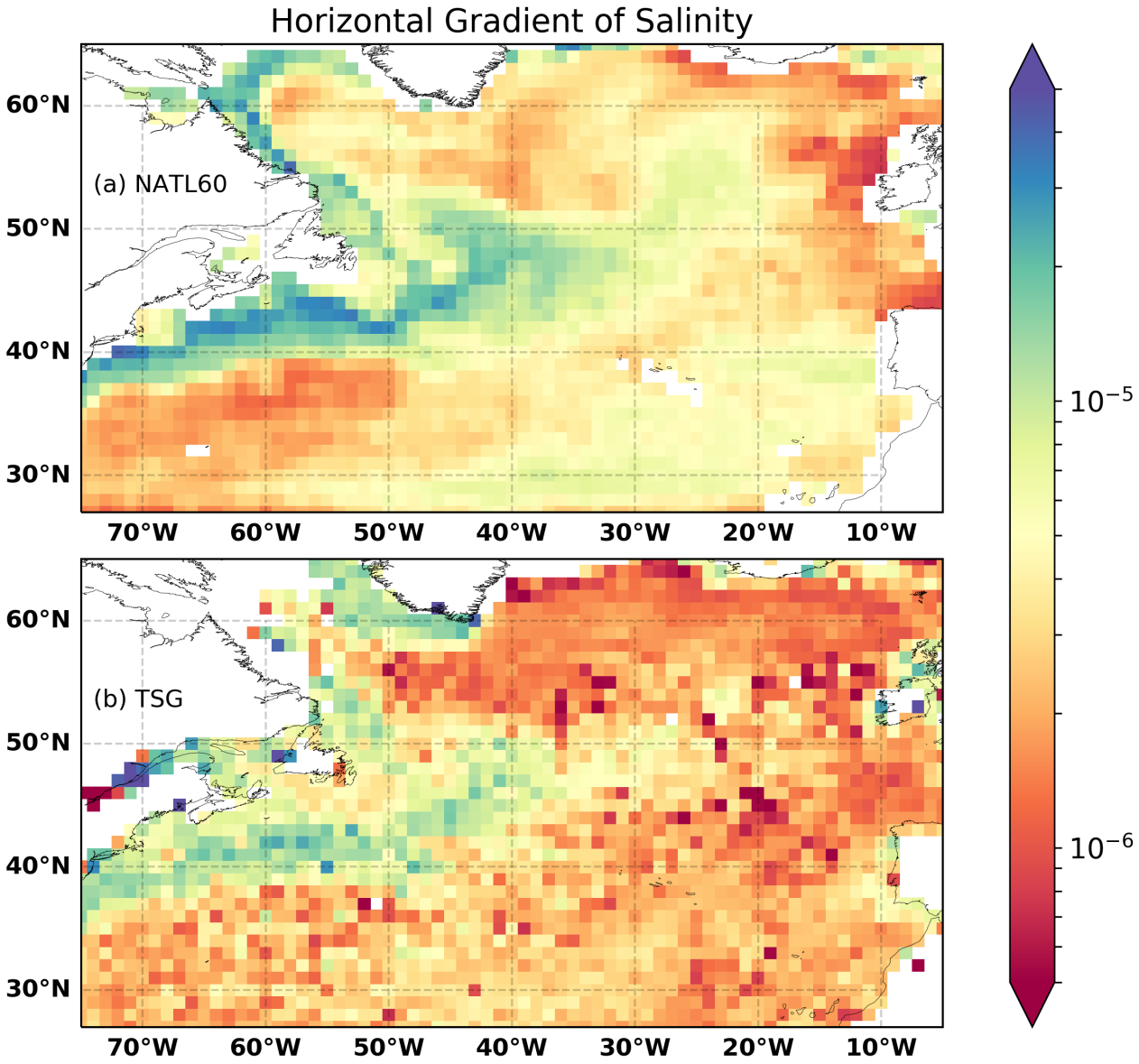

Figure 2.18: Horizontal gradient of salinity in a 2 x 2 degree boxes for (a) NATL60 and (b) TSG dataset. The analysis presented in this plot was prepared by Guillaume Serazin (UNSW)

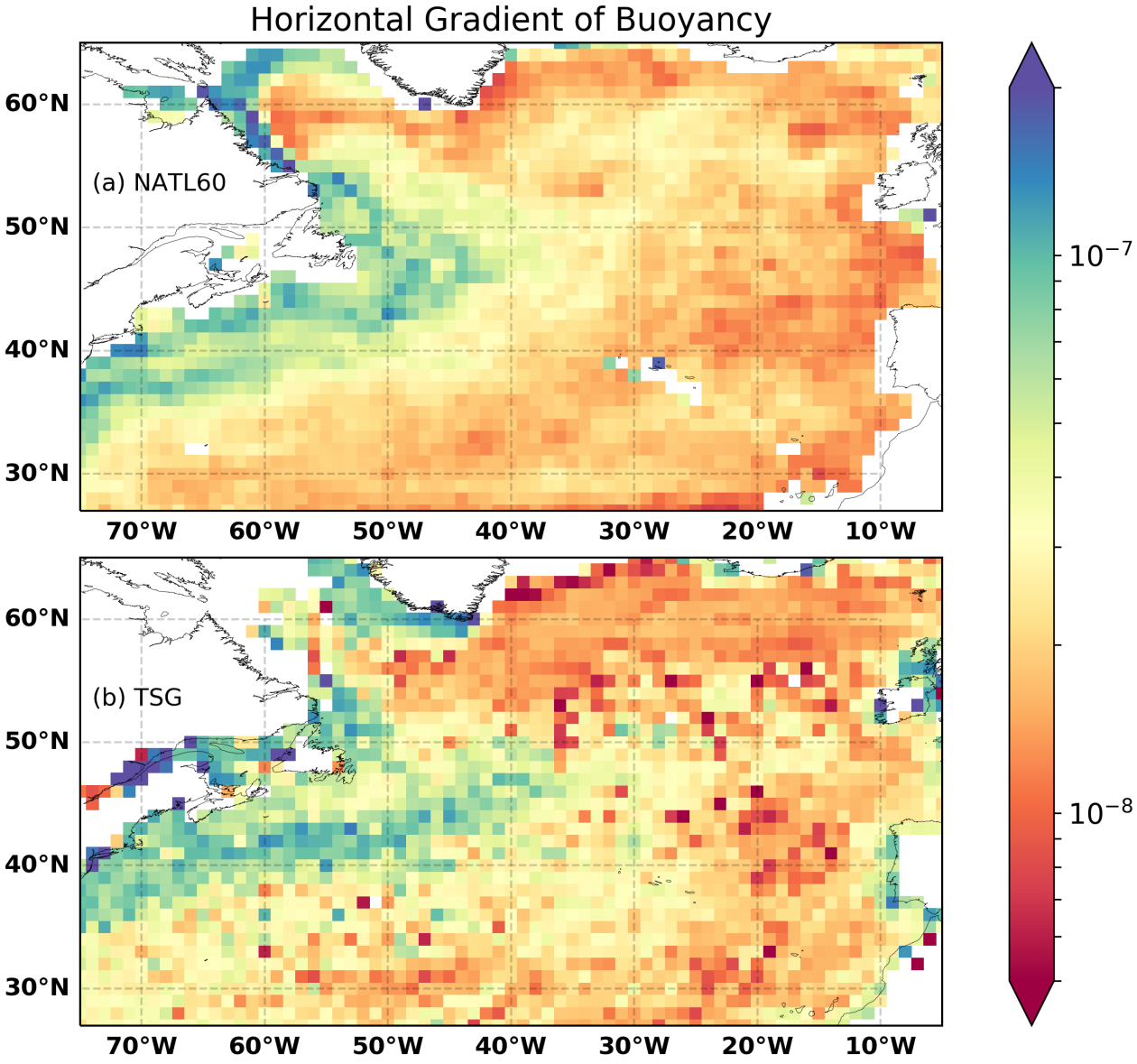

Figure 2.19: Horizontal gradient of buoyancy in a 2 x 2 degree boxes for (a) NATL60 and (b) TSG dataset. The analysis presented in this plot was prepared by Guillaume Serazin (UNSW)

suggesting that NATL60 might need some improvements in those regions.

2.5 Conclusion

In this chapter, we have described the North Atlantic simulations used in this thesis work and we have assessed the ability of NATL60 simulation to resolve fine-scale dynamics by using satellite and in-situ measurements. From our analysis, we show that both the NEMO and HYCOM based simulations have the ability to reproduce realistic basin and mesoscale circulation in the North Atlantic. The energy levels diagnosed through SSH variance is almost similar between the simulations and compares favorably with the observation from SARAL/AltiKa. The statistics of horizontal velocity gradients at 10km scale show strong agreement between NATL60 and OSMOSIS data although NATL60 might be underestimating extreme divergence events because of the lack of tidal forcing. Comparison of buoyancy gradients between NATL60 and TSG observation show great agreement as well with little differences at the eastern side of the North Atlantic basin.

Acknowledgment

We are very grateful to the engineers that designed and performed these numerical simulations. NATL60, eNATL60, and HYCOM50 simulation were performed by Jean-Marc Molines (MEOM, CNRS), Laurent Brodeau (Ocean-Next) and Xiaobiao Xu (COAS, FSU) respectively. The dataset from OSMOSIS was provided by Christian Buckingham (IFREMER) and Guillaume Serazin (CCRC,UNSW) provided & prepared the TSG-NATL60 comparisons. Laurent Brodeau provided the Model vs Satellite along-track SSH spectra comparison. Aurelie Albert (MEOM, CNRS) was involved in many aspects of data extraction and computation of useful diagnostics.

Chapter 3

Seasonal and regional distribution of fine-scale eddy structures in the North Atlantic.

Contents

3.1 Introduction

Oceanic kinetic energy is dominated by eddy motions with spatial scales ranging from 10km to 300km. The interaction between these eddies and large scale flow is an important factor in ocean circulation and kinetic energy exchanges between the different scale of motions. In non-eddy resolving ocean and climate models, this interaction is represented through parameterization scheme based on mixing length hypothesis (which uses eddy length scale and eddy velocity). The dynamics and distribution of eddies with scale $>$ 100km is well known because they are easily identified by ocean observing satellites. On the other hand, eddies with scales $<$ 100km are relatively less known due to their size. The first objective of this thesis work is to investigate the dynamics and distribution of oceanic eddies with scales $<$ 100km in the North Atlantic ocean. Given that eddy kinetic energy dominates the kinetic energy in the ocean, understanding the distribution of fine-scale eddies could give a priori information as to how energy is distributed at fine-scale in the North Atlantic ocean. This will provide a context for our future study on the impact of submesoscale turbulence on oceanic kinetic energy exchanges.

The method and the result of this chapter were prepared in the form of a manuscript and have been submitted to the Journal of Geophysical Research - Ocean with the title: *Spatial and Temporal Variability of North Atlantic Eddy Field at Scale less than 100km.* `https://doi.org/10.1002/essoar.10501076.1`

3.2 Spatial and Temporal Variability of North Atlantic Eddy Field at Scale less than 100km (Publication)

Spatial and Temporal Variability of North Atlantic Eddy Field at Scale less than 100km.

A. O. Ajayi[1], **J. Le Sommer**[1], **E. Chassignet**[2], **JM. Molines**[1], **X. Xu**[2], **A. Albert**[1], and **E. Cosme**[1]

[1]Universite Grenoble Alpes /CNRS/IGE, Grenoble, France.
[2]Florida State University, Tallahassee, USA.

This manuscript has been submitted on the 30th of October 2019, to the Journal of Geophysical Research-Oceans.

Abstract

Ocean circulation is dominated by turbulent geostrophic eddy fields with typical scales ranging from 10 km to 300 km. At mesoscales (> 50 km), the size of eddy structures varies regionally following the Rossby radius of deformation. The variability of the scale of smaller eddies is not well known due to the limitations in existing numerical simulations and satellite capability. But it is well established that oceanic flows (< 50km) generally exhibit strong seasonality. In this study, we present a basin-scale analysis of coherent structures down to 10 km in the North Atlantic Ocean using two submesoscale-permitting ocean models, a NEMO-based North Atlantic simulation with a horizontal resolution of 1/60 (NATL60) and an HYCOM-based Atlantic simulation with a horizontal resolution of 1/50 (HYCOM50). We investigate the spatial and temporal variability of the scale of eddy structures with a particular focus on eddies with scales of 10 to 100 km, and examine the impact of the seasonality of submesoscale energy on the seasonality and distribution of coherent structures in the North Atlantic. Our results show an overall good agreement between the two models in terms of surface wavenumber spectra and seasonal variability. The key findings of the paper are that (i) the mean size of ocean eddies show strong seasonality; (ii) this seasonality is associated with an increased population of submesoscale eddies ($10-50$ km) in winter; and (iii) the net release of available potential energy associated with mixed layer instability is responsible for the emergence of the increased population of submesoscale eddies in wintertime.

1 Introduction

Ocean circulation combines large ($>500\,\mathrm{km}$), meso ($50-500\,\mathrm{km}$) and submesoscale ($1-50\,\mathrm{km}$) structures that result from direct forcing and energy exchanges through nonlinear scale interactions. The ocean is a turbulent fluid and most of its energy is concentrated in geostrophically balanced eddy fields. The coherent structures that make up the eddy field are mostly generated by baroclinic instability in an intensified ocean flow (Stammer, 1997) and therefore scale with the first Rossby radius of deformation. These ubiquitous, energetic, time-dependent circulations have their signature in all aspects of ocean activities and have, therefore, been defined as the weather system of the ocean (Bryan, 2008; McWilliams, 2016).

Improving our knowledge of the scale of eddy structures is key to several applications in physical oceanography. The interaction between the eddy field and large-scale flow is one of the main drivers of ocean circulation. This interaction is presently parameterized in non-eddy resolving ocean and climate models and the parameterizations used in these models are usually derived from a mixing length hypothesis based on eddy velocity and eddy length scale to derive eddy diffusivity (Fox-Kemper et al., 2008; Bates et al., 2014). The correlation scale of mesoscale eddies is also central to the design of the inversion algorithm used in satellite remote sensing. For instance, the optimal interpolation method currently used in calibrating AVISO products takes as input correlation radii based on eddy length scales (Ducet and Traon, 2001). If the typical scale of eddies varies in time and space in the ocean, then this variability should be accounted for in ocean model parameterizations schemes and in satellite data interpolation algorithms, hence the need to document how eddy scale vary in space and time.

Satellite missions have revolutionized the way we see the Earth surface from space and continue to serve as a large-scale observational platform for modern oceanography. Satellite data are currently the major source of knowledge about oceanic eddies,their scales and their variability. A concise review of the knowledge gained from using satellite altimeters to study mesoscale eddies in the global ocean is presented in Fu et al. (2010). Early works include a regional study on the variability of mesoscale eddies using Geosat by Le Traon et al. (1990), where the authors inferred scales of eddies from the spatial autocorrelation function of observed sea surface height (SSH) fields and recorded a high variability of mesoscale eddy fields in space across the entire North Atlantic. More recently, the merging of altimeter products covering a 16-year period paved the way for the automated identification, tracking, and documentation of about 35,000 mesoscale eddies with a lifetime greater than 16 weeks (Chelton et al., 2011). This analysis confirmed that the observed eddy scales mostly fall between the first Rossby radius of deformation L_d and the Rhines scale L_d (Klocker and Abernathey, 2014). This is in agreement with Eden (2007) who

found in an eddy-permitting numerical simulation of the North Atlantic that north of 30°N eddy scales are isotropic and proportional to L_d, while south of 30°N the eddies' scales are more closely related to the L_r. The scale $\min(L_r,L_d)$ was found to be the best predictor of eddy scale over the entire North Atlantic domain.

Studies focusing on coherent eddy structures in the ocean have mostly been limited to structures with scales on the order of 100 km (Amores et al., 2018). This is largely due to the non-availability of a high-resolution global oceanic dataset for the smaller wavelength range, a consequence of the limitations of existing numerical and satellite altimetry capability (Dufau et al., 2016). That been said, several ocean models, such as the NEMO-based North Atlantic simulation with a horizontal resolution of 1/60° (NATL60) and the HYCOM-based Atlantic simulation with a horizontal resolution of 1/50° (HYCOM50), were designed in preparation for the upcoming Surface Water and Ocean Topography (SWOT) altimeter mission (Fu and Ubelmann, 2014). These simulations now have the ability to capture explicitly ocean circulation at the basin-scale down to 10 km and therefore provide a platform to investigate the variability of eddy structures at scales less than 100 km.

At scale smaller than 100 km, oceanic flows are dominated by surface-intensified energetic submesoscale motions and they include coherent vortices, fronts, and filaments. Furthermore, both observations and model simulations have shown that submesoscale motions undergo a strong seasonality with large amplitudes in winter (Callies et al., 2015a; Qiu et al., 2014; Sasaki et al., 2014; Brannigan et al., 2015; Rocha et al., 2016). The emergence in winter of submesoscale motions has been attributed to frontogenesis, wind-induced frontal instabilities, and mixed layer instability (Thomas, 2008; McWilliams, 2016). Mixed layer instability (which is associated with the weakening of surface stratification in winter conditions) has been put forward as the dominant mechanism driving the emergence of submesoscales in winter in mid-latitudes (Capet et al., 2008; Mensa et al., 2013; Qiu et al., 2014; Sasaki et al., 2014; Callies et al., 2015b).

In this paper, the emphasis is on eddies with scales < 100 km, with a focus on *coherent structures* within the 10–50 km scale range, hereafter referred to as submesoscale eddies (SMEs) (Sasaki et al., 2017). Our key objective is to investigate how resolving submesoscales affects eddy motions and their variability, specifically in terms of spatial scale and depth penetration. This paper intends to answer this question by documenting the statistics of SMEs and their overall impact on the variability of averaged eddy scales in the North Atlantic. This is done by first performing a basin-scale analysis of the spatial and temporal variability of coherent structures down to 10 km in the North Atlantic Ocean using two submesoscale resolving ocean models, NATL60 and HYCOM50. Then, we examine the impact of the seasonality of submesoscale energy on the distribution and depth penetration of eddy structures in the North Atlantic.

This paper is organized as follows: In section 2, we provide a description of the NATL60 and HYCOM50 datasets. In section 3, we present the description of eddy statistics. Sections 4 focuses on the spatial variability of eddy scales while section 5 presents the seasonality of eddy scales with insights on the impact of mixed layer instability on eddy statistics. We summarize and conclude our analysis in section 6.

2 Datasets and Methodology

2.1 North Atlantic Ocean model simulations

In this study, we use numerical outputs from two submesoscale eddy-permitting simulations of the North Atlantic: a NEMO-based North Atlantic simulation with a horizontal resolution of 1/60° (NATL60) and a HYCOM-based Atlantic simulation with a horizontal resolution of 1/50° (HYCOM50).

The NEMO-based NATL60 has a horizontal grid spacing that ranges from 1.6 km at 26°N to 0.9 km at 65°N. The grid has been designed so that the model explicitly simulates the scales of motions that will be observed by the SWOT altimetric mission. In practice, the model's effective resolution is about 10-15 km in wavelength. The initial and open boundary conditions are based on GLORYS2v3 ocean reanalysis with a relaxation zone at the northern boundary for sea-ice concentration and thickness. The model has 300 vertical levels with a resolution of 1 m at the top-most layers. The atmospheric forcing is based on DFS5.2 (Dussin et al. (2018)). The grid and bathymetry follow Ducousso et al. (2017). In order to implicitly adapt lateral viscosity and diffusivity to flow properties, a third-order upwind advection scheme is used for both momentum and tracers in the model simulation. The model is spun-up for a period of six months, and a one-year simulation output from 2012 to 2013 is used in this study. A description of the NATL60 simulation is available from Le Sommer et al. (2019) and the outputs have been used in recent studies by Fresnay et al. (2018) and Amores et al. (2018).

The HYCOM-based HYCOM50 extends from 28°S to 80°N and has a horizontal grid spacing ranging from 2.25 km at the equator, ~ 1.5 km in the Gulf Stream region, and 1 km in the subpolar gyre. As for NATL60, the effective resolution is about 10–15 km. The vertical coordinate is hybrid and consists of 32 layers. The simulation is initialized using potential temperature and salinity from the GDEM climatology and spun up from rest for 20 years using climatological atmospheric forcing from ERA-40 (Uppala et al., 2005), with 3-hourly wind anomalies from the Fleet Numerical Meteorology and Oceanography Center 3-hourly Navy Operational Global Atmospheric Prediction System (NOGAPS) for the year 2003. The year

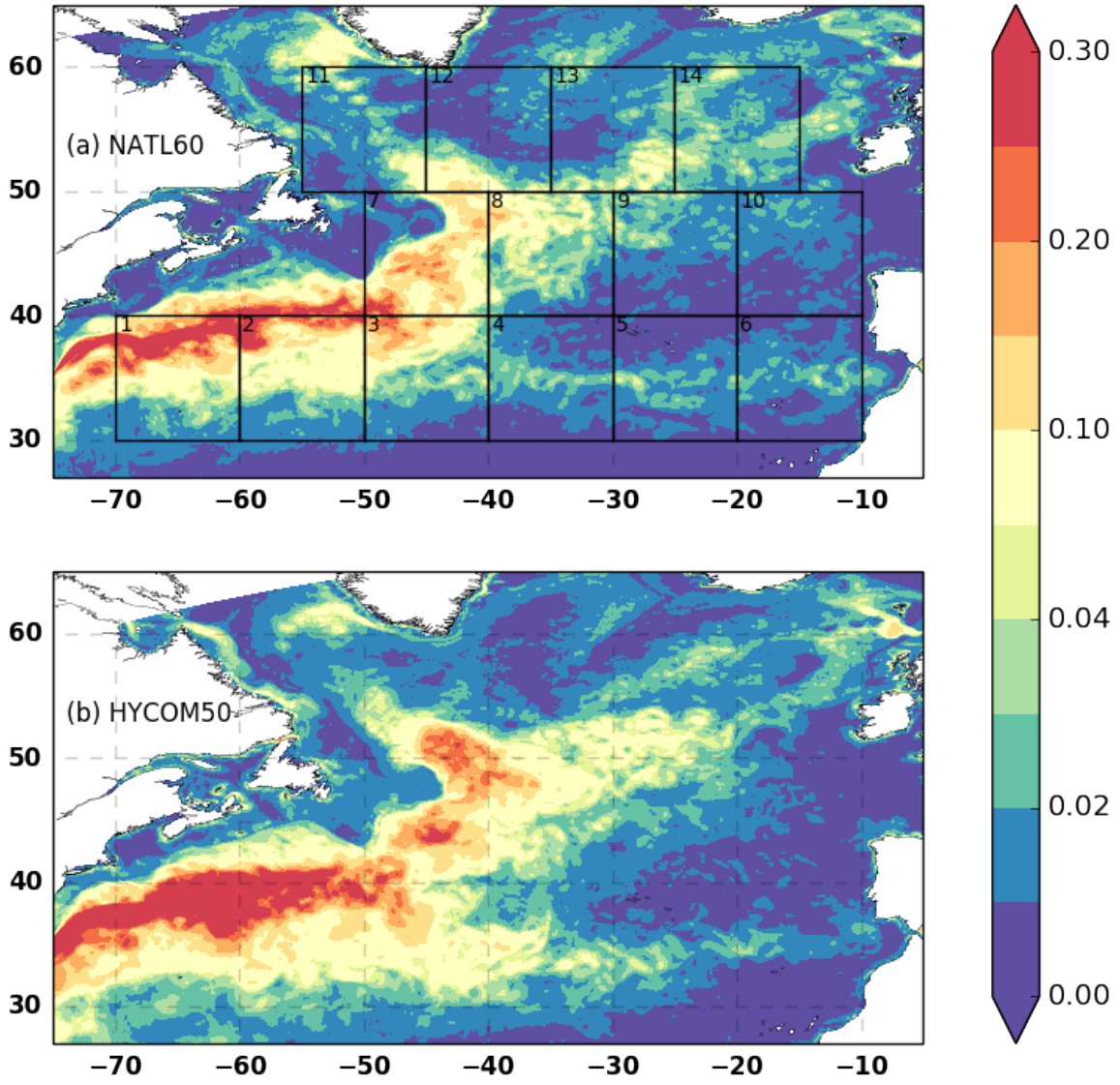

Figure 1: Surface eddy kinetic energy ($cm^2 s^{-2}$) computed from daily mean outputs of the total velocity. (a) NATL60 and (b) HYCOM50

2003 is considered to be a neutral year over the 1993 to present timeframe in terms of long-term atmospheric patterns of the North Atlantic Oscillation. The last year of the simulation is used to perform the analysis. The horizontal viscosity operator is a combination of Laplacian and Biharmonic. The bathymetry is based on the Naval Research Laboratory (NRL) digital bathymetry database. The model configuration and a detailed evaluation of the model results in the Gulf Stream region with observations are documented in Chassignet and Xu (2017).

Table 1: Table of model parameters for NATL60 and HYCOM50

	NATL60	HYCOM50
Domain	26.5N - 65N	28 - 80N
Numerical Code	Nemo v.3.6	HYCOM
Horizontal grid	1/60: 0.9-1.6 km	1/50:1.1-2.2 km
Vertical coordinate	Z partial cells	Hybrid (Z & isopycnal)
Vertical grid	300 Levels : 1-50 m	32 Layers
Boundary conditions	GLORYS2v3	GDEM
Atmospheric forcing	DFS5.2	ERA-40
Horizontal Viscosity	Implicit in momentum advection	Laplacian & Biharmonic

Both NATL60 and HYCOM50 resolve the first Rossby radius of deformation everywhere within the model domains and these simulations reproduce realistic eddy statistics with levels of kinetic energy in the range of altimetric observations (Le Sommer et al., 2019; Chassignet and Xu, 2017) (Figure 1). HYCOM50 shows a higher eddy kinetic energy (EKE) level along and around the Gulf Stream-North Atlantic Current path. The less energetic Gulf Stream-North Atlantic Current in the NATL60 simulation may be due, in part, to its shorter spin-up period (6 months versus 19 years).

A summary of the model parameters is tabulated in Table 1. In this study, we consider the outputs of HYCOM50 for exactly the same region covered by NATL60 to have comparable results and we perform statistical analysis of the model outputs in two dimensional $10^\circ \times 10^\circ$ boxes, following earlier approaches by Stammer and Böning (1992), Uchida et al. (2017), and Chassignet and Xu (2017).

2.2 Wavenumber spectra

Wavenumber spectra provide a way to quantify the variability and energy associated with motions of different spatial scales across different regions. In this study, spectral analysis is performed in subdomains of $10^\circ \times 10^\circ$ boxes across the North Atlantic in order to document regional variability. Prior to spectral analysis, the field of each box is detrended in both direction and a 50% cosine taper window (turkey

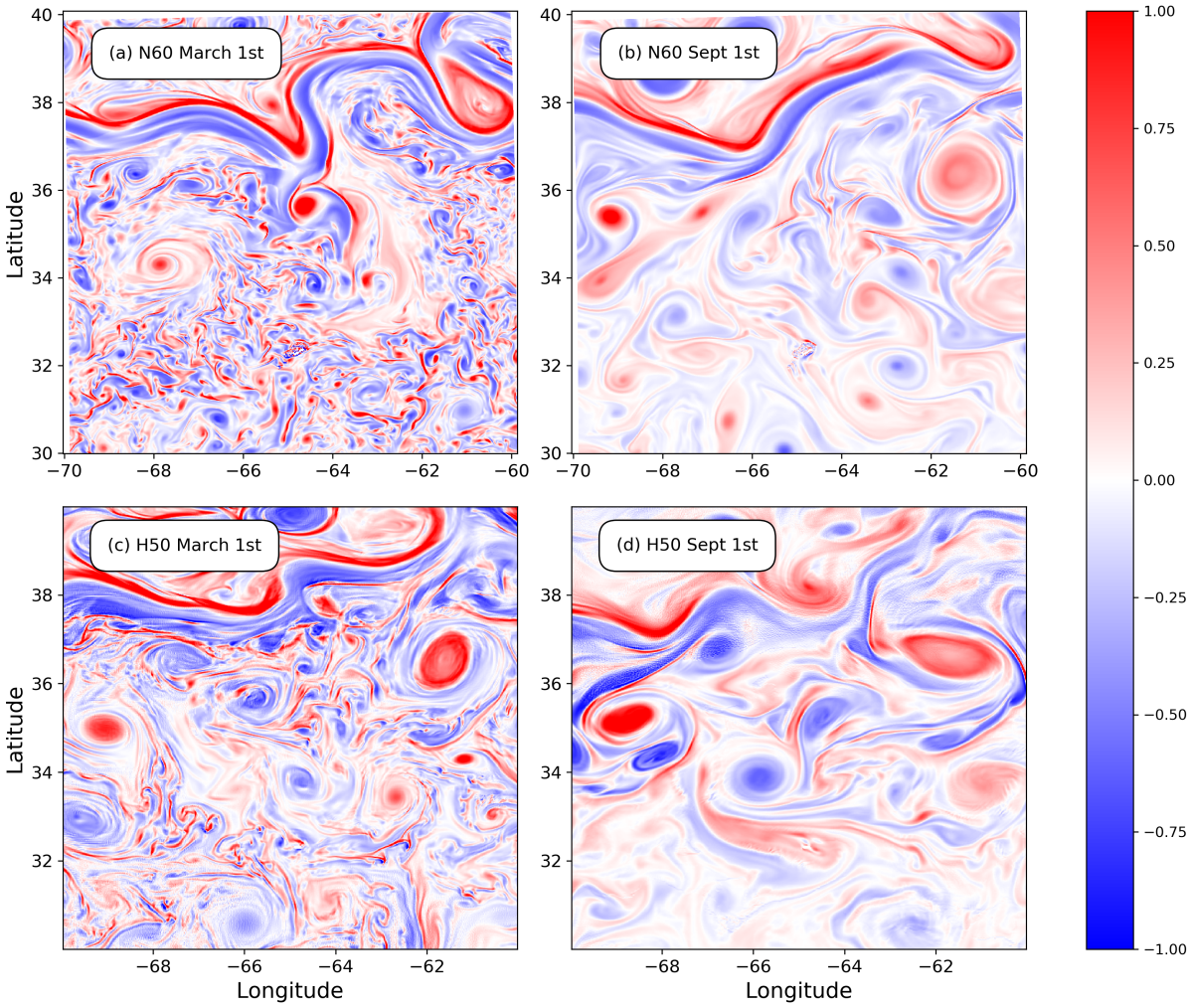

Figure 2: Seasonality of resolved vorticity field in NATL60 and HYCOM50 in Box 1

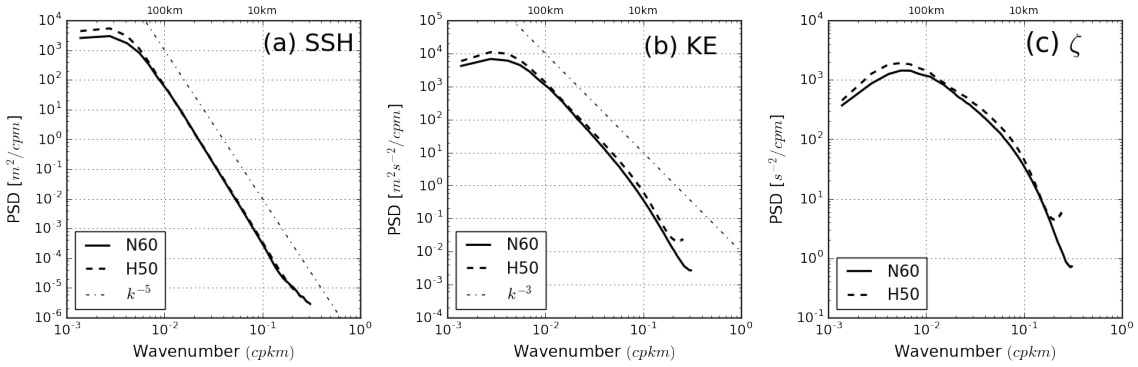

Figure 3: One year averaged wavenumber power spectra density in a 2D 10° square box (Box 1, Fig. 1) around the energetic Gulf Stream region computed from daily output of NATL60 (thick black line) and HYCOM50 (thick dash line). (a) SSH (b) surface KE from total velocity (c) surface relative vorticity.

windowing) is applied for tapering. a Fast Fourrier Transform (FFT) is applied to the tapered data and a one-dimensional isotropic spectrum is obtained by averaging over azimuthal directions. Our spectral approach is in line with Chassignet and Xu (2017) and because we are making use of year 20 of the HYCOM50 simulation used in Chassignet and Xu (2017), we were able to compare our SSH wavenumber spectra estimates with the already published results for the same dataset and found our result to be consistent as well (not shown).

Figure 3 shows the wavenumber power spectral density for SSH, surface kinetic energy (KE), and surface relative vorticity (RV) in a region close to the Gulf Stream (Box 1, as defined in Figure 1) for the two datasets. The wavenumber power spectra from the two models agree well, indicating that the distribution of energy across scales is similar in both models. The estimated slope from the SSH and KE spectra indicates that the two models agree with quasigeostrophic dynamics, which predict a slope of k^{-5} and k^{-3} for SSH and KE spectra, respectively. This agreement is particularly strong for the wavelength band of $10-100$ km. HYCOM50 shows more variance at low wavenumbers compare to NATL60. This is consistent with the lower EKE in NATL60 compared to HYCOM50 at these scales (Figure 1).

In Figure 4, we present the seasonality of SSH, KE, and RV wavenumber power spectral density. At scales smaller than 100 km, the variance of SSH, KE, and RV is of higher magnitude in winter (January, February, and March) compared to summer (July, August, and September). Whereas, the variance associated with scales larger than 100 km has a higher magnitude in the summer compared to winter. This winter-to-summer contrast is more pronounced in RV wavenumber spectra and is usually more visible in a winter-summer contrast of a RV snapshot (Figure 2).

The overall assessment shows that NATL60 and HYCOM50 agree reasonably well with each other on the dynamics governing the ocean surface. The small mismatch

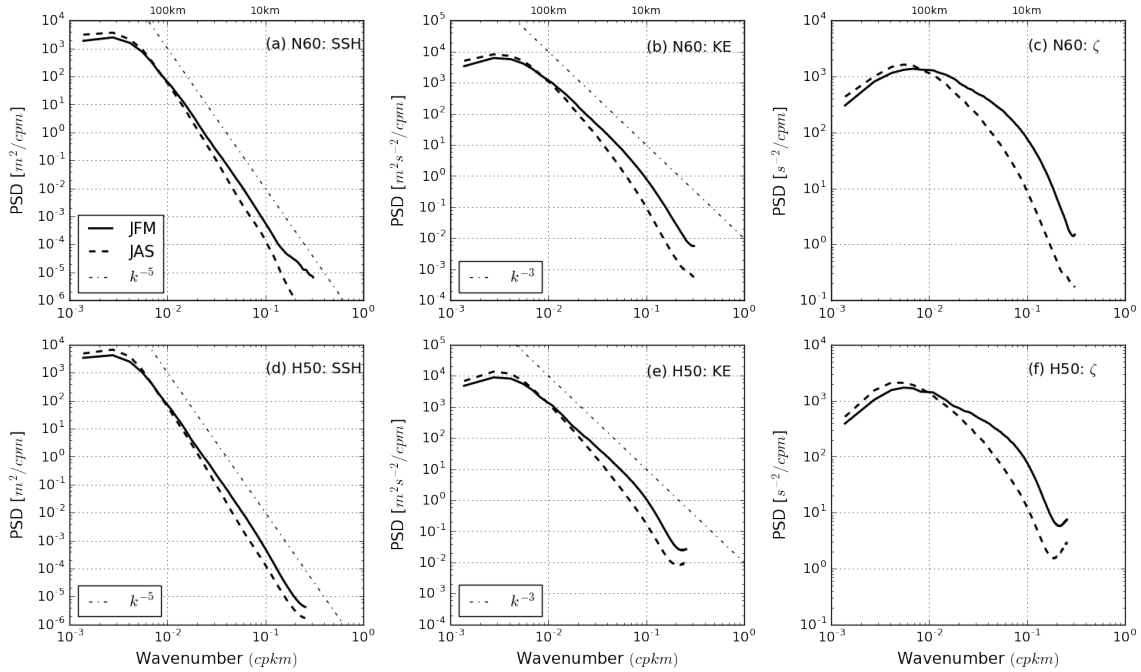

Figure 4: Winter (JFM) (thick black line) and summer (JAS) (thick dash line) wavenumber power spectra density in a 2D 10° square box (Box 1, Fig 1) around the energetic Gulf Stream region computed from daily output of NATL60 and HYCOM50.

between the result of the models may be a function of the differences in the model parameters and the length of their spin-up. In the next section, we focus on describing the statistics of eddy scales as seen in the two simulations.

2.3 Eddy length scale metric

A well-known approach for describing turbulent oceanic flows is to identify the typical length scale of motion that characterizes the dynamics of the flow. This involves computing the integral length scale of the energy-containing eddies (Qiu et al., 2014; Moum, 1996) or the enstrophy-containing scale (Scott, 2001; Morris and Foss, 2005) from the velocity and vorticity wavenumber spectrum, respectively. These length scales in physical space correspond to the scale of the most energetic eddy structures and are roughly consistent with the averaged scale of eddies that can be identified by eddy detection algorithms (Stammer, 1997; Chelton et al., 2007, 2011).

In this paper, we measure averaged eddy scales in each of our study regions by estimating the enstrophy-containing scale L_ζ from the vorticity wavenumber power spectra density following Scott (2001). The vorticity wavenumber spectral density is estimated (as described in section 2.2) using surface relative vorticity computed from the daily averaged model outputs. The enstrophy-containing scale is the enstrophy

weighted mean scale defined in equation (1) and it represents the scale of the most intense vortical structure in that flow. In equation (1), Z(k, l) denotes the vorticity wavenumber power spectral density, while k and l are the zonal and meridional wavenumber, respectively.

$$L_\zeta = \frac{\int\int Z(k,l)dkdl}{\int\int \sqrt{k^2+l^2}Z(k,l)dkdl} \tag{1}$$

To describe the distribution of the individual coherent eddy structures, we used an automated eddy detection algorithm. The algorithm detects coherent eddies by identifying closed SSH contours. A closed contour is then identified as an eddy if it satisfies some specific criteria with regards to its amplitude, number of pixels, the existence of at least one local extremum, etc. The successful application of the algorithm is documented in Chelton et al. (2011). This method is hereafter referred to as C11 and the corresponding eddy scale is referred to as L_η. We applied C11 to daily averages of SSH in two-dimensional 10° boxes for a period of one year. The implementation of the C11 algorithm in Python is available online at https://github.com/chrisb13/eddyTracking.

3 Description of eddy statistics

In this section, we present the variability of eddy statistics across the North Atlantic as diagnosed from the vorticity wavenumber spectra. The analysis is presented for both winter (January, February, and March) and summer (July, August, and September) in two regions: the Gulf Stream extension (Box 1) and the Labrador sea (Box 11). These two boxes were selected based on the fact that Box 1 is a well-documented high EKE region (Mensa et al., 2013) while Box 11 (a relatively low EKE region compare to Box 1) is a region with a very deep mixed layer in winter and energetic submesoscale activities.

In Figure 5, we show the vorticity wavenumber spectra for winter and summer in Box 1 and Box 11. In both boxes, vorticity wavenumber spectra vary notably from winter to summer, with the peak and enstrophy-containing scale (thick dot) of the spectra shifting to finer scales in winter. This change is evident in both models and in both regions. Similarly, the magnitude of the enstrophy-containing scale and spectra density vary from one region to another. The enstrophy-containing scale in Box 1 is of higher wavelength compared to Box 11. This type of regional difference in the spectra estimates and its weighted scale represents the spatial variability associated with the energy of the vortical structures across the North Atlantic. Regardless of the model or region, the winter spectra are shallower compared to the summer

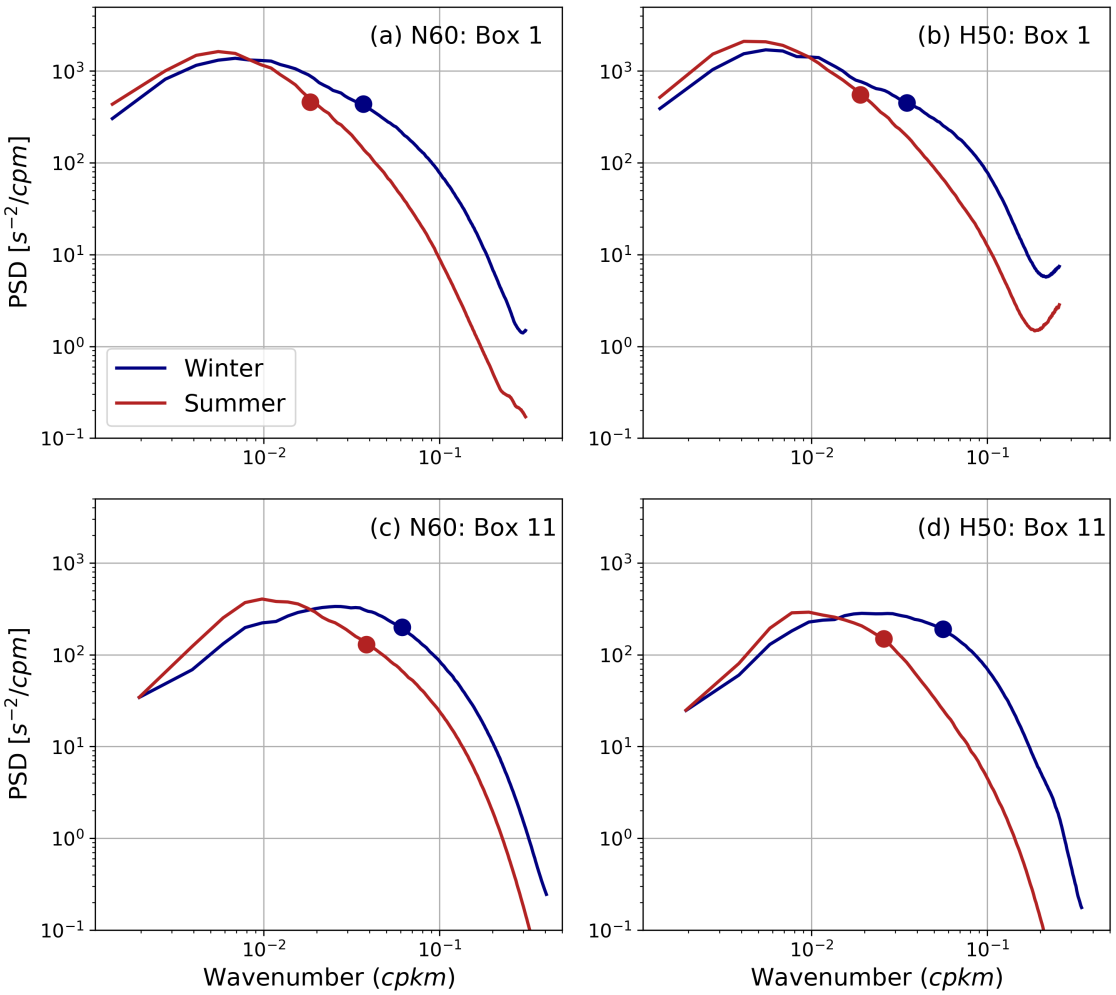

Figure 5: Surface relative vorticity wavenumber spectra for box 1 and box 11 (box defined in Figure 1), calculated from daily averages for winter time, JFM (red line) and summer time, JAS (blue line). Thick dot represent enstrophy-containing scale for each spectra. (a) NATL60 Box 1 (b) HYCOM50 Box 1 (c) NATL60 Box 11 (d) HYCOM50 Box 11.

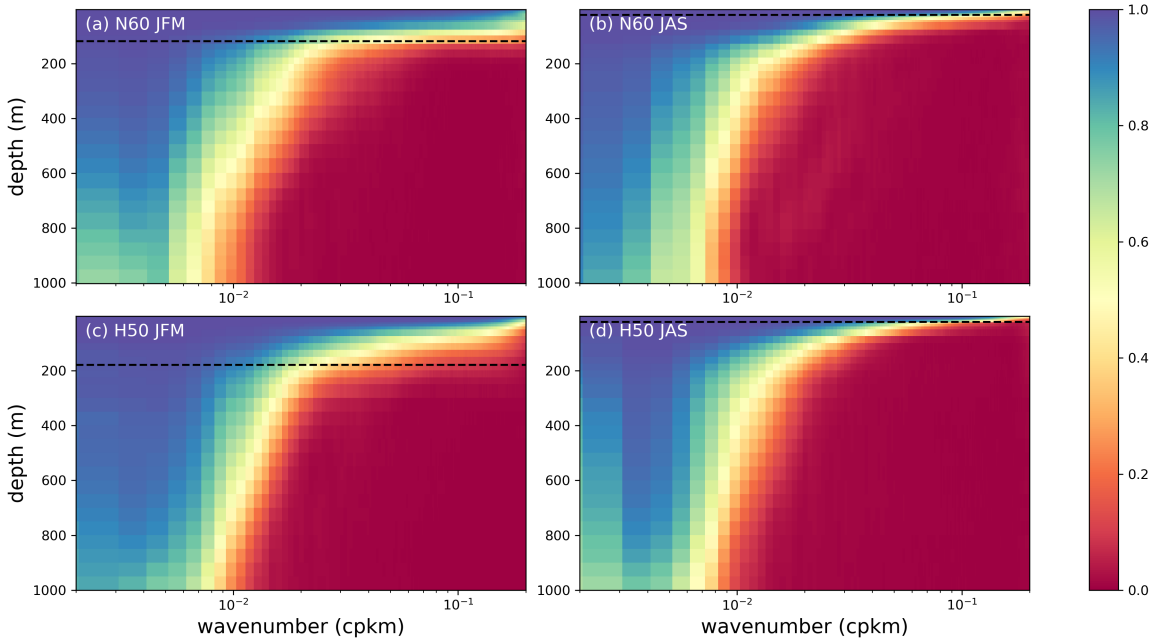

Figure 6: Winter and summer averages of vorticity spectral coherence as a function of depth for NATL60 and HYCOM50 in Box 1.

spectra (Figure 5), which indicates that energetic structures occupy a wider range of scales in winter. Also in winter, eddy motions with scales around 30 km can be as energetic as eddy motions with scales around 100 km.

In order to characterize the depth penetration of eddy structures, we estimate for typical length scale the phase relationship between the vorticity spectral density at the surface and in the interior down to 1000 m. This spectral correlation provides a proxy for the depth penetration of energetic surface structures (Klein et al., 2009). In Figure 6, we present the winter and summer averages of spectral correlation of vorticity in Box 1 for the two simulations. In both seasons and in the two models, we see that energetic motions with a scale larger than 100 km are strongly correlated down to a depth of about 1000 m. On the other hand, scales smaller than 100 km penetrate less into the water column with an observed seasonality. In fact, at these scales, surface motions are correlated with the interior roughly down to 170 m in winter and down to 40 m in summer. Scales of motions less than 50 km tend to penetrate slightly deeper into the water column in NATL60. These summer and winter depth penetration values coincide fairly with the average mixed layer depth in the two seasons. This indicates that mixed layer instability could be a possible modulator of the vertical structure of fine-scale eddy motions. Overall, despite the differences in vertical resolution (300 vertical z levels in NATL60 and 36 hybrid isopycnal layers in HYCOM50), it is worth noting that the two simulations agree fairly well in terms of the depth penetration of eddies.

In order to explain the seasonality of the enstrophy-containing scale in terms of the statistics of isolated eddy structures, Figure 7 shows the distribution of eddy scales obtained from the application of C11 to SSH fields. The histogram show eddies with a lifetime greater than ten (10) days, in order to filter out short-lived features wrongly identified as eddies by the algorithm. In the plot, the seasonal differences in the distributions of the scales of eddies are more pronounced for eddies with scales smaller than 50 km. Following our definition of submesoscales eddies (SMEs) as eddies with scales from 10 km to 50 km, we find that the seasonality of enstrophy-containing scale is attributed to an increased population of SMEs in winter. This information is supported by our analysis for both models across the North Atlantic and is, therefore, a robust signal.

The increase in the number of detected SMEs in winter corroborates the large variance at a high wavenumber in the vorticity spectra (Figure 5). However, we should note that the information about SME seasonality from the application of C11 highlights only the coherent structures, while the results of the spectra at a high wavenumber might include the vorticity variance coming from fronts, filaments, and all other active submesoscales features other than coherent vortices.

Noticeable in Figure 7 is the discrepancy in the tails of eddy scale distribution. In particular, there are more large-scale eddies (> 50 km) in HYCOM50 compare to NATL60. This difference, observed in most of the boxes, may be due to the difference in the choices of the sub-grid closures used in the models and/or, as discussed later, evidence of a stronger inverse energy cascade in HYCOM50.

4 Spatial variability of eddy scale

The spatial variability of the eddy scale is documented by computing the annual mean of the enstrophy-containing scale (L_ζ) computed from daily relative vorticity spectra for each box. The values of the mean length scale in each of the boxes for the two models is presented in Figure 8. The averaged scale varies spatially with a factor of about 2 as you move from the south to north in the North Atlantic. This spatial variability is consistent in the two models, but HYCOM50 has an annual mean scale slightly larger than NATL60 in almost all the boxes. This is consistent with what is observed in Figure 7 where typical eddy scales are larger in HYCOM50 than in NATL60.

To better understand how the eddy scales compare with the Rossby radius of deformation, we present in Figure 9 a plot of the annual mean of L_ζ versus the estimate of the first Rossby radius of deformation. The deformation radius is estimated using the GLORYS2v3 datasets following the approach highlighted in Chelton et al.

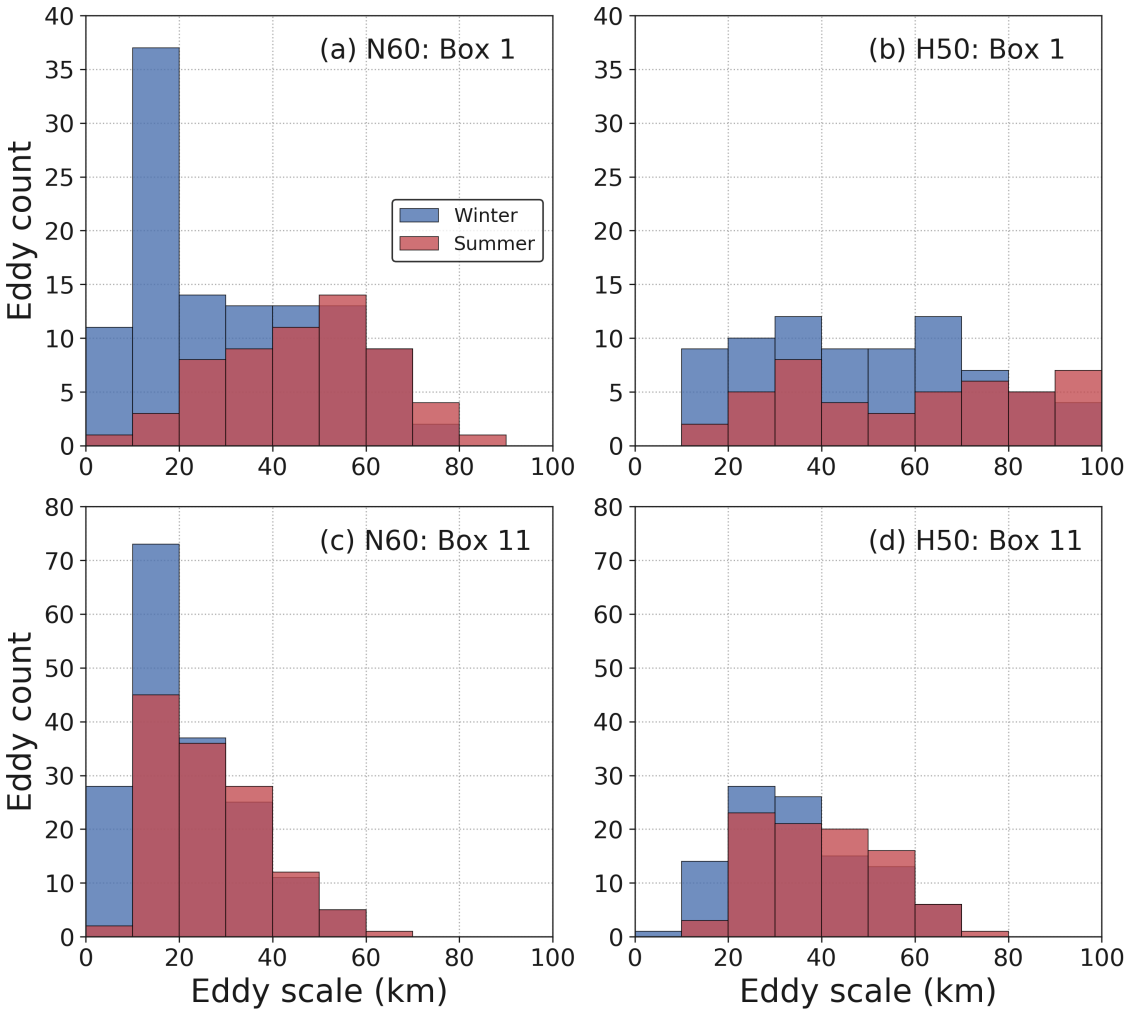

Figure 7: Histogram of eddy scale from eddy detection algorithm for box 1 and box 11 (defined in Figure 1), for winter time, JFM (red line) and summer time, JAS (blue line). (a) NATL60, Box 1 (b) HYCOM50, Box 1 (c) NATL60, Box 11 (d) HYCOM50, Box 11.

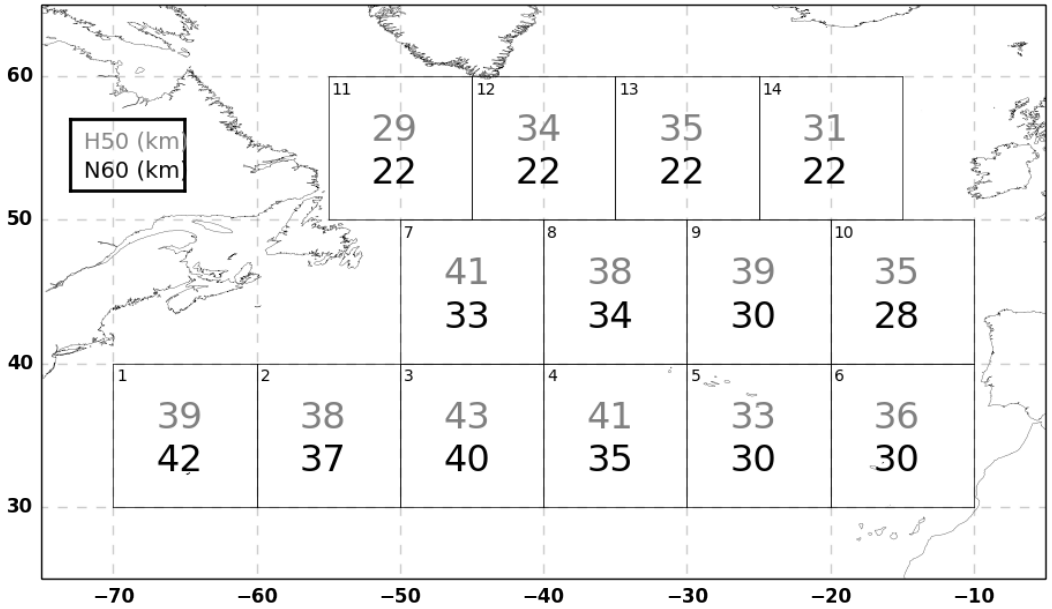

Figure 8: Map of one year averaged eddy scale (L_ζ) in all the 2D 10° boxes for NATL60 and HYCOM50

(1998). The spatial variability of the annually averaged scale is consistent with the estimate of the Rossby radius of deformation (L_d) with latitude (Figure 9). The length scales from HYCOM50 show less variability and this is evident in the slope of the fitted line plot (grey dash line). The slope for the annual averaged eddy scale is steeper for NATL60 (0.70) and shallower for HYCOM50 (0.27). The averaged eddy scale in winter is roughly consistent in the two models, while the difference in the annual mean of eddy scale between the two models is largely due to the difference in the scale of eddies in summer.

Following Klocker et al. (2016), we present a regime diagram for eddies identified from the application of C11 to SSH fields. The regime diagram presents a plot of eddy scale (L_η) normalised by the Rossby radius of deformation against a nonlinearity parameter ($r = U/c$) computed as the ratio of the root mean squared eddy velocity (U) and the Rossby wave phase speed ($c = \beta L_d^2$). The eddy velocity used in this study is the characteristic flow speed (U) within the eddy which is defined as the average geostrophic speed within the eddy interior (Chelton et al., 2007). $U = (g/f)(A/L)$, where g is the gravitational acceleration, f is the Coriolis parameter, A is the eddy amplitude and L is the effective radius of the eddy.

The regime diagram introduces frontiers along which the dynamical behavior of eddies is expected to change significantly (Klocker et al., 2016). Two different boundaries are considered in this study: (i) rotation dominated ($L/Ld < 1$) to stratification dominated ($L/Ld > 1$) and (ii) weak to strong Rossby elasticity which is represented by the Rhines scale (L_r). Figure 10 presents a kernel density plot

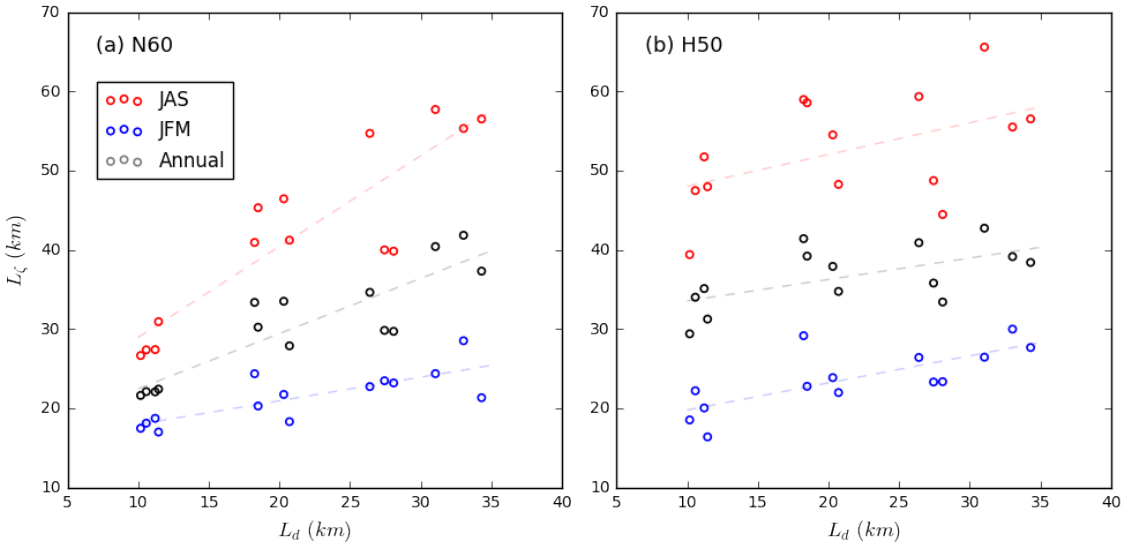

Figure 9: Eddy length scale L_ζ versus first baroclinic Rossby radius L_d. (a) NATL60 and (b) HYCOM50. Dash line represents estimated regression line and each circle corresponds to a averaged eddy scale in a box.

and describes the relative position of eddies (as a function of eddy nonlinearity) to L_d and L_r. The first baroclinic Rossby radius of deformation defines the length scale of variability over which the internal vortex stretching is more important than relative vorticity (Chelton et al., 1998), while the Rhines scale can be thought of as a threshold of scale at which the inverse cascade of energy is arrested. The Rhines scale can also be interpreted as the scale where the dispersion of Rossby wave begins to dominate the ocean signal (Rhines, 1975).

Most of the detected eddies are nonlinear and the spread of eddy nonlinearity increases with latitude. The eddy scales lie between L_d and L_r which is consistent with the findings of Eden (2007), but the scales mostly follow the L_d for NATL60 (Figure 10a) while most scales in HYCOM50 are much bigger than L_d (Figure 10b). This difference follows from the argument presented in section 4 with regard to the abundance of eddies with larger scales in HYCOM50. Also, eddies in the 55^oN latitude band (grey shading) are more nonlinear in NATL60 compared to HYCOM50. One explanation could be that 55^oN latitude eddies in HYCOM50 are more elastic due to their bigger size (w.r.t to NATL60) and thus have smaller speed magnitude and hence smaller nonlinearity compared to NATL60. This could be interpreted as evidence of a stronger inverse cascade in HYCOM50, possibly because of the longer spin-up phase. The result from NATL60 is similar to that of Eden (2007) where the author argued that north of the 30°N, the eddy length scale should follow the Rossby radius of deformation and not the Rhines scale.

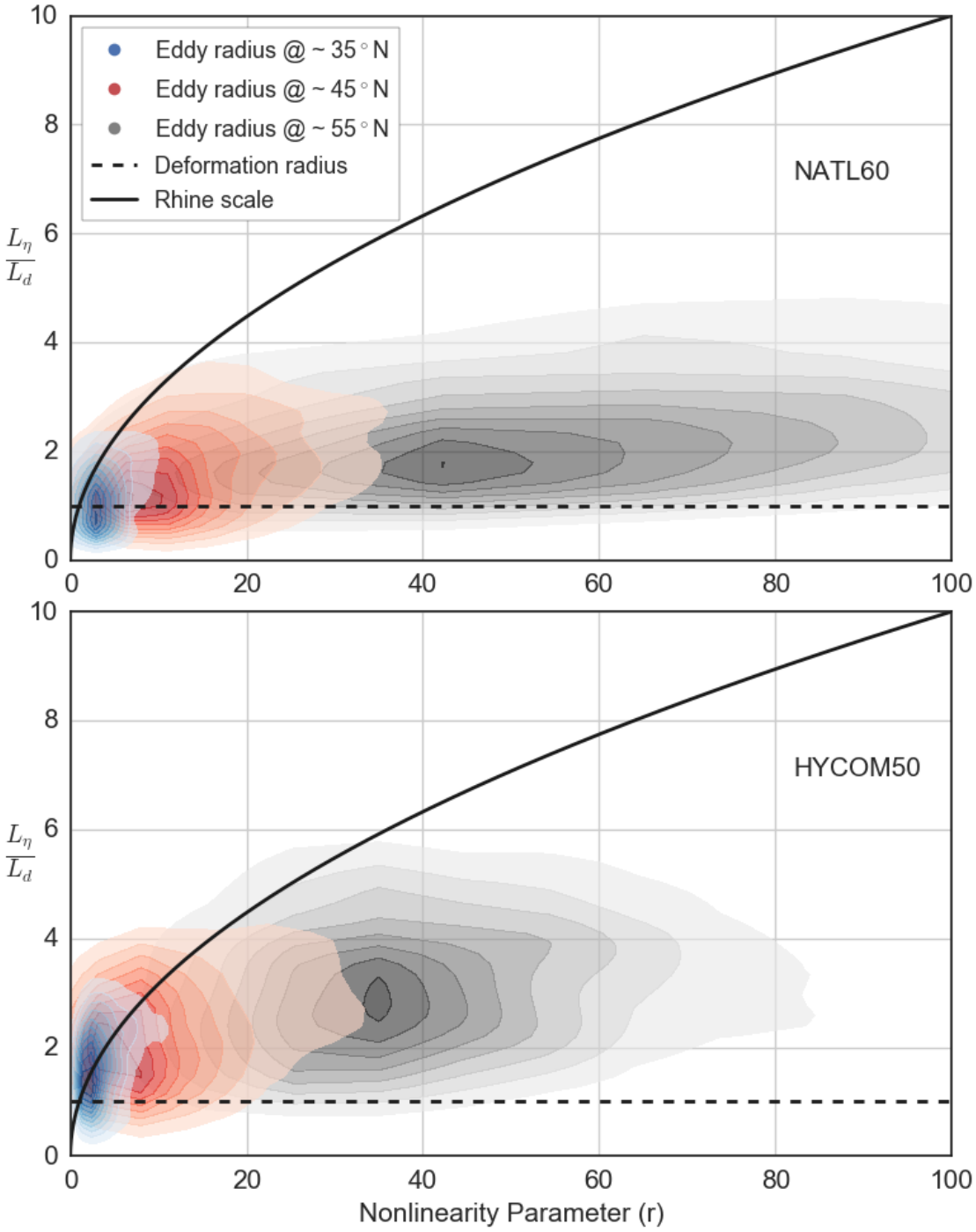

Figure 10: Kernel density plot of eddy nonlinearity (r) versus normalised eddy scale L_η/L_d for eddies identified by the automated eddy detection algorithm. The nonlinearity parameter (r) is defined as r = U/c following Chelton et al 2007. Colour blue, red and grey represents eddies in the 35°, 45°, and 55° latitudinal band. This regime diagram is adapted from Klocker et al. (2016). This plot combines data corresponding to 4680 and 3755 detected eddy structures for NATL60 and HYCOM50 respectively.

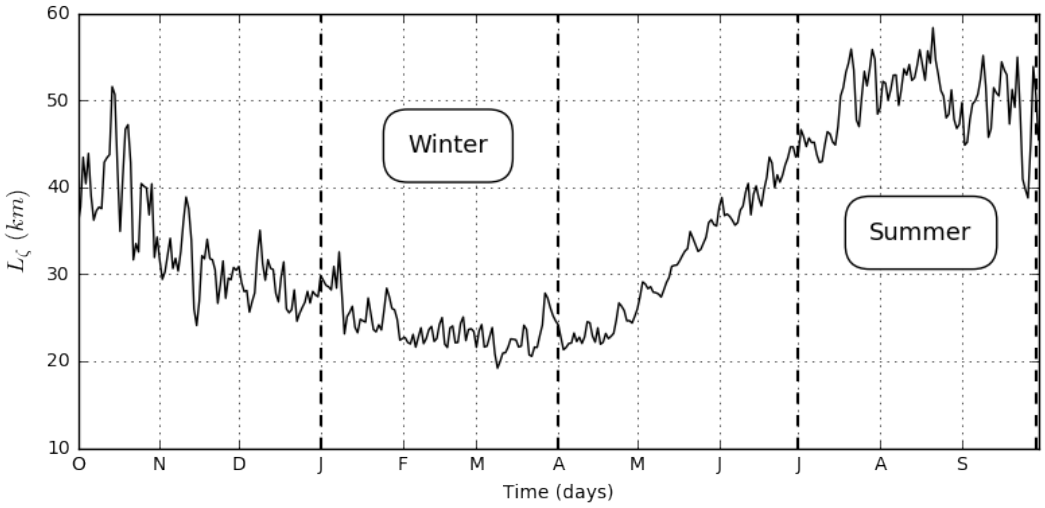

Figure 11: Time series of the enstrophy containing scale L_ζ for Box 1 (NATL60 dataset). The enstrophy containing scale is the enstrophy weighted mean scale defined in equation (1)

5 Temporal variability of eddy scale

In section 3 we established that scales of eddies undergo seasonal variability in the North Atlantic and that this seasonality is as a result of an increased population of submesoscale eddies ($10-50$ km) in winter. In Figure 11, we show the time series of L_ζ in Box 1, which illustrates the seasonality of eddy scale as captured by the enstrophy-containing scale defined in Equation (1). This seasonality is pronounced everywhere in the North Atlantic, as shown in Figure 12: The averaged eddy scale of L_ζ is about a factor of two larger in summer compared to winter. This reduction in scale from summer to winter is expected because there are more SMEs in winter and that results to smaller averaged eddy scales in winter.

So far we have shown that the average eddy scale varies in time across the entire North Atlantic following the seasonality of the number of SMEs. In what follows, we study the mechanism responsible for the seasonanlity of eddies from a dynamical point of view. Submesoscales are more active in wintertime (Thompson et al., 2016). Their emergence is believed to be driven by mechanisms such as frontogenesis, wind-induced frontal instabilities, and mixed layer instability among other processes (Thomas, 2008; McWilliams, 2016). Recent studies have identified baroclinic mixed layer instability (a specific frontal instability occurring in regions with a deep mixed layer and intense horizontal buoyancy gradients) as the dominant mechanism driving the emergence of submesoscale turbulence at mid-latitudes (Boccaletti et al., 2007; Fox-Kemper et al., 2008; Capet et al., 2008; Mensa et al., 2013; Sasaki et al., 2017)). Also, Uchida et al. (2017), using a mesoscale permitting ocean model on a global scale, surmised that mesoscale seasonality is a direct result of an inverse cascade

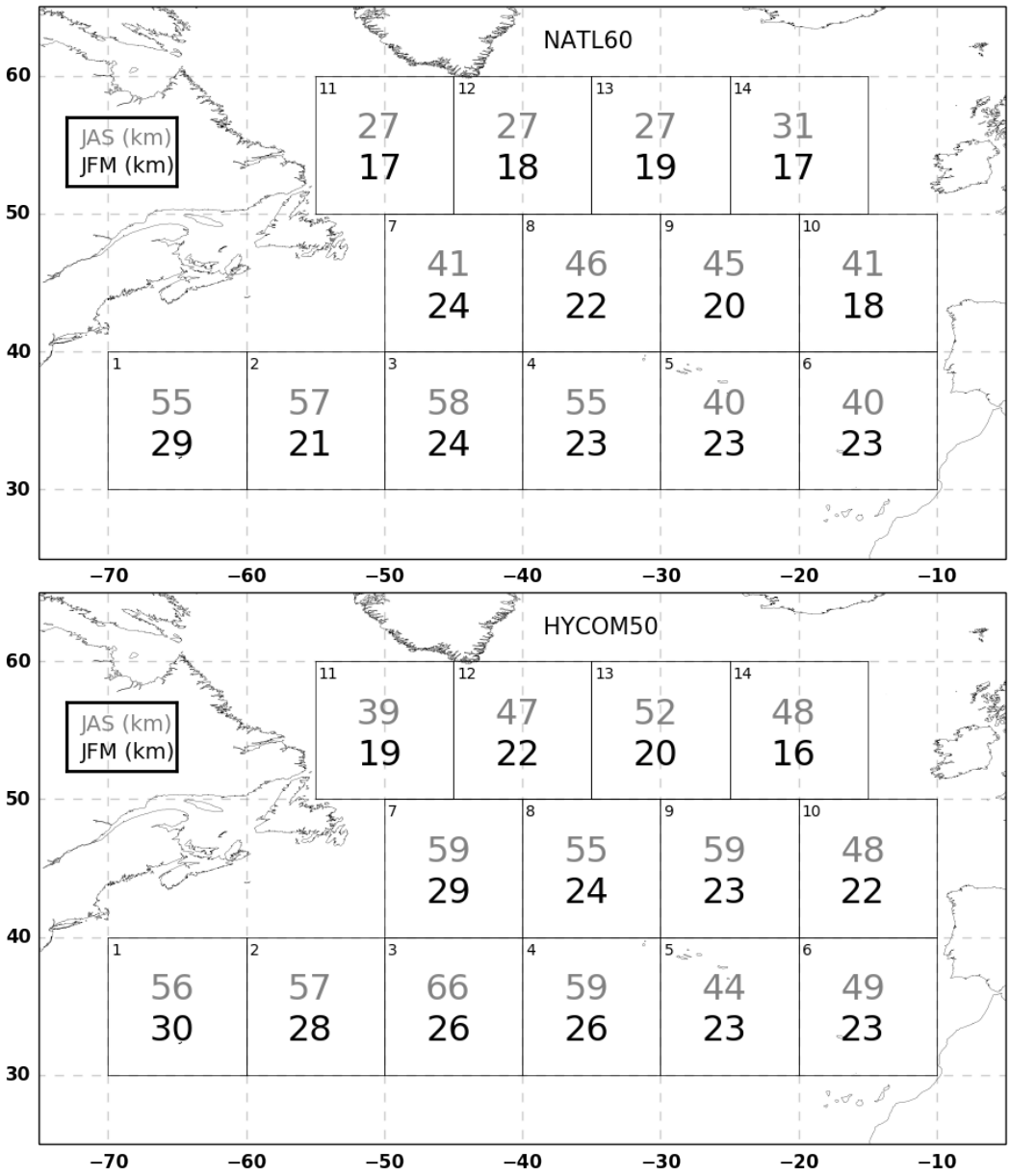

Figure 12: Map of averaged eddy length scale (L_ζ) in winter (JFM) and summer (JAS). (a) NATL60 and (b) HYCOM50

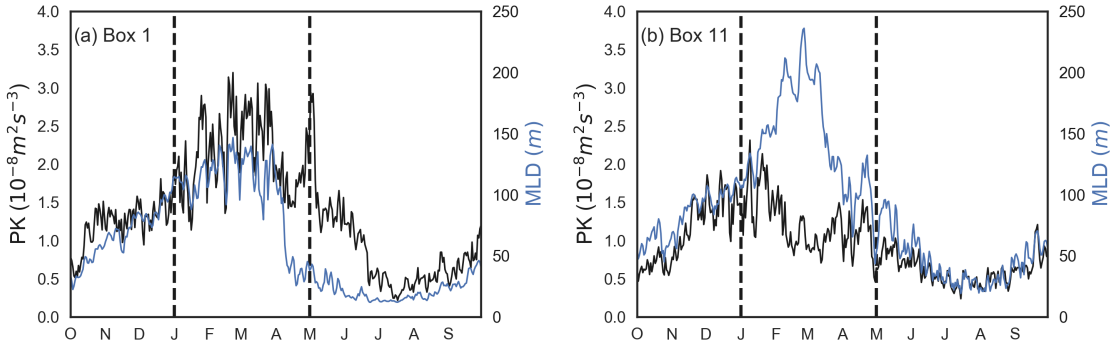

Figure 13: Time series of available potential energy, PK (blue line) and mixed layer depth, MLD (black line) for NATL60

of submesoscale energy generation by mixed layer instability. However, how the seasonality of submesoscales translates to the seasonality of SMEs is still unclear. This section aims to show that the increased population of SMEs in winter is directly linked to the advent of submesoscale turbulence in winter. Frontal structures that generate submesoscale eddies (Gula et al., 2016) exhibit high values of relative vorticity (Held et al., 1995). We intend to show the relationship between relative vorticity and submesoscale eddy statistics following a correlation of the later with mixed layer depth as shown in Sasaki et al. (2017).

In order to establish the relationship between the seasonality of submesoscale energy and eddy scale seasonality, we quantify the conversion of KE through baroclinic mixed layer instability following Boccaletti et al. (2007), Fox-Kemper et al. (2008), and Capet et al. (2008)). This conversion rate of available potential energy (APE) to eddy kinetic energy is defined as

$$PK = \frac{1}{h}\int_0^{-h} \langle w' b' \rangle_{xy} \, dz. \tag{2}$$

h, w, and b represent the mixed layer depth, vertical velocity, buoyancy gradient, respectively. The prime sign $[']$ indicates the small-scale component of the flow obtained by applying Lanczos windowing (with a cut frequency of 0.0125 and window size of 80 grid points) method to the two-dimensional fields of vertical velocity (w) and buoyancy (b).

Figure 13 presents the time series of mixed-layer depth (MLD) (blue line) and PK (black line) in box 1 and box 11 for NATL60. These two quantities are correlated with similar peaks in wintertime. This is consistent with previously published results of Boccaletti et al. (2007) and Sasaki et al. (2014) and this underscores mixed layer instability as the major driver for the emergence of submesoscale in winter.

We show similar time series for MLD (blue line), RV (red line) and daily counts

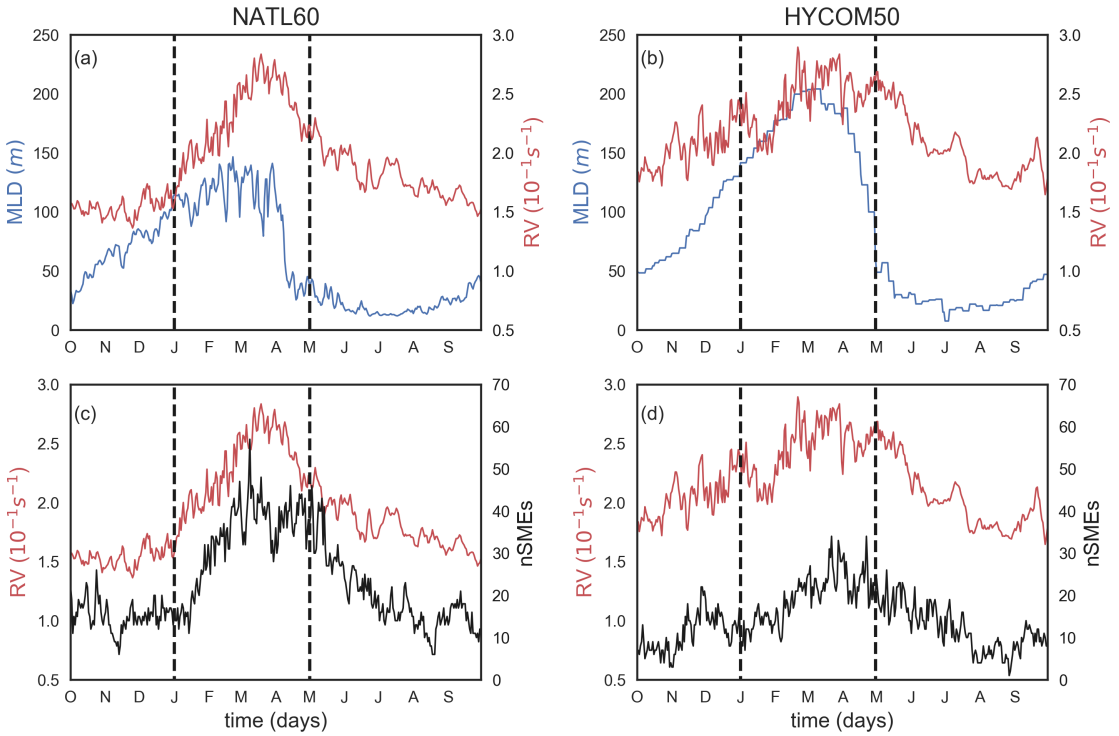

Figure 14: Time series of mixed layer depth, MLD (thin black line), root mean square of the surface relative vorticity RV (red line) and the number of submesoscale eddies (thick black line) in Box 1 for NATL60 and HYCOM50 datasets. nSMEs (daily number of L_η with a scale between 10km and 50 km)

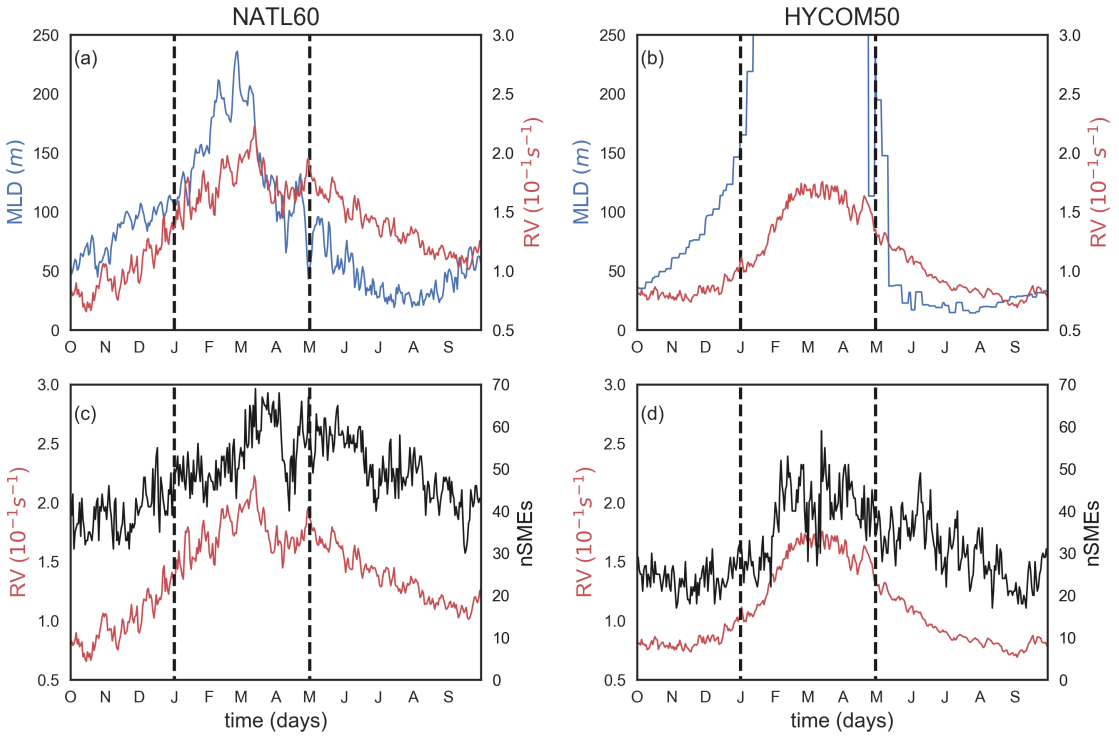

Figure 15: Time series of mixed layer depth, MLD (thin black line), root mean square of the surface relative vorticity RV (red line) and the number of submesoscale eddies (thick black line) in Box 11 for NATL60 and HYCOM50 datasets. nSMEs (daily number of L_η with a scale between 10km and 50 km)

of SMEs (thick black line) in Figure 14 and 15 for Box 1 and Box 11, respectively. Indeed, Figure 14a,b and 15a,b highlight how mixed layer instability drives the evolution of relative vorticity with a peak value in winter. An abrupt decay of MLD is observed in late winter that is not observed for RV. A similar result was recorded by Sasaki et al. (2017) and the authors attributed this difference in MLD and RV (starting in late winter) to the evolution of RV in two-dimensional turbulent flow in free decay after an abrupt decay of MLD. This implies that the dynamics immediately after wintertime is characterized by an inverse cascade of energy. This inverse cascade is evident in the subsequent decline in the number of submesoscale eddies in late winter (Figures 14c,d and 15c,d). It is, however, worth mentioning that SMEs and RV show a strong correlation with a similar peak in winter.

Figure 16 presents the vertical profile of eddy buoyancy fluxes $\langle w^{'}b^{'}\rangle$ in March and September for Box 1 and Box 11. We see seasonality in the profiles and this is associated with changes in mixed layer depth. The magnitude of $\langle w^{'}b^{'}\rangle$ in March is higher compared to September for the two simulations. A higher $\langle w^{'}b^{'}\rangle$ is responsible for feeding the growth and emergence of submesoscales eddies in winter. This growth is, however, region dependent. The winter-summer change in APE in Box 1 is about a factor of 3 higher than Box 11 for both NATL60 and HYCOM50.

6 Conclusion

The spatial and temporal variability of the typical size of oceanic eddies smaller than 100 km is investigated in this study using two submesoscale-permitting ocean model simulations of the North Atlantic; NATL60 and HYCOM50. The scale of oceanic eddies shows a strong temporal and spatial variability as reflected in the enstrophy-containing scale which is estimated from the vorticity wavenumber spectra. Our analysis reveals that the increased population of submesoscale eddies (10 km - 50 km), driven by mixed layer instability in wintertime, is responsible for the seasonality of eddy scale in the North Atlantic. The winter/summer difference in the averaged eddy scale is about a factor of two in favor of summer. The map of averaged eddy scale reveals that the spatial variability of eddy length scale is consistent with the latitudinal dependence of the first Rossby radius of deformation and that most of the eddies 30°N of the North Atlantic are nonlinear in nature with a wider nonlinearity spread in the 55°N latitudinal bands. In terms of eddy penetration, we found that at scales less than 100 km the vertical structures of energetic eddy motion (diagnosed from the spectral coherence of vorticity) vary seasonally as a function of the mixed layer depth. In fact, the depth penetration of eddies with scales < 50 km is confined to the mixed layer. This further highlights how mixed layer instability modulates fine-scale dynamics.

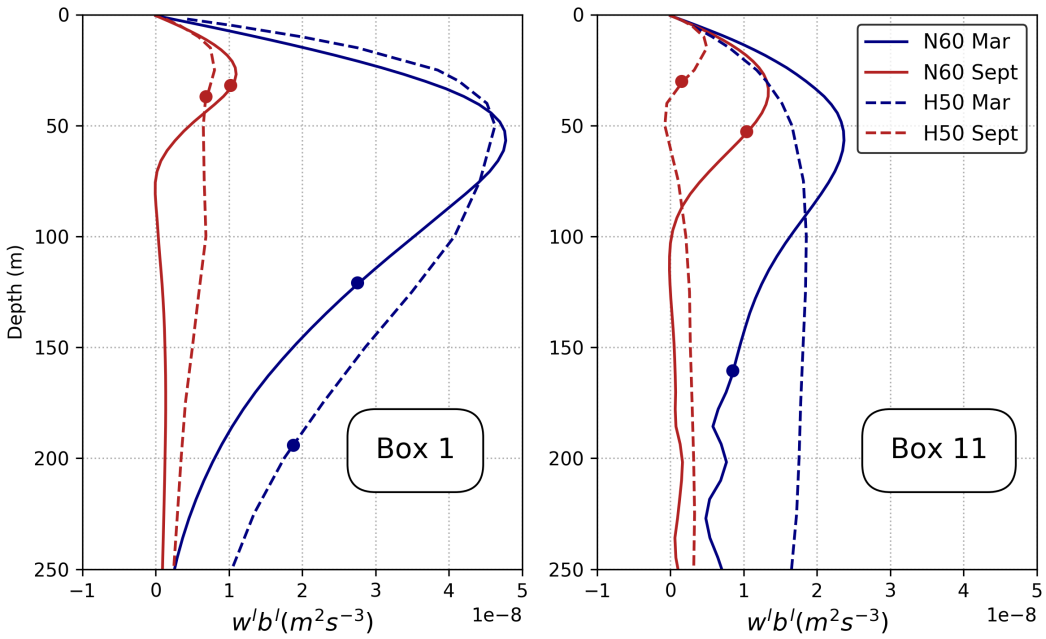

Figure 16: March (blue line) and September (red line) profile of $w'b'$ in Box 1 and Box 11 for NATL60 (thick line) and HYCOM50 (dashed line). Thick dot represent mixed layer depth.

While the focus of this study is to investigate eddy scale variability, we also examined the ability of NATL60 and HYCOM50 as a virtual observation scene for the SWOT mission. Following the analysis presented in this study and despite the model differences in terms of numerics, parameterization scheme, and vertical resolution, the statistics of eddy scale and the vertical structure of eddy motions captured by the two models are comparable. We can reasonably conclude that both NATL60 and HYCOM50 have the capability to resolve and characterize fine-scale dynamics down to 15 km scales in the North Atlantic, and that the fine-scale dynamics predicted by the models are a robust feature of this class of submesoscale permitting ocean models. This is key for the SWOT mission because information about eddy scale variability from these simulations (with respect to their horizontal resolution) is very useful for the calibration of inversion techniques for estimating two-dimensional maps of SSH from SWOT data. This knowledge of eddy scale variability will also be useful for improving eddy parameterization schemes of ocean models. However, there are concerns as to the size of the eddies identified in the models. The eddies are relatively smaller in NATL60 than in HYCOM50, and this is possibly a consequence of NATL60 short spin-up pahse (6 months) and smaller inverse energy cascade. In light of that, a longer run of NATL60 is recommended for future study to allow enough time for the simulated eddies to equilibrate.

Chapter 4

Kinetic energy transfer at fine-scale in a regime of energetic submesoscale motions.

Contents

4.1 Introduction

Much is known about the ocean kinetic energy at scales > 200km where 2D balanced motions dominate and also at scales less than 1km where unbalanced motions in 3D turbulence are at play. However, a wide gap remains in between these two spatial regimes and which is where fine-scale motion resides. 3D turbulence is characterized by a forward cascade of energy, but we do not know exactly the spatial range occupied by this forward cascade neither are we really sure of the mechanisms that flux energy downscale towards dissipation. Recent evidence suggests that submesoscale motions could provide a pathway to energy dissipation. Having said that, it is not clear at the moment if this forward cascade by submesoscales extends towards the interior of the ocean. In the previous chapter, we showed that submesoscales undergo strong seasonality that is associated with mixed-layer instability and that this seasonality affects the distribution and the average spatial scale of oceanic eddies. This is true both in the North Atlantic mid-latitudes and in the subpolar gyre. The aim of this chapter is to investigate how submesoscale and its associated seasonality affect cross-scale kinetic energy exchanges both at the surface and the interior of the ocean.

The method and the result of this chapter were prepared in the form of a manuscript and have been submitted to the Journal of Advances in Modeling Earth Systems with the title: *Diagnosing cross-scale kinetic energy exchanges from two submesoscale permitting ocean models*. `https://doi.org/10.1002/essoar.10501077.1`

4.2 Diagnosing cross-scale kinetic energy exchanges from two submesoscale permitting ocean models (Publication)

Diagnosing cross-scale kinetic energy exchanges from two submesoscale permitting ocean models.

A. O. Ajayi[1], **J. Le Sommer**[1], **E. Chassignet**[2], **JM. Molines**[1], **X. Xu**[2], **A. Albert**[1], and **W. Dewar**[2]

[1]Universite Grenoble Alpes /CNRS/IGE, Grenoble, France.
[2]Florida State University, Tallahassee, USA.

This manuscript has been submitted on the 16th of October 2019, to the Journal of Advances in Modeling Earth Systems.

Abstract

The upper-ocean at fine-scales (<100 km) contributes significantly to energy exchanges and dissipation. However, our knowledge of fine-scale motions (in terms of kinetic energy density and transfer) in the real ocean is limited due to lack of sufficient observational datasets at these scales. Kilometric resolving ocean models have been developed in anticipation for the Surface Water and Ocean Topography (SWOT) satellite mission. This mission would provide unprecedented global coverage of energetic oceanic flows down to 10 km. In this study, we investigate the distribution and exchange of energy across different scales down to 10 km based on two state-of-the-art realistic North Atlantic basin simulations with horizontal resolution of ~ 1.5 km. The results show that ageostrophic motions have direct impacts on cross-scale kinetic energy exchanges and that these exchanges undergo both regional and seasonal variability. In particular, this seasonality which is more pronounced at fine-scale is characterized by a significant amount of direct KE cascade in wintertime. In general, we found the forward cascade to be confined to the mixed layer depth while the inverse cascade extends down to about 700m in the interior.

1 Introduction

The world ocean is a turbulent fluid with a very broad range of energetic scales, ranging from large $\sim$ O(1000km) to centimeter scales. The ocean kinetic energy is mostly

concentrated in quasi-geostrophic mesoscale eddy field with scales $\sim$O(100 km) (Stammer and Böning, 1992). Due to non-linear interactions among different length scales, energy can be transferred both from large to small (forward, or direct cascade) and from small to large scale (inverse cascade). Understanding the distribution of kinetic energy and variance across scale in oceanic flows is, therefore, key to our knowledge of ocean circulation (Ferrari and Wunsch, 2009).

To estimate the variance and energy associated with eddy motions at different scales, velocity wavenumber spectral density has proven to be very efficient (Le Traon et al., 1990, 2008; Fu et al., 2010; Dufau et al., 2016; Uchida et al., 2017). However, spectral density does not indicate the direction of kinetic energy exchanges between the different scales. A better knowledge of cross-scale energy exchanges is gained by looking at the KE cascade due to nonlinearity. This important feature in turbulence study dates back to the work of Charney (1971) and Salmon (1980) on geostrophic turbulence. For a stratified rotating quasi-two-dimensional fluid motion, classical geostrophic turbulence theory predicts a direct cascade of energy if the flow is depth-dependent (baroclinic) but an inverse cascade of energy if the flow is depth-independent (barotropic). In particular, for the ocean with a surface intensified stratification, energy from higher baroclinic modes concentrates in the first mode and then undergoes a direct cascade towards the deformation scale (R_d) (Smith and Vallis, 2002). At R_d, baroclinic energy is converted to barotropic mode via barotropization. At this point, most of the energy near the deformation scale cascade towards larger scale while a small fraction undergoes direct cascade to dissipation (see Figure 1).

This prediction of geostrophic turbulence theory has been observed both in the virtual ocean and the real ocean but with a little discrepancy. Based on altimeter data, Scott and Wang (2005) showed that the (Pacific) ocean is dominated by an inverse cascade of energy at scales larger than R_d. So, if one agrees that the altimeter data is reflecting the first baroclinic mode (Smith and Vallis, 2002), then this is in contrast with geostrophic turbulence theory which predicts a forward cascade for a baroclinic flow. From this discrepancy, two questions arise. (i) is the inverse cascade seen at the surface due to the barotropic mode? or (ii) is it possible that the baroclinic modes experience an inverse cascade? Scott and Arbic (2007) using a 2-layer model simulation showed that the inverse cascade at the ocean surface is mostly baroclinic with a small contribution from the barotropic mode. More recent literature Eden (2007); Sasaki et al. (2017); Tulloch et al. (2011); Aluie et al. (2017); Brüggemann and Eden (2015); Kjellsson and Zanna (2017); Khatri et al. (2018) have also shown that inverse cascade of energy mostly dominates the surface ocean at scales larger than R_d.

Indeed we know much about the inverse-cascade-dominated-ocean-surface for scales larger than the deformation radius. What about at fine-scales where ocean struc-

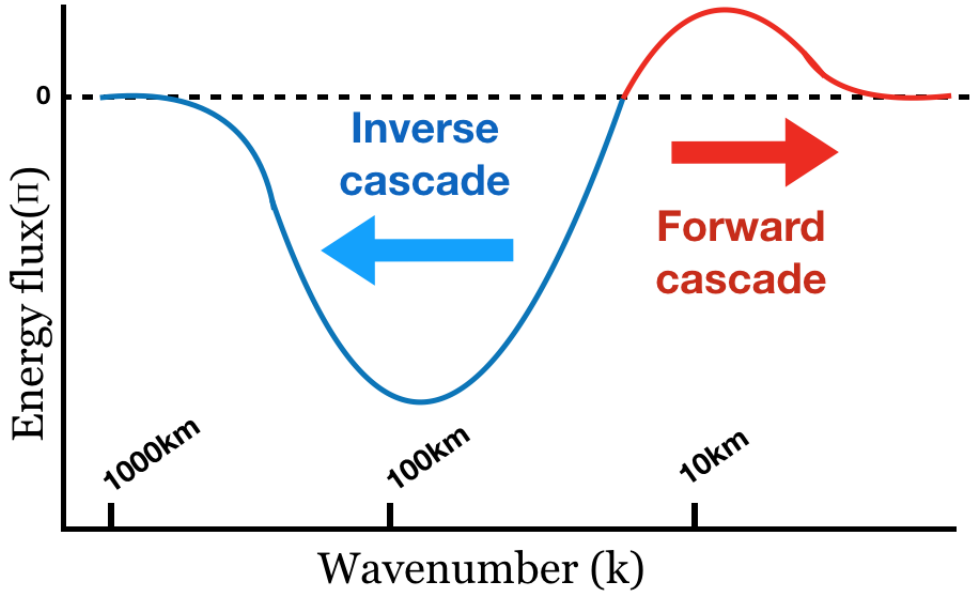

Figure 1: Schematics of kinetic energy spectral flux. Blue : inverse cascade of energy, Red : forward cascade of energy.

tures are very energetic and are highly modulated seasonally? In fact, at scales < 100 km, oceanic motion includes energetic submesoscale motions (< 50km). Results from numerical simulation and observation have shown an injection of energy in wintertime at submesocales (Sasaki et al., 2017). This energy injection is partly responsible for both meso and submesoscale seasonality (Uchida et al., 2017; Capet et al., 2008a; Sasaki et al., 2014) and has been argued to be associated with mixed layer instability (Callies et al., 2015; Qiu et al., 2014; Sasaki et al., 2014; Brannigan et al., 2015; Rocha et al., 2016). This seasonality is responsible for the shallowing of KE spectra slope from -3 in summer to -2 in winter. This is usually interpreted as a shift from a turbulence dominated by interior gradients (Charney regime) to a regime dominated by surface driven turbulence (Philips regime) (Sasaki et al., 2014). Apart from the work of Sasaki et al. (2017, 2014), we are unaware of any investigation on the implication of submesoscale seasonality on cross-scale energy exchanges at basin scale. There are also a few other open questions with regard to energy transfer at fine-scales that are worth investigating, e.g., (i) what are the range of scales that corresponds to forward and inverse cascade of energy, (ii) the depth penetration of this cascade and in particular (iii) how much energy is cascaded in the forward direction at fine scale.

Submesoscale resolving ocean models have been developed in anticipation for the Surface Water and Ocean Topography (SWOT) satellite mission (Fu et al., 2010). At a global scale, satellite altimeter remains the major source of information on the distribution of energy across scales. However, at the moment, the resolution capability of our existing ocean-observing satellite altimeter stands at roughly 70 km

(Dufau et al., 2016). This limitation undermines our ability to investigate energy exchanges at scales < 100 km. To solve this challenge, SWOT is been implemented to provide 10 times higher resolution than conventional altimeters and numerical ocean models have been designed to prepare for SWOT. These state-of-the-art numerical experiments with high resolution capability thereby provide an opportunity to study cross-scale energy exchanges down to kilometric scales while keeping in mind the aforementioned open questions.

To this end, the aim of this study is to investigate the distribution and transfer of energy across different scales by using outputs of two sub-mesoscale permitting ocean models of the North Atlantic. In particular, we focus on the seasonality and depth penetration of cross-scale KE variance and transfer with an emphasis on scales < 100 km. This paper is organized as follows, section 2 presents a short description of the two numerical simulations. In section 3, we examine the kinetic energy wavenumber spectral density and slope. The KE cascade, the seasonality and the influence of ageostrophic flow on energy cascade in the North Atlantic are discussed in section 4. Finally, in section 5 we summarize the findings and discuss the relevance of this work to the anticipated SWOT mission.

2 North Atlantic Numerical Simulations

In this study, we use numerical outputs from two submesoscale eddy-permitting simulations of the North Atlantic: a NEMO-based simulation with a horizontal resolution of 1/60° (NATL60) and a HYCOM-based (HYbrid Coordinate Ocean Model) simulation with a horizontal resolution of 1/50° (HYCOM50).

The NEMO-based NATL60 has a horizontal grid spacing ranging from 1.6 km at 26°N to 0.9 km at 65°N. The initial and open boundary conditions are based on the GLORYS2v3 ocean reanalysis with a relaxation zone at the northern boundary for sea-ice concentration and thickness. The model has 300 vertical levels with a resolution of 1 m at the top-most layers. The atmospheric forcing is based on DFS5.2 Dussin et al. (2018) and the grid and bathymetry follows Ducousso et al. (2017). In order to implicitly adapt lateral viscosity and diffusivity to flow properties, a third-order upwind advection scheme is used for both momentum and tracers in the model simulation. The model is spin-up for a period of six months, and a one-year simulation outputs from the year 2012 to 2013 are used in this study. A description of the NATL60 simulation is available from Le Sommer et al. (2019) and the outputs have been used in the recent studies by Fresnay et al. (2018) and Amores et al. (2018).

The HYCOM-based HYCOM50 extends from 28°S to 80°N and has a horizontal

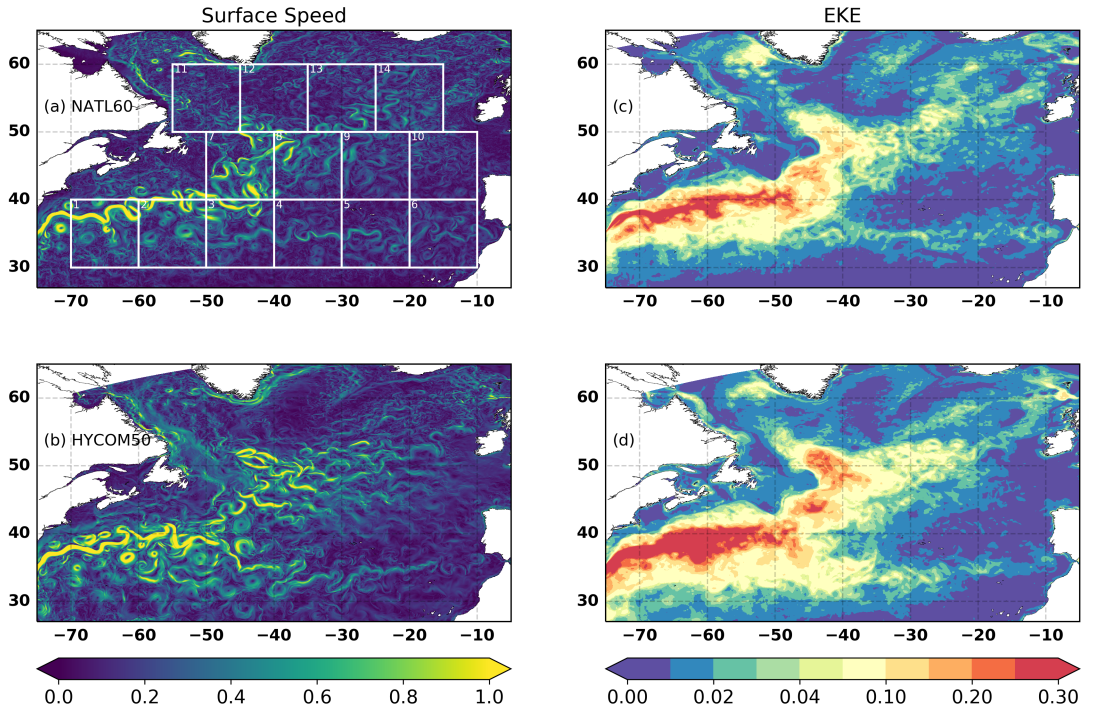

Figure 2: Left panel : snapshot of surface speed on march 1st for NATL60 and HYCOM50. Right panel : eddy kinetic energy computed from daily output of surface velocity field.

grid spacing ranging from 2.25 km at the equator, $\sim$1.5 km in the Gulf Stream region, and 1 km in the subpolar gyre. As for NATL60, the effective resolution is about 10–15 km. The vertical coordinate is hybrid and consists of 32 layers. The simulation is initialized using potential temperature and salinity from the GDEM climatology and spun up from rest for 20 years using climatological atmospheric forcing from ERA-40 (Uppala et al., 2005), with 3-hourly wind anomalies from the Fleet Numerical Meteorology and Oceanography Center 3-hourly Navy Operational Global Atmospheric Prediction System (NOGAPS) for the year 2003. The year 2003 is considered to be a neutral year over the 1993 to present timeframe in terms of long-term atmospheric patterns of the North Atlantic Oscillation. The last year of the simulation is used to perform the analysis. The horizontal viscosity operator is a combination of Laplacian and Biharmonic. The bathymetry is based on the Naval Research Laboratory (NRL) digital bathymetry database. The model configuration and a detailed evaluation of the model results in the Gulf Stream region with observations are documented in Chassignet and Xu (2017).

Both NATL60 and HYCOM50 resolve the first Rossby radius of deformation everywhere within the model domains and these simulations reproduce realistic eddy statistics with levels of kinetic energy in the range of altimetric observations (Le Sommer et al., 2019; Chassignet and Xu, 2017) (Figure 2). HYCOM50 shows a higher eddy kinetic energy (EKE) level along and around the Gulf Stream-North

Atlantic Current path. The less energetic Gulf Stream-North Atlantic Current in the NATL60 simulation may be due, in part, to its shorter spin-up period (6 months versus 19 years). A summary of the model parameters is tabulated in Table 1.

Table 1: Table of model parameters for NATL60 and HYCOM50

	NATL60	HYCOM50
Domain	26.5N - 65N	28 - 80N
Numerical Code	Nemo v.3.6	HYCOM
Horizontal grid	1/60: 0.9-1.6 km	1/50:1.1-2.2 km
Vertical coordinate	Z partial cells	Hybrid (Z & isopycnal)
Vertical grid	300 Levels : 1-50 m	32 Layers
Boundary conditions	GLORYS2v3	GDEM
Atmospheric forcing	DFS5.2	ERA-40
Horizontal Viscosity	Implicit in momentum advection	Laplacian & Biharmonic

Since the NATL60 covers a smaller domain than HYCOM50, we consider the HYCOM50 outputs for exactly the same region covered by NATL60 to have comparable results and we perform spectral analysis in sub-domains of 14 $10^\circ \times 10^\circ$ boxes across the North Atlantic. We focus specifically on quantifying kinetic energy wavenumber spectral density (Eq. 1) and flux (Eq. 2) using horizontal velocity fields. In equation (1) and equation (2),$\hat{}$refers to Fourier transform, * represents the complex conjugate, *Re* refers to the real part of a complex number and $k = \sqrt{k_x^2 + k_y^2}$. Before performing spectral analysis the 2D velocity field from each subdomain (box) is detrended in both direction and a 50% cosine taper window (turkey windowing) is applied for tapering. An FFT is applied to the tapered data and a 1D isotropic spectrum is obtained by averaging in the azimuthal direction. Our spectra method is consistent with procedures previously used in Stammer and Böning (1992); Sasaki and Klein (2012); and Chassignet and Xu (2017).

$$E(k) = \int_k^{k+\delta k} \left[\widehat{\mathbf{u}}^* \cdot \widehat{\mathbf{u}}\right](k)dk \tag{1}$$

$$\Pi(k) = \int_k^{k_s} -Re\left[\widehat{\mathbf{u}}^* \cdot \left(\widehat{\mathbf{u} \cdot \nabla_{\mathbf{H}}\mathbf{u}}\right)\right](k)dk \tag{2}$$

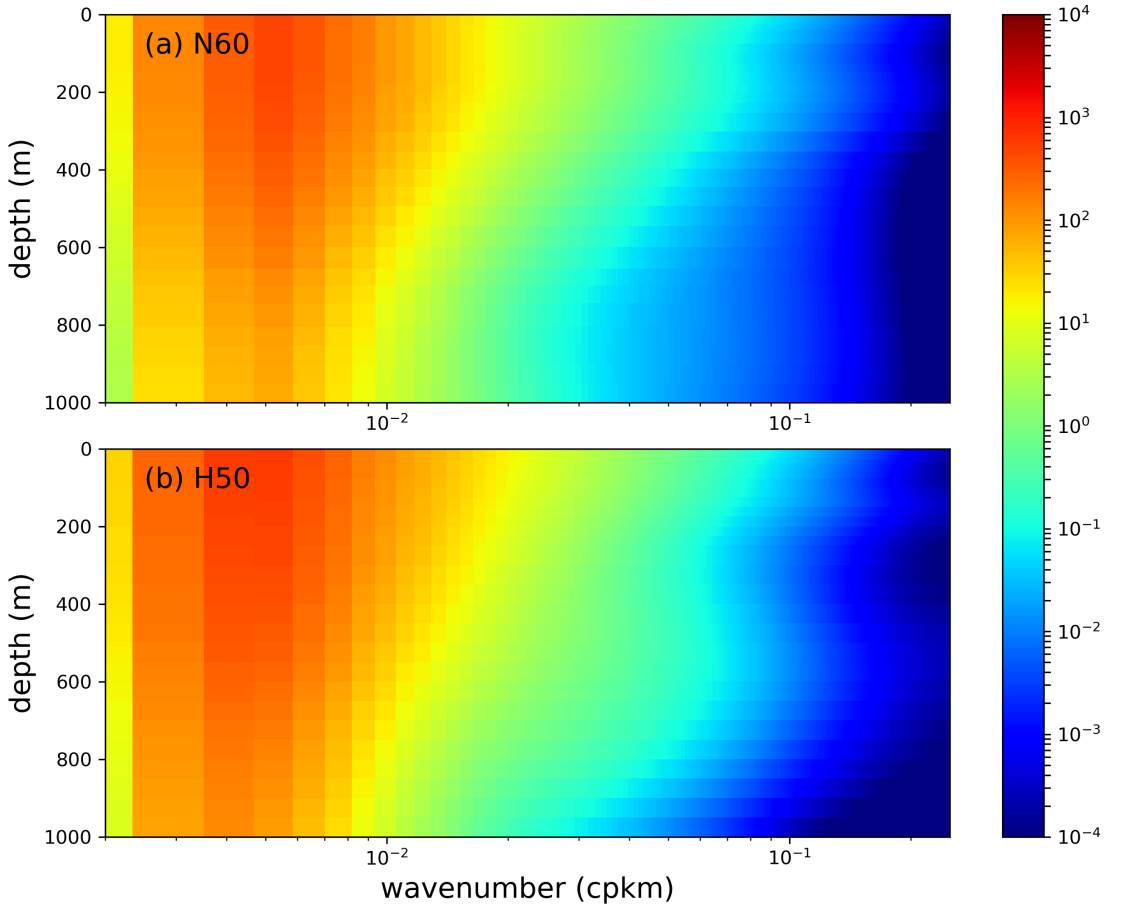

Figure 3: One year average of kinetic energy spectral density (computed from daily outputs for Box 8) as a function of depth for (a) NATL60 and (b) HYCOM50.

3 Distribution of Kinetic Energy

3.1 Spectral Density

We present in this section the analysis of the kinetic energy wavenumber spectra as a proxy to quantify the energy across different scales of motions. In Figure 3 we present the KE spectral density as a function of depth for the two simulations (Box 8). The peak of the spectral density is around the mesoscale motions (100–500 km) and, as expected, the energy associated with large scale motion are relatively higher compared to that of fine-scales. The peak is preserved with depth, but the variance at all scales decreases with depth. The decrease in the spectral variance with depth relative to the surface is more pronounced at the fine scales when compared to large scales. This indicates that the fine-scale structures (relative to the surface) are less energetic in the interior of the ocean.

The comparison between the two simulations is better illustrated in Figure 5a where

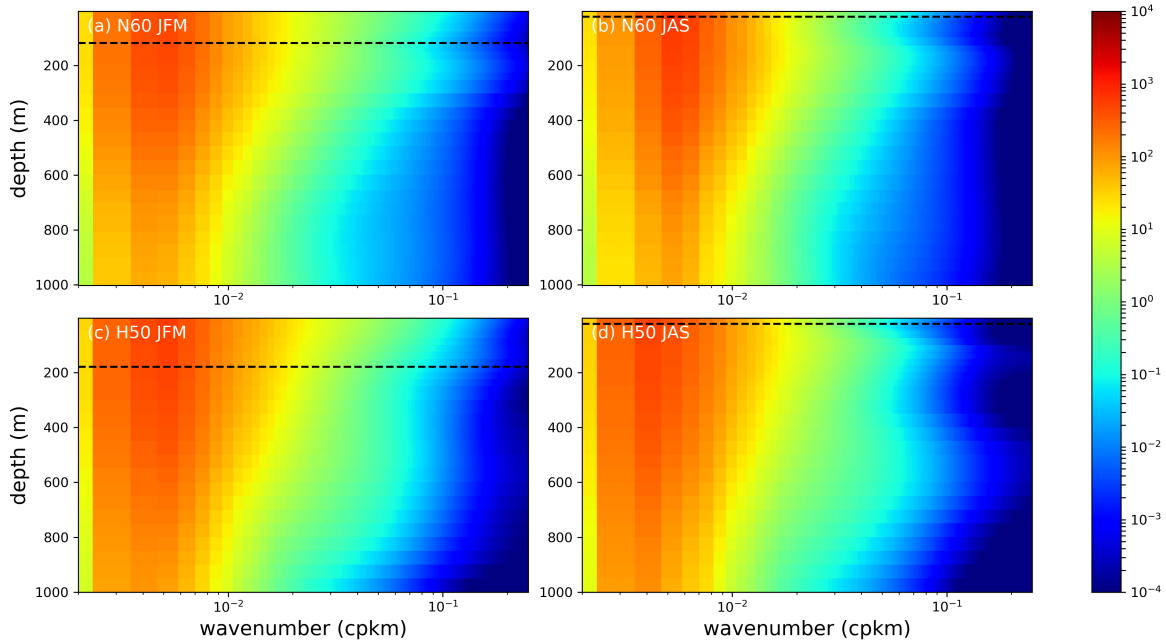

Figure 4: Winter and summer averages of kinetic energy spectral density for Box 8 computed from horizontal total velocity as a function of depth for (a) NATL60 and (b) HYCOM50.

we present the annual, winter and summer depth-averages of KE spectra density for the two simulations in the same region (Box 8). The spectral density from the two models agrees well and both are consistent with the QG prediction with a spectral shape of k^{-3}. There is a strong seasonality in the variance associated with fine-scale motions (Figure 4 and 5b). The increase in spectral density observed in wintertime at high wavenumbers underscores the energetic nature of fine-scale structures in wintertime. From the KE density plot, we also see that HYCOM50 is more energetic than NATL60 both at the surface and also in the interior.

The disparity between the energy level of the two models is not the main focus of this paper. Having said that, we propose a few reasons why the two model could differ in terms of energetics. Firstly, the eddy structures in NATL60 are not fully developed due to the short spin-up (6 months for NATL60 versus 20 years for HYCOM50). The first 2 years of the HYCOM50 simulation show a clear increase of total kinetic energy level; see Figure 2 in Chassignet and Xu (2017). Furthermore, as recently documented in Ajayi et al. (2019), the typical eddy scales are smaller in NATL60 (than in HYCOM50) and this could be a direct consequence of the shorter spin-up length. Secondly, the question did arise as to whether the coarser vertical resolution in HYCOM50 (32 hybrid vertical layers versus 300 z-levels in NATL60) could lead to a stronger inverse cascade and hence a higher energy level because of an under-resolved stratification and the depth dependence of flows. However, a comparison of the vorticity spectral coherence with respect to depth shows that the two simulations

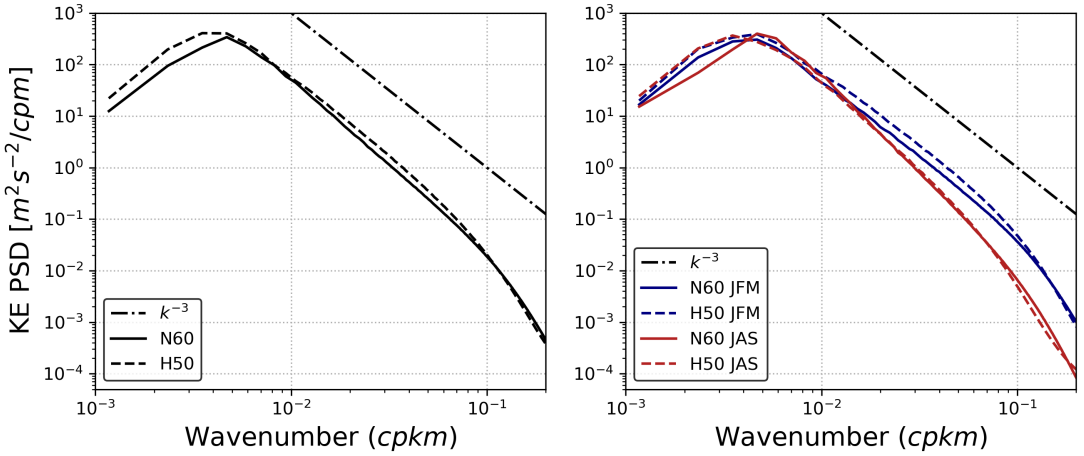

Figure 5: Kinetic energy spectra density for Box 8 (averaged over 1000m depth) computed from daily output of horizontal total velocity for NATL60 (thick line) and HYCOM50 (dash line). (a) one year mean (b) winter (blue line) and summer (red line) averages.

are essentially identical in terms of the depth penetration of energetic eddy structures (Ajayi et al., 2019). Furthermore, in section 4, a comparison of the KE spectral flux at depths for the two simulations will show that HYCOM50 upscale energy flux is not surfaced intensified and that having only 32 isopycnal vertical levels is not detrimental to the representation of the dynamics in the ocean interior. Thirdly, the choice of sub-grid parameterization is different between the two simulations and could possibly have a strong effect on how energy is dissipated between them.

3.2 Spectral Slope

Horizontal wavenumber spectral density generally exhibits power-law behavior, where the exponent is interpreted in terms of the dynamical processes governing the eddy energy transfer. Existing theoretical frameworks predict (for horizontal velocity) a spectral slope of -3 and -5/3 for Quasigeostrophic (QG) and surface quasi-geostrophic (SQG) turbulence respectively. A slope of -2 is also well known for a front dominated flow (Fu and Ferrari, 2008). Over the years, many research works have tried to establish the accuracy of these predictions by using outputs of realistic ocean models (Sasaki and Klein, 2012; Chassignet and Xu, 2017; Uchida et al., 2017) and also recently within context of the real ocean by using altimeter dataset (Le Traon et al., 1990; Dufau et al., 2016). Their results have argued for the non-existence of a universal wavenumber spectrum (Le Traon et al., 2008) following observed regional variability.

A quick way to estimate the wavenumber spectral power law is to compute the 1D wavenumber spectra then estimate a slope from this spectra by fitting a line to the

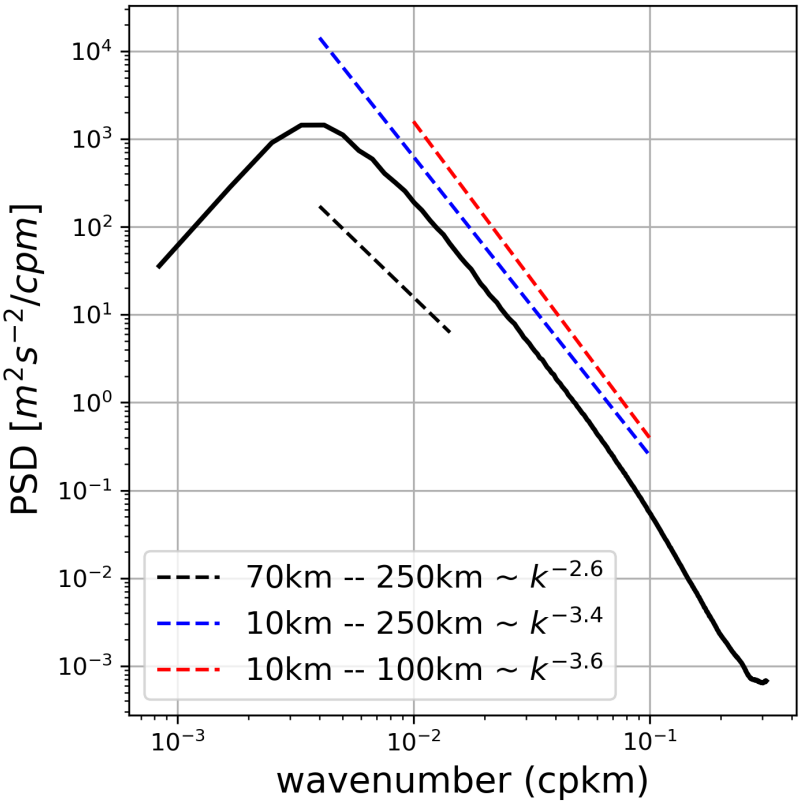

Figure 6: Average KE wavenumber spectral and slope for box 1 in the month of March for three different selected wavenumber range. The wavelengths range are represented by dashed lines with the color red, blue and black for 10-100km, 10-250km and 70 – 250km respectively.

spectral density curve within a selected wavenumber range. This method is fast and easy to implement and provides a way to investigate regional variability of ocean energetics both at the basin and global scale. For studies focused on mesoscale energetics using satellite datasets and model outputs, this wavenumber range is mostly within the error limits of the altimeter ($\sim$ 70 km) with an upper bound of 250–300 km. One drawback of this approach is that it does not account for the changes in the scale of average energetic eddy structures with latitude. Scales of motions that are mesoscales in the polar regions are classified as sub-mesoscales in the tropics.

A number of recent studies have tried to propose different approaches to estimate wavenumber spectral power law as a way to correctly characterize the spectral signature. Vergara et al. (2019) estimated spectra slope for mesoscale motions by computing the slope between the peak of the spectra and the minimum of the Rossby radius and the Rhines scale following Eden (2007). A similar approach was presented in Sasaki and Klein (2012), where the authors estimated spectral slope between a fixed wavelength of 30 km (at the lower bound) and the scale that corresponds to the peak of the KE wavenumber spectra.

In order to show how sensitive the estimated slopes are to the selected wavelength range, we present in Figure 6 the average KE wavenumber spectra and slope for box 1 in the month of March for three different selected wavenumber ranges. The wavelengths are represented by dashed lines with the color red, blue and black for 10–100 km, 10–250 km and 70–250 km respectively. The estimated slopes for these three different wavelength range have different values, therefore raising the question as to which slope is most representative of the dynamics of this region. We repeat this analysis for all the boxes and present the map in Figure 7. The mismatch is particularly pronounced at the sub-polar region, where the scales of the eddy structures are smaller. The 70–250 km wavelength range is a typical wavelength for estimating spectral slope for satellite datasets because 70 km roughly corresponds to the wavelength where the satellite data becomes noisy. The spectral slope in this range is fairly consistent with the already published work of Dufau et al. (2016) and Chassignet and Xu (2017).

To avoid the sensitivity of the estimated spectral slope to an a-priori selected wavelength range, we introduce an approach that takes into account the dynamics of the regions and the resolving capability of the model by estimating the spectral slope (Figure 8) between the energy-containing scale (Kjellsson and Zanna, 2017) and the effective resolution of the model (Soufflet et al., 2016). The energy-containing scale (which represents the scale of the most energetic eddy structure) is estimated from the kinetic energy wavenumber spectra using equation (3) while the effective resolution (a function of the model grid-size) is taken as 5 $\times$ the model grid size and this is roughly equally to 10 km for both models. This approach takes into account

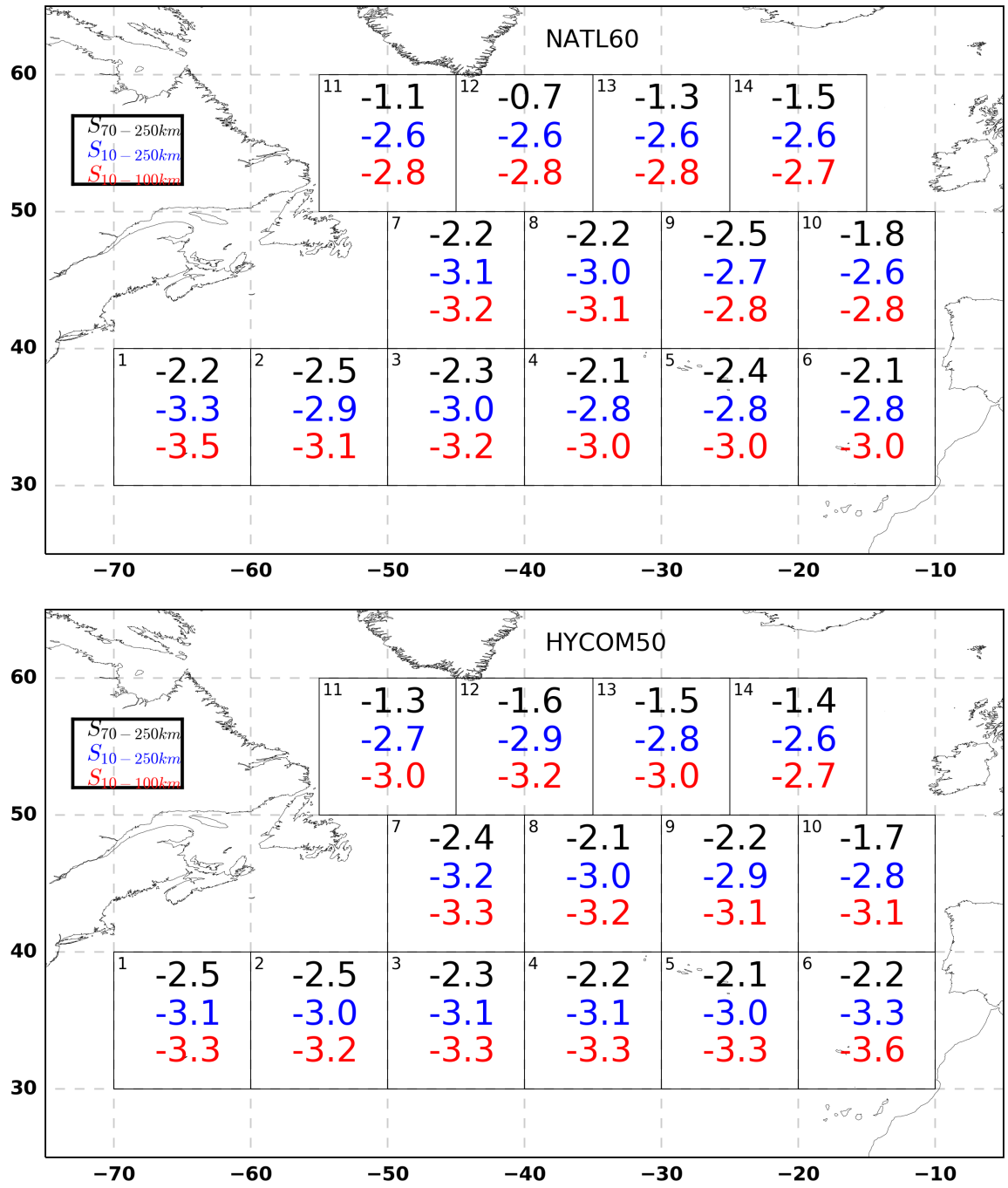

Figure 7: Map of spectral slope estimated from three different wavelength range. Colour red, blue and black represent 10 - 100km , 10 - 250km and 70 - 250km respectively

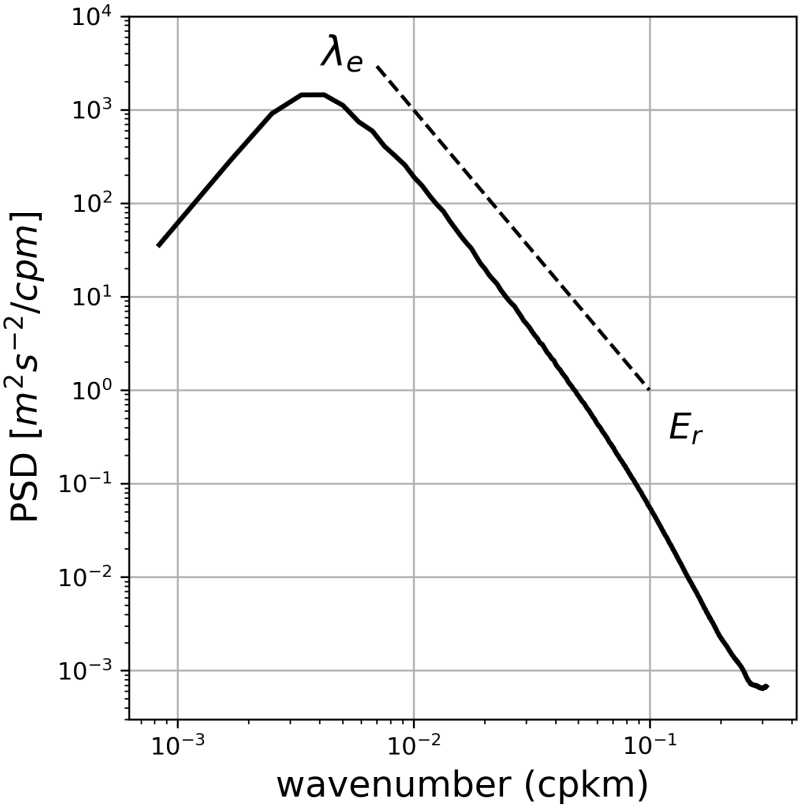

Figure 8: A schematic to illustrate the proposed dynamical approach to estimate spectral slope. λ_e is the energy-containing scale (which represents the scale of the most energetic eddy structure) and it is estimated from the kinetic energy wavenumber spectra using equation (3) while E_r is the effective resolution (a function of the model grid-size) and is taken as 5 $\times$ the model grid size. E_r is roughly equally to 10 km for both NATL60 and HYCOM50.

the scale of the energetic eddy structures within the flow region and also takes into account the geographical variability of this scale, and therefore provides a way to infer dynamical properties of oceanic motions in different regions.

$$\lambda_e = \frac{\int\int E(k_x, k_y) dk_x dk_y}{\int\int \sqrt{k_x^2 + k_y^2} E(k_x, k_y) dk_x dk_y} \tag{3}$$

We apply this technique to the output of both simulations and we present the estimated spectral slope and the energy-containing scale (integral scale) for all the boxes in the North Atlantic (Figure 9). The estimated integral scale from the wavenumber spectra represents the averaged scale of energetic motions in the selected region. On one hand, this scale varies regional and fairly follows the variability of the Rossby radius of deformation with latitude, with high values in the south and relatively low values in the north. On the other, the estimated slope across the basin is almost uniform and follows the prediction of QG with a slope value $\sim k^{-3}$. This consistency with the QG prediction is observed in both model outputs and also holds in the well known high energetic Gulf stream (box 1) and the low energetic OSMOSIS (box 10) regions. This result suggests that the North Atlantic Ocean is well described by QG dynamics.

4 Kinetic Energy Cascade

In this section, we present and discuss the exchange of energy due to non-linearity across different scales of motion. This exchange is estimated from the horizontal velocity fields using equation (2). A positive flux represents a direct cascade of energy while a negative value represents an inverse cascade of energy. The novelty of the estimated spectral flux presented in this study is partly based on the ability of the models to reasonably resolve the cross-scale energy exchanges at scales <100 km.

We show in Figure 10, the result of the KE spectra flux computed using one year daily outputs of surface velocity fields. For simplicity, we show plots for box 3, 8 and 11 representing latitudes of 35N, 45N, and 55N respectively. In all the boxes and in both model outputs, the spectral flux is dominated by an inverse cascade of energy at large scales (between 25-50km and 500km) and a forward cascade of energy below 25-50 km. Depending on the region, part of the submesoscale range of 0 to 50km (as defined by Sasaki et al. (2017)) falls to the left of the zero-crossing (where the flux changes sign). This implies that a significant part of submesoscales motions are involved in fluxing energy to large scales via an inverse cascade of energy, and this, in a way indicates how submesoscales flow impact meso and large scales circulations via energy exchanges.

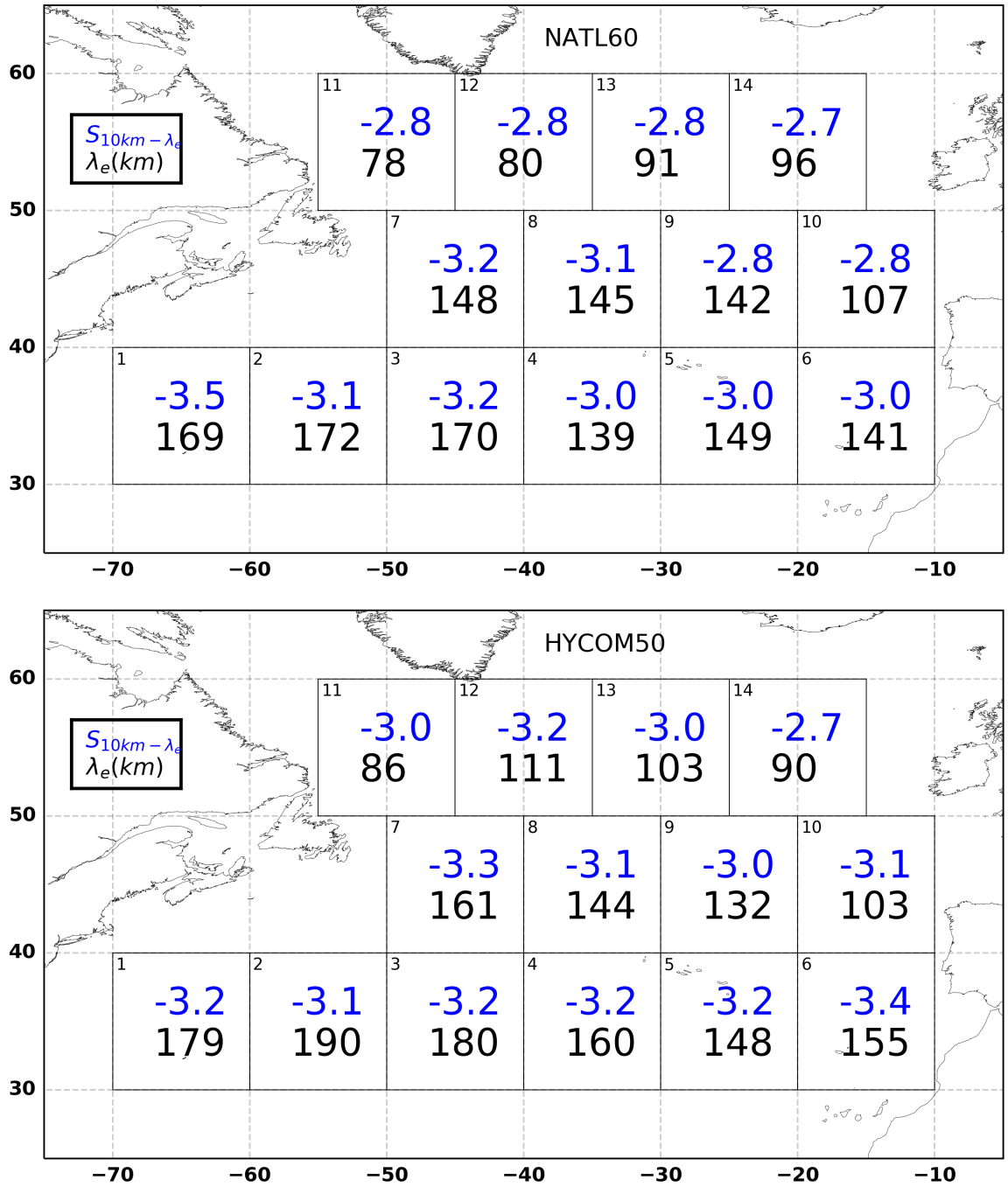

Figure 9: Blue colour : spectral slope estimated between the model effective resolution (E_f) and the integral scale (λ_e). Black colour : energy containing scale estimated from the kinetic energy wavenumber spectral density

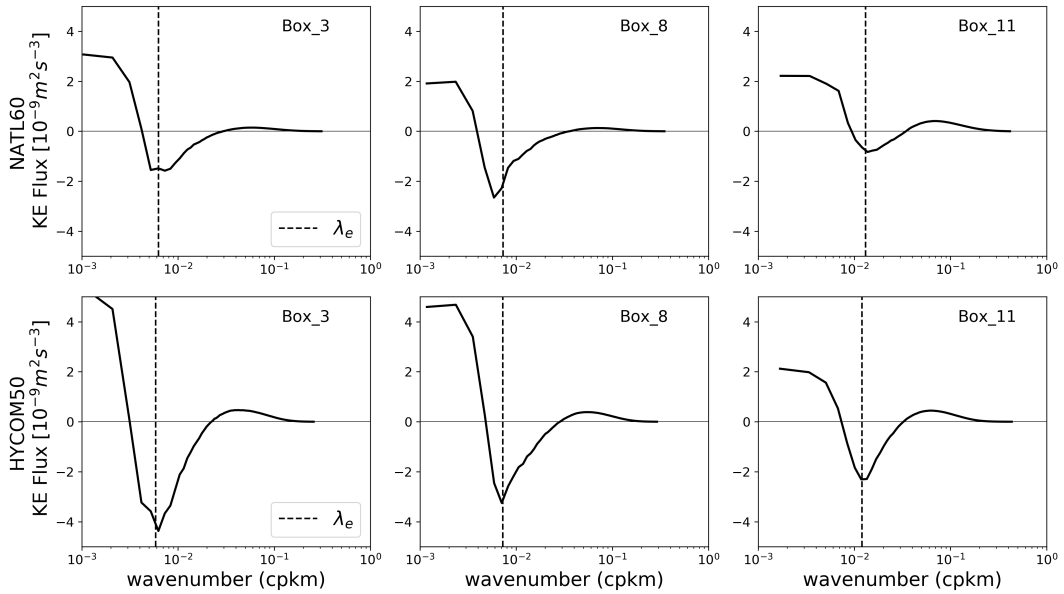

Figure 10: One year average of kinetic energy spectral flux computed from the daily output of horizontal total velocities. NATL60 (upper panel) and HYCOM50 (lower panel)

The scale at which the inverse cascade is most intense coincides with the energy-containing scale (dashed line in Figure 10) estimated from the kinetic energy spectrum. This signifies that the strength of the inverse cascade is maximum at the scale of the most energetic eddies. Just like the energy-containing scale, the scale of the most intense inverse cascade also varies with latitude with relatively smaller values in the sub-polar regions.

Figure 11 presents the KE spectral flux for Box 8 as a function depth. The overall shape of the flux is preserved and the scale at which the inverse cascade is maximum is also consistent with depth. However, the strength of inverse cascade decreases with depth and the direct cascade at high wavenumbers is confined mostly to the surface. We saw in section 1, that fine-scale structures are less energetic at depth, a consequence of that is the absence of a direct cascade of energy (at high wavenumber) at depth. The depth averaged flux for the two simulations is presented in Figure 14a.

In section 3.1, the question was raised as to whether HYCOM50's higher KE when compared to NATL60 is a consequence of HYCOM50's coarser vertical resolution which could lead to a surface intensified inverse cascade and hence more energetic surface eddies. However, in Figure 11, we can see that both at the surface and at all depth levels, the estimated inverse and direct cascade is stronger in HYCOM50 than in NATL60. This clearly indicates that HYCOM50 upscale energy flux is not surfaced intensified and we can conclude that the disparity between the two model in terms of energy levels is most likely due to differences in the length of the spin-up and

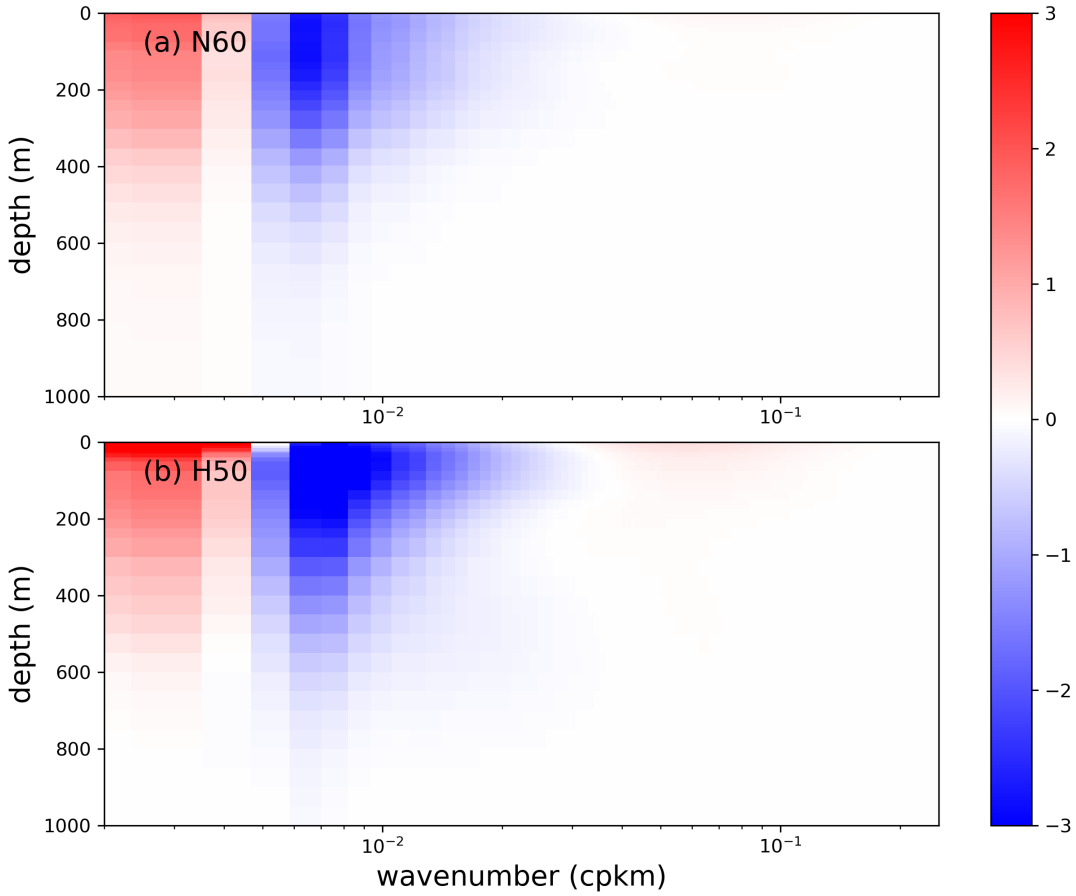

Figure 11: One year average of kinetic energy spectral flux for Box 8 computed from horizontal total velocity as a function of depth for (a) NATL60 and (b) HYCOM50. The dashed line (λ_e) is the energy containing scale estimated for the kinetic energy wavenumber spectra.

that having only 32 isopycnal vertical levels is not detrimental to the representation of the dynamics in the ocean interior.

4.1 Seasonality of energy cascade

In this section, we present the seasonality of the kinetic energy spectral flux by comparing winter (JFM) and summer (JAS) averages. Figure 12 shows the winter cascade in blue and the summer cascade in red. There are two notable differences between the seasons. First, there is a shift in the zero crossings to higher wavenumbers in winter. As previously highlighted in the preceding section, a zero-crossing at the very high wavenumbers partly indicates how much of submesoscales motions are involved in feeding large scales motions via an inverse cascade of energy. So, a shift to higher wavenumbers in wintertime signifies that smaller-scale structures are involved in fluxing energy to larger scales. Second, there is a stronger forward cascade within submesoscale wavenumber range towards dissipation in winter. Recent studies have shown that submesoscales motions are more energetic in wintertime (Sasaki et al., 2017; Rocha et al., 2016; Brannigan et al., 2015; Capet et al., 2008b) and their emergence is forced by mechanisms such as frontogenesis, wind-induced frontal instabilities, mixed layer instability among many others (Thomas, 2008; McWilliams, 2016). A possible explanation for this seasonality is that energetic submesoscale motions inject energy at small scales and part of this energy feeds larger scale motion via inverse cascade. This seasonality highlights how submesoscales motions modulate the redistribution of energy between scales of motions. Hence, the need for climate (ocean) models with submesoscale resolving capability. The seasonal differences that we see at the surface extend to the interior as well (Figure 13). The forward cascade at high wavenumbers in winter is confined within the mixed-layer depth and this corroborates what we expect, because we know that submesoscales emerging from mixed layer instability are confined to the mixed layer depth. The mean over all the depth levels is presented in Figure 14b.

It is noteworthy that the integral scale and scale of the maximum inverse cascade also undergo seasonality. There is a shift in the scale to high wavenumber from winter to summer. This can be interpreted as a reduction in the averaged size of energetic eddies structures in winter and this is consistent with the findings of Ajayi et al. (2019).

4.2 Impact of ageostrophic flows on KE flux

We have discussed so far the KE spectral flux computed using the daily output of total horizontal velocities. As mentioned earlier, NATL60 and HYCOM50 are

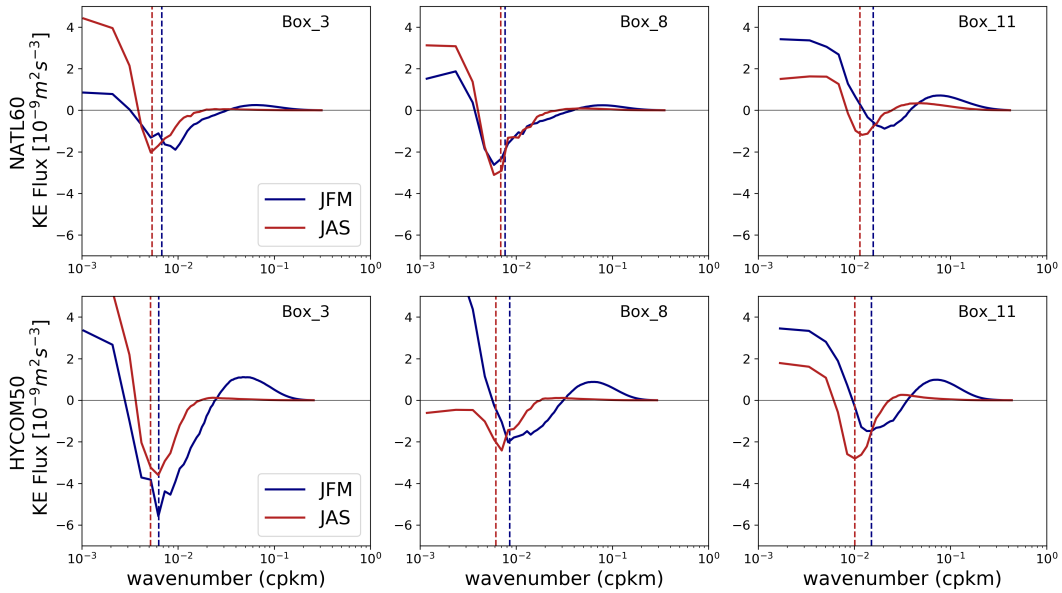

Figure 12: Winter (blue line) and summer (red line) average of kinetic energy spectral flux computed from daily output of horizontal total velocities. Dash lines represents the energy containing scale. NATL60 (upper panel) and HYCOM50 (lower panel)

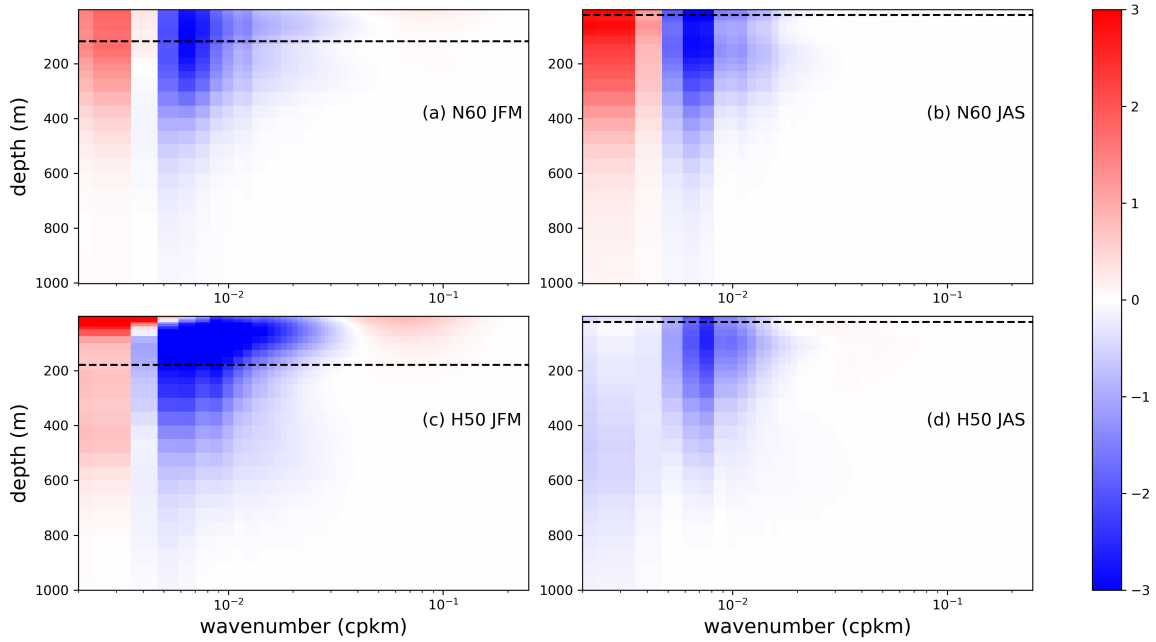

Figure 13: Winter and summer averages of kinetic energy spectral flux for Box 8 computed from horizontal total velocity as a function of depth for (a) NATL60 and (b) HYCOM50. Black dash line represents the average mixed layer depth.

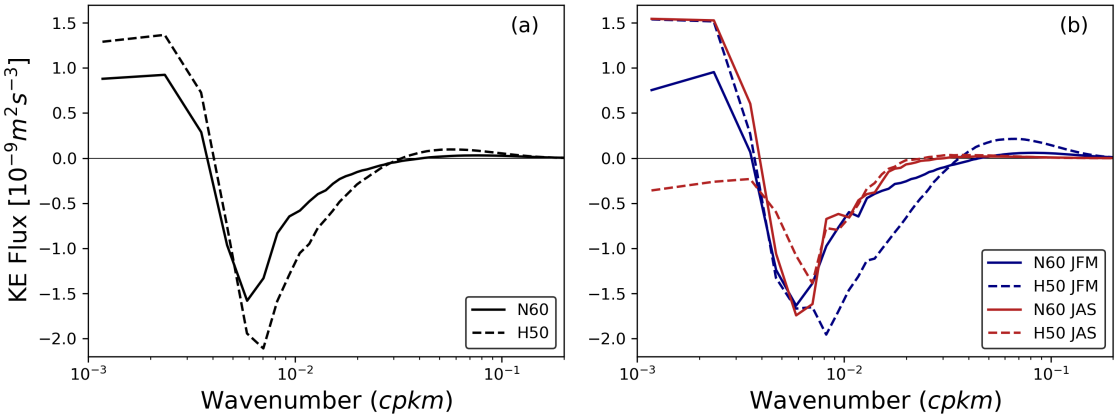

Figure 14: Kinetic energy spectra flux (averaged over 1000m depth) for Box 8 computed from daily output of horizontal total velocity for NATL60 (thick line) and HYCOM50 (dash line). (a) one year mean (b) winter (blue line) and summer (red line) averages.

submesoscale permitting model simulations that have been created to simulate the scales of motions that we expect SWOT to see from space. SWOT like every other satellite mission will provide the measurement of sea surface heights from which velocities (based on geostrophic approximations) are inferred. The world ocean is predominantly dominated by geostrophically balanced motions at meso and large scale, and the inferred geostrophic velocities at this scale mostly reflect the absolute velocity of these large scales motions. However, geostrophy is less accurate for fine-scale motions and this questions our ability to trust satellite altimeter to resolve effectively the energetics of fine-scale motions in terms of energy redistribution within the submesoscales range (<50 km). SWOT will provide information down to 15km and we are curious to see if the geostrophically inferred surface velocity would capture the true energetics at scales less than 50 km where geostrophy is likely to fail.

In Figure 15, we present the spectral flux from total velocity and geostrophic velocity for three regions (same as for the previous sections). The strength of the energy cascade differs between the flux computed from the total velocity and that of the geostrophic velocity. This difference is consistent in all the three boxes and in the two models. In particular, at the very high wavenumbers, the strength of the forward cascade is underestimated in the flux computed from the geostrophic velocity. A possible reason for this mismatch at smaller scales could be explained by the findings of Brüggemann and Eden (2015) that showed that ageostrophic flows at fine scales are a good catalyst for energy cascade towards dissipation. Despite the differences in terms of flux magnitude, the overall shape of the flux is consistent for the two forms of spectral flux. In fact, the scale of the maximum inverse cascade is the same irrespective of the type of velocity fields.

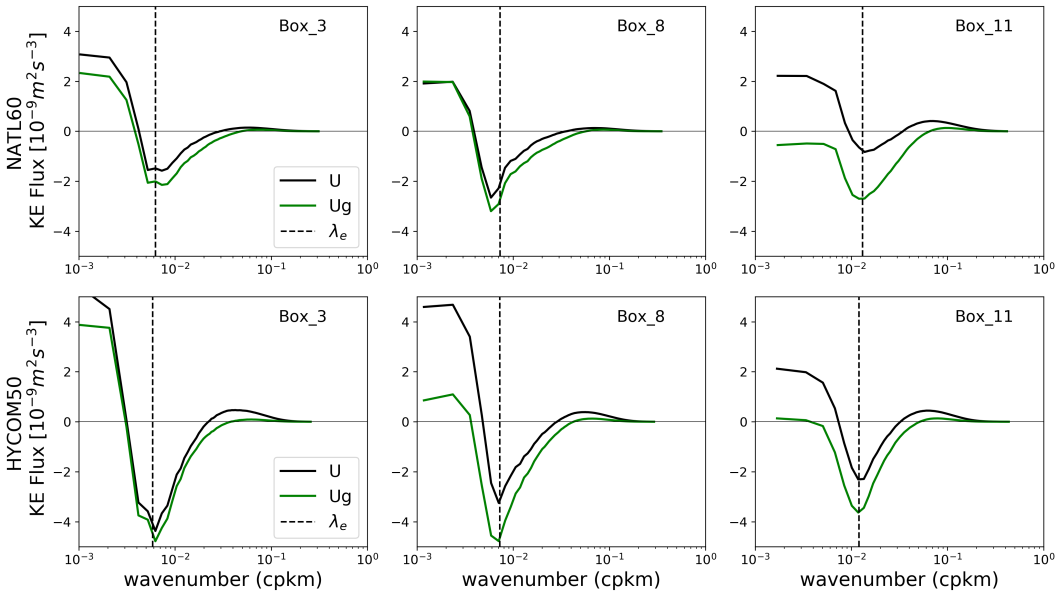

Figure 15: Kinetic energy spectral flux computed from total velocity (black line) versus spectral flux computed from geostrophic velocity (green line). NATL60 (upper panel) and HYCOM50 (lower panel)

5 Discussion and Summary

Kinetic energy wavenumber spectra density, slope, and flux are estimated in this study. The analysis presented has shown that the North Atlantic ocean follows the framework of quasi-geostrophy dynamic with a KE spectral shape of $\sim k^{-3}$ almost everywhere. Owing to the ability of our kilometric ocean models (NATL60 and HYCOM50) to reasonably resolve fine-scale structures down to 10km, kinetic energy spectral flux computed from daily outputs of horizontal total velocities revealed an overall net inverse cascade of energy with a significant direct cascade of energy at high wavenumbers. The cascade as a function of depth reveal that the forward cascade at high wavenumber is confined to the mixed layer depth while the inverse cascade dominates the water column down to 700m. We showed that the maximum inverse cascade occurs at a scale that coincides with the energy-containing scale estimated from the kinetic energy wavenumber spectra.

The results presented in this study are based on the analysis of two kilometric simulations outputs with similar horizontal grid space but different numerics, sub-grid parametrization and vertical resolution. In particular, NATL60 has 300 z levels while HYCOM50 has 32 hybrid layers. Despite these differences, the two simulations agree well on the overall dynamics of the North Atlantic. Having said that, HYCOM50 show stronger energy level compared to NATL60 both at the surface and in the interior. We found the estimated cascade in HYCOM50 to be of higher magnitude compared to NATL60 for both direct and inverse cascade. The difference

in energetics between the two models is possibly due to the difference in the length of the spin-up or the subgrid scale parameterization choices. Initially, we thought that HYCOM50 having just 32 hybrid layers in the vertical could lead to a more surface intensified energy cascade in HYCOM50 than in NATL60. But this is not the case, because across all scales and at depth, HYCOM50 seems to show stronger energetics compared to NATL60.

NATL60 and HYCOM50 are designed particularly to serve as an observational dataset for the much-anticipated SWOT mission. So what is the implication of our results for the upcoming fine-scale resolving satellite mission SWOT? From SWOT we will able get surface geostrophic velocity as usual hence we can compute cross-scale energy transfer. Our results show that not accounting for ageostrophic fine-scale motions underestimates the forward cascade of energy.

Chapter 5

Kinetic energy transfer at fine-scale in a regime of externally forced internal tides.

Contents

5.1 Introduction

Submesoscale balanced motions and unbalanced internal gravity waves are the two major classes of motions that dominates oceanic fine-scale motions. In the previous chapter, we show that kinetic energy flux at scale < 50km undergo forward cascade of energy. This forward flux is particularly strong in wintertime when submesoscale turbulence is active, suggesting that submesoscale motions can provide a route to kinetic energy dissipation. The result of the kinetic energy cascade presented in chapter 4 is based on daily averages of horizontal velocity fields. Daily averaging the model outputs suppresses the ageostrophic and super-inertial motions therefore not accounting for the effect of higher frequency motions in the estimate of the spectral flux. This statement is made obvious in Fig. 5.1 where we compare the kinetic energy spectral flux estimated form daily averaged and hourly snapshots of velocities. This plot highlights that using daily averages underestimate the magnitude of the kinetic energy forward cascade at high wavenumbers in wintertime. However, this does not change the results presented in Chapter 4 because spectral flux estimated from daily averaged velocity fields permits to isolate the impact of submesoscale motions on kinetic energy exchanges, which was the aim of that chapter. Following this results and other literature on the role of unbalanced high-frequency motions on the direct cascade of energy to dissipative scale, we investigate in this study, the role of high-frequency waves motions (in particular externally forced internal tides) on cross-scale kinetic energy exchanges.

The results of this chapter are been prepared in form of a manuscript to be submitted to the Journal of Geophysical Research Ocean with the title: *On the modulation of kinetic energy transfer by externally forced internal tides.*

5.2 On the modulation of kinetic energy transfer by externally forced internal tides (Publication)

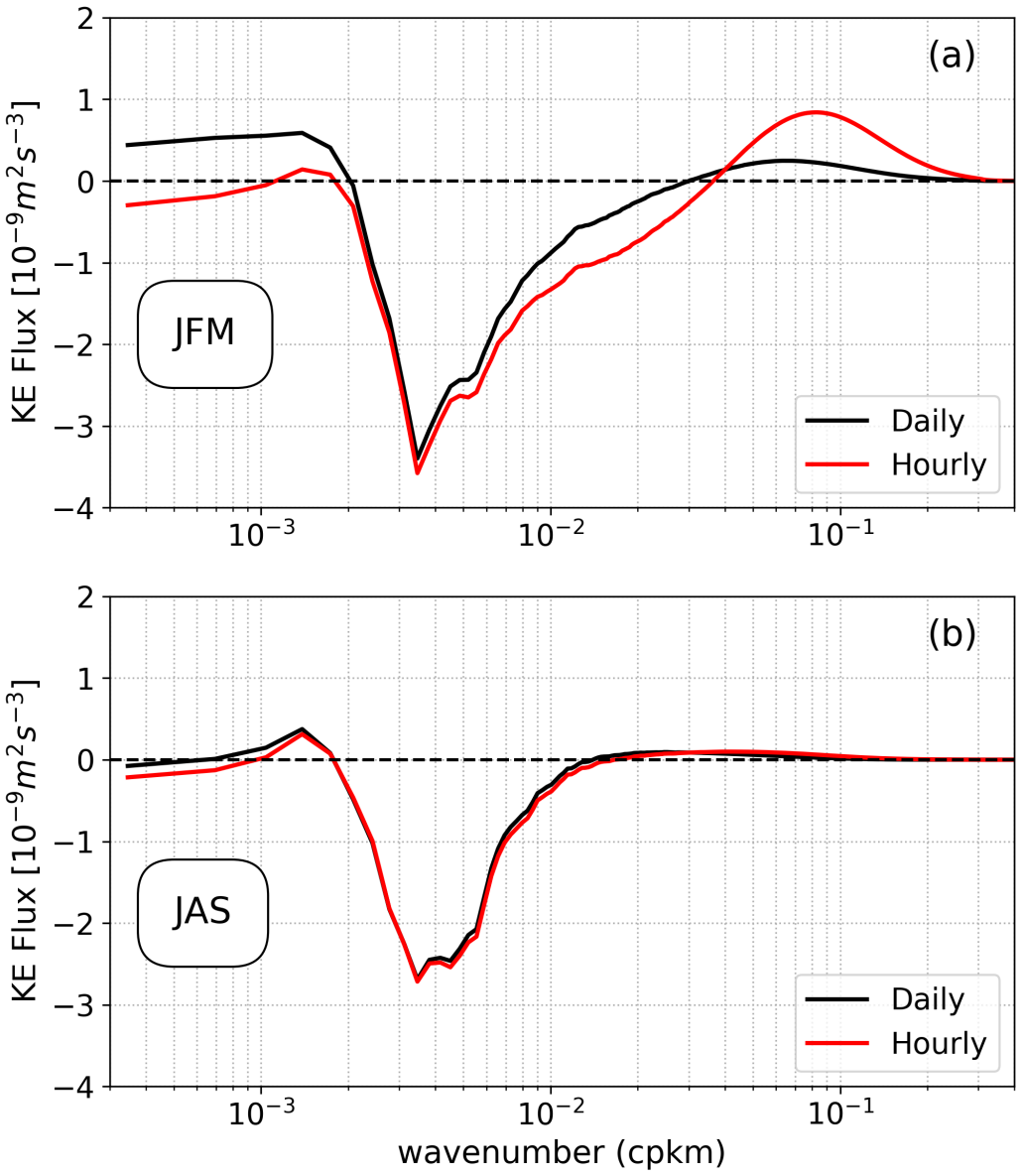

Figure 5.1: Kinetic energy spectral flux computed from daily averages and hourly snapshot of horizontal velocity outputs of NATL60 in box at the middle of North Atlantic Gyre 50°W to 20°W,30°N to 50°N. (a) JFM : Janaury, February and March (b) JAS : July, August and September

On the modulation of kinetic energy transfer by externally forced internal tides

A. O. Ajayi[1], **J. Le Sommer**[1], **L. Brodeau**[1], **B. Arbic**[2], **G. Serazin**[4], **A. Albert**[1], and **P. Klien**[3]

[1]Universite Grenoble Alpes /CNRS/IGE, Grenoble, France.
[2]University of Michigan, USA.
[3]Lops Ifremer/CNRS, Plouzane, France.
[4]Climate Change Research Center, UNSW, Australia.

In preparation for Journal of Geophysical Research : Ocean

Abstract

The question of how kinetic energy (KE) is dissipated in the ocean remains a key question in physical oceanography. Recent literature suggests that quasi-balanced submesoscale motions and internal gravity waves (IGWs) can play an active role in fluxing kinetic energy towards dissipative scales. The process and mechanisms by which these classes of motions may provide a route to dissipation remain as open questions. In this study, we investigate the impact of internal tides generated by tidal motions on cross-scale kinetic energy exchanges at mid-latitude. Our analysis is based on the output of two NEMO based sub-mesoscale permitting ocean model simulations of the North Atlantic ocean (with/without tidal forcing). Our results show that resolving both submesoscales and IGWs yields a strong forward cascade toward dissipative scales. But we find that different mechanisms are controlling this forward cascade depending on the season. In wintertime, energetic submesoscales are the key driver for the forward cascade of KE while in summertime IGWs are responsible for the forward cascade. We found that, in both seasons, the forward cascade at high wavenumbers extends vertically over a significant fraction of the upper ocean.

1 Introduction

The kinetic energy of ocean circulation is mostly concentrated in motions close to geostrophic balance, with frequencies smaller than the Coriolis frequency (f) and spatial scales larger than the first Rossby deformation radius (R_d). These balanced motions (BMs) are largely energized through baroclinic instability which extracts energy from large scale stratification. Balanced motions include large-scale motions (>300 km), mesoscale motions (50-300) and submesoscale balanced motions (<50km) McWilliams (2016). Balanced motions are characterized by an inverse cascade of energy (Scott and Wang, 2005; Scott and Arbic, 2007; Eden, 2007; Aluie et al., 2017), so they do not provide a route to dissipation by themselves. Therefore, energy has to be transferred from balanced motions to high-frequency unbalanced motion for dissipation to occur.

A particular class of unbalanced motions are fast propagating internal gravity waves (IGWs) with frequencies equal to or larger than f and spatial scale ranging from O(10m) to O(100km). IGWs include wind-induced near-inertial waves with a frequency near the Coriolis frequency and internal tides (generated by large scale barotropic tidal flow over topographic features) with diurnal and semidiurnal frequencies. Near-inertial waves are stronger in winter than in summer because they are driven by surface winds (D'Asaro, 1985) while internal tides are likely to be stronger in summer time.

In concise form, to equilibrate the well known inverse cascade of energy, the ocean requires ageostrophic processes to extract energy from balanced motions. Mechanisms that might effect a forward transfer of energy from balanced motions down to dissipate scale includes but are not limited to (i) bottom boundary-layer turbulence (Wunsch and Ferrari, 2004), (ii) generation of lee waves by mesoscale eddies interacting with topography (Nikurashin and Ferrari, 2010; Nikurashin et al., 2013), (iii) generation of internal waves by upper-ocean frontal instabilities (Danioux et al., 2012; Shakespeare and Taylor, 2014) and (iv) direct cascade of energy by energetic submesoscales motions (Capet et al., 2008b,a; Ferrari and Wunsch, 2009; McWilliams, 2016). In summary, at fine scale, there two classes of motions that can provide efficient transfer of energy to dissipative scale; submesoscale motions and internal gravity waves. In particular, kinetic energy forward cascade due to IGWs can be classified into two mechanisms; (i) stimulated generation of forward cascade of kinetic energy by near-inertial waves from balanced flows (Gertz and Straub, 2009; Rocha et al., 2018) and (ii) spontaneous generation of near-inertial waves from balanced flows (Nagai et al., 2015; Shakespeare and Hogg, 2017). In stimulated generation, near-inertial waves are first introduced by external forcing (e.g. wind) at the inertial frequency and then grow by extracting energy from the balanced flow (Barkan et al., 2017; Thomas, 2017; Gertz and Straub, 2009) while

spontaneous generation is the emission of waves by unbalanced, large Rossby number flow at density fronts without external forcing. These waves then radiate vertically downwards into the interior and amplify by extracting energy from deep balanced flow (Shakespeare and Hogg, 2017). Spontaneous generation is localized at sharp submesoscale fronts and is not very efficient at small Rossby numbers (Danioux et al., 2012; Nagai et al., 2015; Shakespeare and Hogg, 2017). On the other hand, stimulated generation is efficient at small Rossby number provided that the waves are forced externally.

Recent works have highlighted that these two classes of motions; submesoscale motions and internal gravity waves are out of phase seasonally (Rocha et al., 2016). Submesoscales motions are more stronger than IGWs in wintertime. The emergence of submesoscales is due to winter favored mechanisms such as mixed layer instability, wind-induced frontal instability among other processes (Callies et al., 2015b; Qiu et al., 2014; Sasaki et al., 2014; Brannigan et al., 2015; McWilliams, 2016). On the other hand, the kinetic energy associated with internal gravity waves shows stronger amplitude in summertime. This is due the intensification of vertical normal modes and shallow mixed layer (Callies et al., 2015a; Rocha et al., 2016). Having said that, due to high-frequency winds and tidal motions, energy extraction via IGWs seems to be a highly probably means of (balanced motions) kinetic energy sinks. Most of the previous study has focused on the impact of wind-generated near-inertial waves on energy dissipation (see Rocha et al. (2018) for summary). Whereas little is known as to the role of internal tides on kinetic energy exchanges. Although we know that internal tides contributes to the building up of internal gravity waves continuum (Garret-Munk spectra) and that their energy eventually contributes to dyapycnal mixing in the ocean interior. But weather they could be playing a significant role in down-scale transfer of kinetic energy is yet to be fully explored.

In this study, we focus on investigating the role of IGWs on cross-scale kinetic energy exchanges in a regime with active submesoscale motions and externally forced internal tides. We show that externally forced IGWs enhances KE dissipation in summertime by catalyzing the transfer of energy from balanced motion to dissipative scale. We do this by using a twin submesoscale resolving numerical simulations (with/without tides) of the North Atlantic Ocean with a horizontal resolution of $1/60°$. The only difference between the two simulations is the inclusion of tidal forcing. This permit to investigate how IGWs (particularly internal tides) affect kinetic energy exchanges in the presence of active submesoscales motions.

This paper is organized as follows, in the next section, we describe the numerical simulations. In section three (3), we present the seasonality of balanced motions and internal gravity waves characterized by the kinetic energy frequency-wavenumber spectral density. The contribution of balanced motions and internal gravity waves to the kinetic energy transfer is presented in section four (4). We discuss the impacts

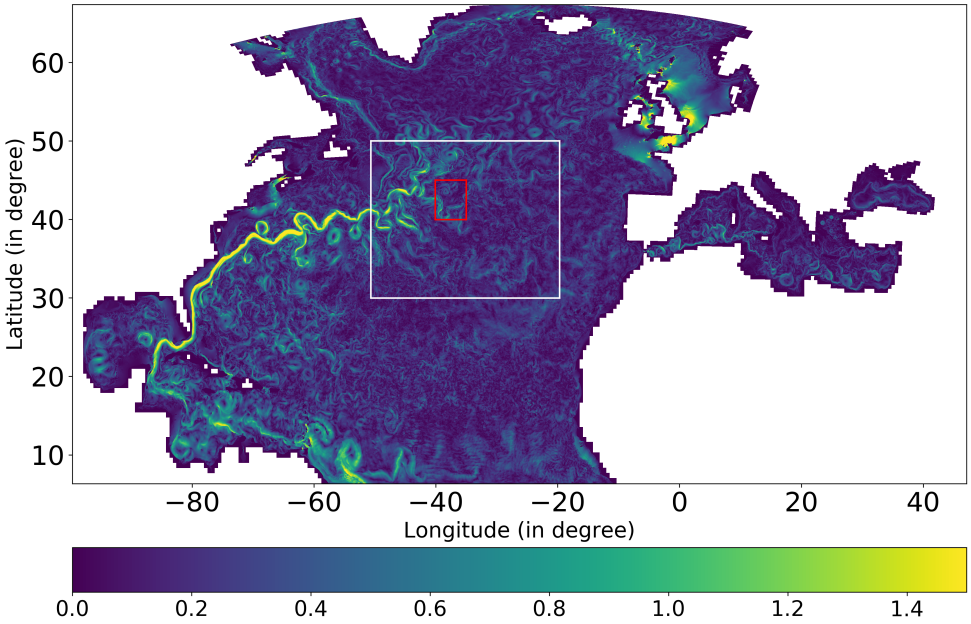

Figure 1: Snapshot of surface speed of eN60-WT (with tidal forcing) on the 1st of March. The Big box is the domain of interest and the small box corresponds to the region where we compute frequency-wavennumber spectra.

of this observed seasonality on the kinetic energy spectral flux and we identify two different mechanisms that support a direct cascade of energy in a dynamical regime with/without tidal motions.

2 North Atlantic Ocean Simulation

In this study, we use numerical outputs from a NEMO-based submesoscale eddy-permitting simulations of the North Atlantic with horizontal resolution of 1/60° (eNATL60). eNATL60 is a spatially-extended version of NATL60 (Le Sommer et al., 2019). The simulation spans the North Atlantic ocean from about 6°N up to the polar circle. This simulation has a horizontal grid spacing ranging from 1.6 km at 6°N to 0.9 km at 65°N. The model has 300 vertical levels with a resolution of 1 m at the top-most layers to better resolve a realistic surface boundary layer. In practice, the model effective resolution is about 10-15 km in wavelength, the same as the resolution of the anticipated Surface Water and Ocean Topography (SWOT) altimetry mission (Fu and Ubelmann, 2014). The initial and open boundary conditions are based on

GLORYS2v3 ocean reanalysis with a relaxation zone at the northern boundary for sea-ice concentration and thickness. The atmospheric forcing is based on ERA-Interim (ECMWF), the grid and bathymetry follow (Ducousso et al., 2017). To implicitly adapt lateral viscosity and diffusivity to flow properties, a third-order upwind advection scheme is used for both momentum and tracers in the simulation. The model is spin-up for a period of 18 months, and a one-year simulation output from July 2009 to June 2010 is used in this study. eNATL60 has two identical runs (i) eNATL60 with tidal forcing herein referred to as eN60-WT and (ii) eNATL60 with no tidal forcing eN60-NT. The two simulations have perfectly the same configuration except for the inclusion of tidal motions in eN60-WT. In the rest of this article, we use eNATL60 to refer to the two simulations while individual runs are addressed as eN60-WT (with tides) or eN60-NT (no tides). The inclusion of tidal forcing in eN60-WT run provides the conversion of tidal energy into the internal wave field through, both, flow-topography interactions and wave-balanced motions interactions (Arbic et al., 2008). Consequently, the comparison between the two simulations allows diagnosing the impacts of the internal tides on cross-scale energy transfer in the North Atlantic.

To investigate cross-scale energy exchanges between the different scales of motions, we estimate kinetic energy spectral density in frequency-wavenumber space as a proxy to understand the energetic nature of balanced/unbalanced motions in regimes with/without tidal motions. Also, we estimate the rate at which nonlinear mechanisms exchange energy across temporal and spatial scales in the two scenarios. In what follows, our analysis of KE density and transfer is based on hourly output of horizontal total velocity field and is computed using the following equations;

$$\frac{\partial \hat{KE}}{\partial t} = T_{KE} \;\; + \;\; \widehat{\mathbf{u}}^* \cdot OT \tag{1}$$

$$\hat{KE} = \frac{1}{2}\widehat{\mathbf{u}}^* \cdot \widehat{\mathbf{u}} \tag{2}$$

$$T_{KE} = -\widehat{\mathbf{u}}^* \cdot [\widehat{\mathbf{u} \cdot \nabla \mathbf{u}}] \tag{3}$$

Equation (1) to equation (3) is derived from the Fourier transform of momentum equation multiplied by horizonatal velocity field (Scott and Wang, 2005; Capet et al., 2008b; Müller et al., 2015). In the momentum equation (eq. 1), KE and T_{KE} represents the kinetic energy density and kinetic energy transfer respectively while OT stands for "Other Terms". $\hat{[\,]}$ refers to the Fourier transform and * represents the complex conjugate. Before performing spectral analysis the 2D time series were detrended and windowed in space and time. The procedure performed in this study

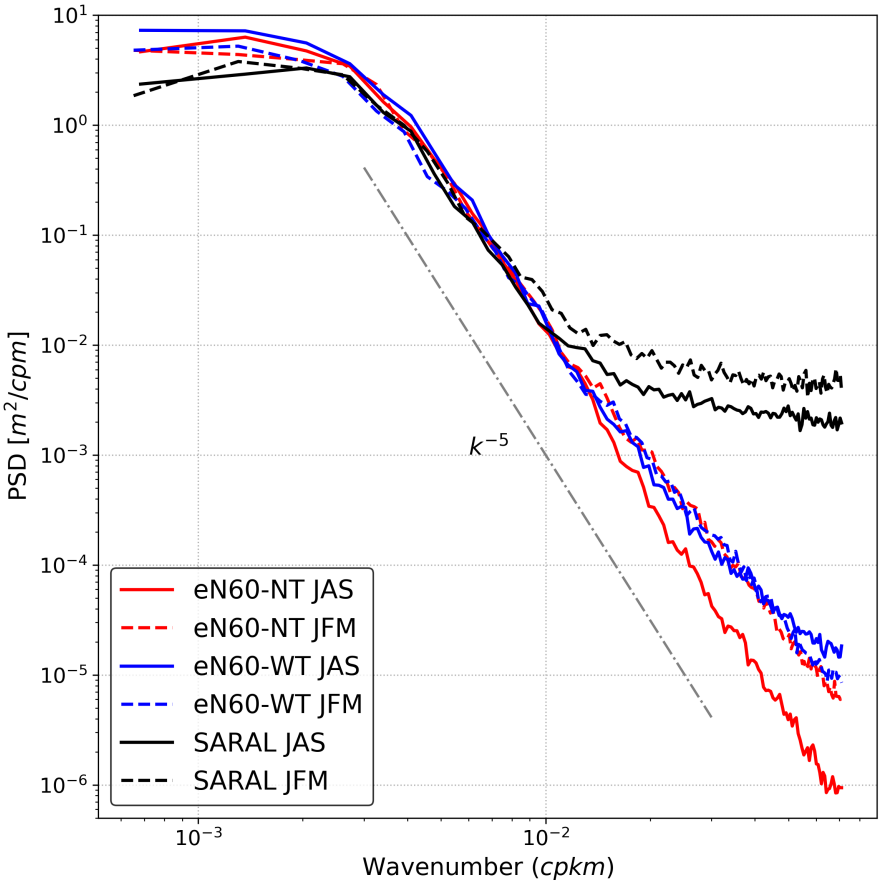

Figure 2: Comparison of SSH wavenumber spectra between eNATL60 and SARAL Alika satellite.

is consistent with standard procedures previously used in Rocha et al. (2016),Müller et al. (2015) and Torres et al. (2018).

We presents in figure 1, the snapshot of surface speed in eN60-WT. The simulation resolves well to a reasonable extent mesoscale motions, submesoscale motions, and IGWs. Very visible from the plot is the famous North Atlantic Gulf stream and its separation. The tidal motions are equally visible in the English Channel and the North sea. To assess the fidelity of the model to reproduce energy level at different temporal and spatial scales, we compare the spectral density obtained from the Sea Surface Height (SSH) of SARAL/AltiKa satellite altimeter with that of eNATL60 both in winter and summer. For this comparison, we used SSH values in a region centered at the middle of the North Atlantic (70°W to 60°W, 30°N to 40°N, Figure 1). This comparison of SSH spectral density is presented in Figure 2 and the SSH variance of the model output compares well with the satellite dataset for scales $>$ 100km. The difference at scales $<$ 100k is due to the satellite instrument noise level. Also, there seems to be quite a robust agreement between the two runs of eNATL60 simulations in wintertime. However, of particular interest is the difference between

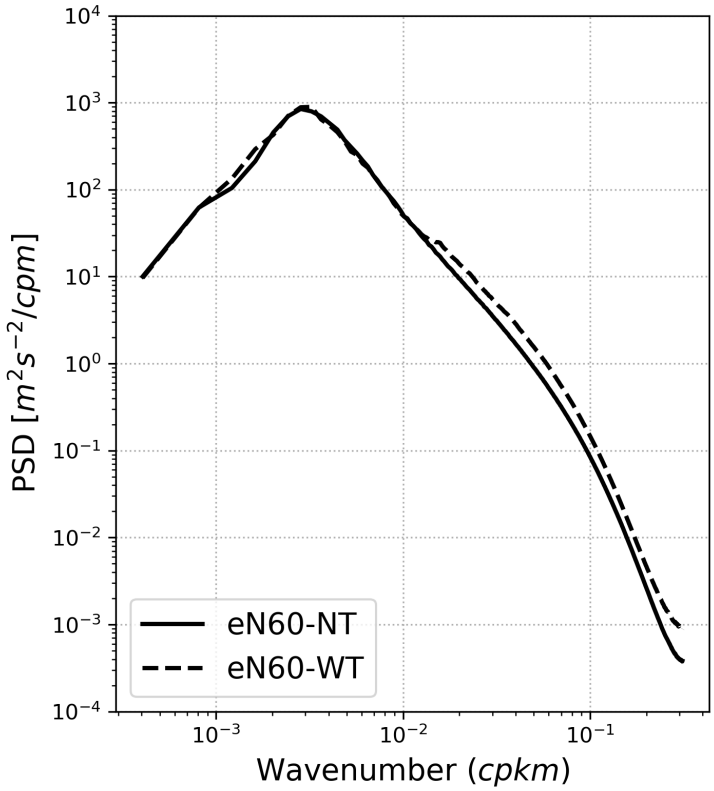

Figure 3: (a) One year average of kinetic energy wavenumber spectral density computed from hourly outputs of eN60-NT (no tides) and eN60-WT (with tides)

the runs in summertime where variance at fine-scales are of higher magnitude in eN60-WT compared to eN60-NT.

A similar analysis of the kinetic energy spectral density in the same region (Figure 3), show that the variance associated with fine-scale motions smaller than 100km is higher in the eN60-WT compared to eN60-NT. So what are the mechanism/dynamics at fine-scales in eN60-WT that could be responsible for this higher variance? A possible answer to this is that the inclusion of tidal motion in eN60-WT simulation is responsible for enhanced wave activity and this is why we see higher variance at fine scales in the SSH and KE spectra density plot. To qualitative investigate this, we separate the flow into its rotational and divergent part which represents the balanced and the unbalanced wave motions respectively. Figure (4) presents the spectral density for these two components. The spectral of the rotational part for the two runs are almost indistinguishable and this indicates that both simulations are identical in terms of the resolved geostrophically balanced motions. However, the spectral of the divergence part of the kinetic energy is very different between the two simulations. This difference is obvious at scales less than 500km and indeed, the divergent motions are more energetic in eN60-WT by a factor of 2

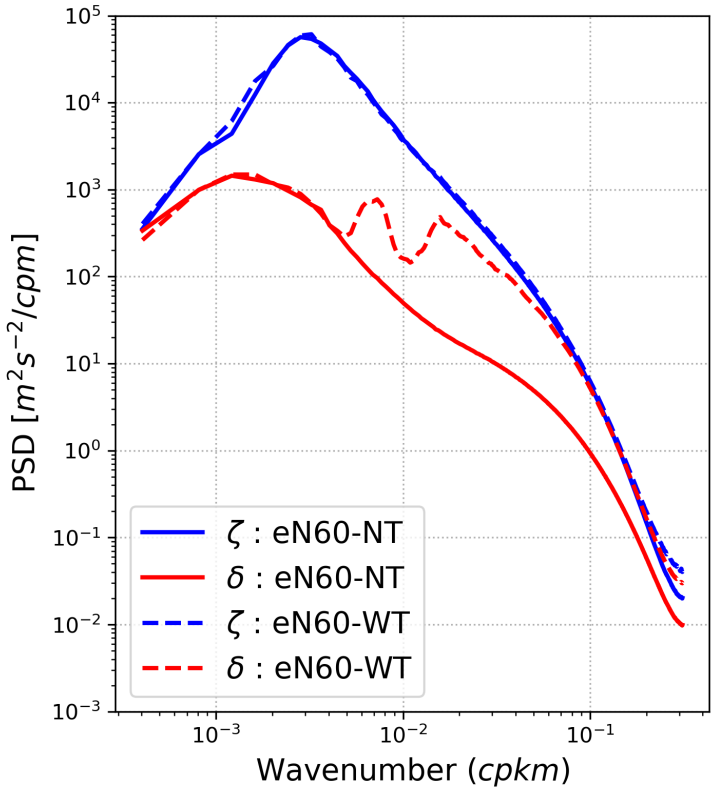

Figure 4: (a) Helmholtz decomposition of kinetic energy into rotational (ζ) and divergent (δ) spectral components. thick line (eN60-NT) and dashed lines (eN60-WT)

with two interesting peaks. We can conclude from this that the higher variance in eN60-WT at fine-scales compared to eN60-NT is primarily due to stronger divergent wave motions in eN60-WT and this is caused by the inclusion of tidal forcing in this simulation.

3 Seasonality of BMs and IGWs

In this section, we present the different classes of motions and their seasonality on the basis of wavenumber-frequency decomposition. This diagnostic will help to better understand how the difference in wave activity between the two simulations affects the spectral signature of oceanic motions across different temporal and spatial scales. For simplicity, we would refer to frequency-wavenumber spectra as ω-k spectral. Following Torres et al. (2018), we begin by presenting a schematics (Figure 5) showing the different observable dynamical regimes in the ocean as a function of their temporal and spatial scale. These classes of motions starting with low frequency, small wavenumber motions to high-frequency, high wavenumber mo-

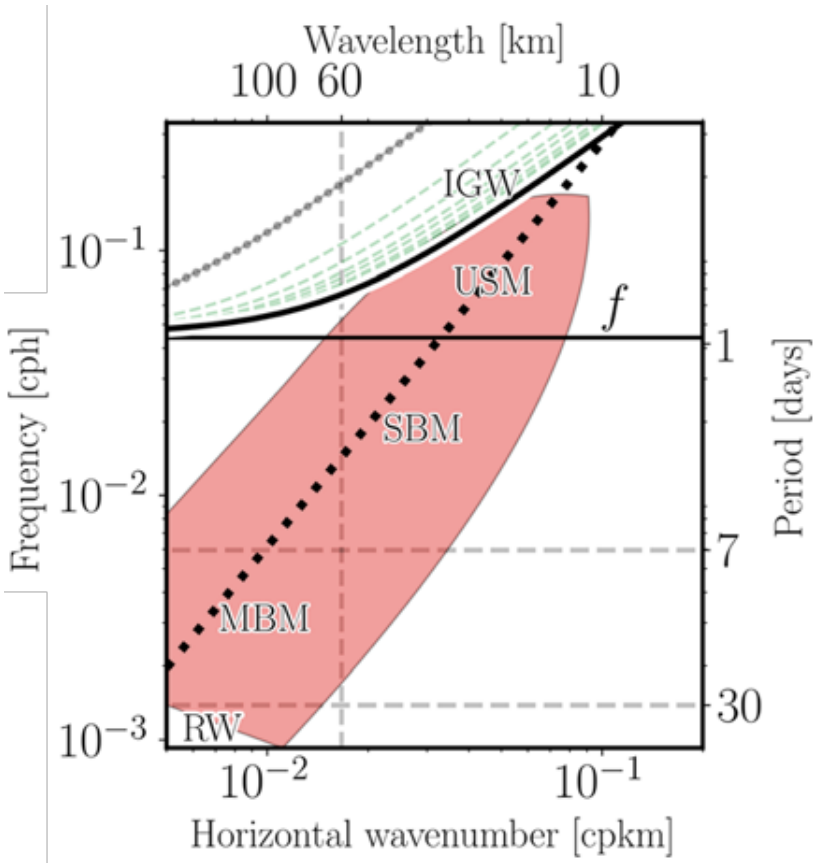

Figure 5: A schematic of the observable dynamical regimes with different classes of motions in the ocean. These classes of motions starting with low frequency, small wavenumber motions to high frequency frequency, high wavenumber motions are Rossby waves(RW),Mesoscale balanced motions (MBM) ,Submesoscale balanced motions (SBM), Unbalanced submesoscale motions (USM) and Internal gravity waves (IGW)

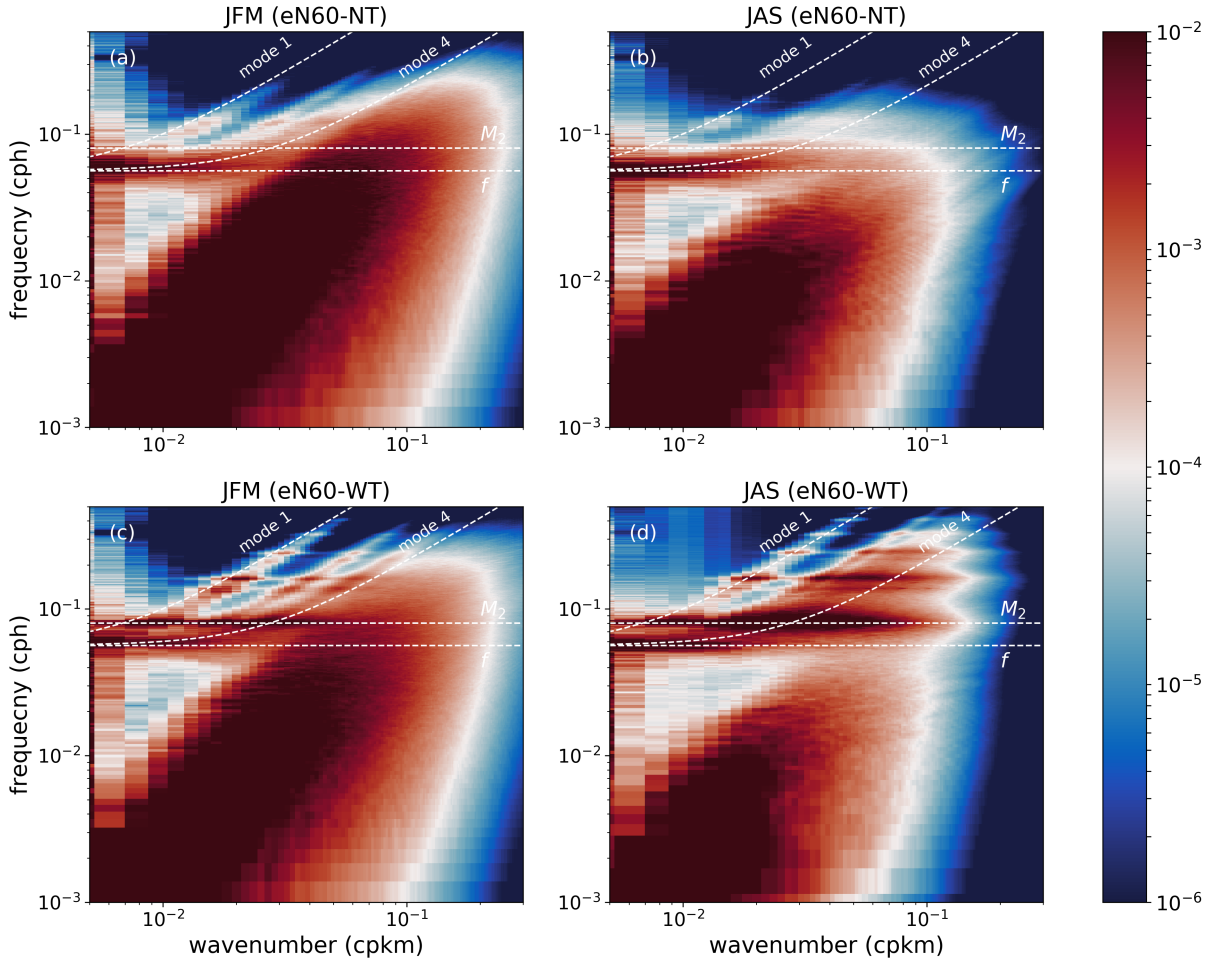

Figure 6: Kinetic energy frequency-wavenumber spectral computed from hourly outputs of eN60-NT (no tides) and eN60-WT (with tides) for winter (JFM) and summer (JAS) time.

tions are Rossby waves(RW), Mesoscale balanced motions (MBM), Submesoscale balanced motions (SBM), Unbalanced submesoscale motions (USM) and Internal gravity waves (IGW). In this study, we focus more on understanding how IGWs and BMs (in the presence of tidal motions) affect cross-scale kinetic energy transfer. Due to computational cost of this diagnostic tool, we decide to perform the ω-k spectra analysis in a 5° x 5° (−40° to −35°, 40° to 45°) box located inside the previous large box (Figure 1).

We show in Figure (6), the winter and summer averages of kinetic energy ω-k spectra for the two runs. In the Figure, the upper panel corresponds to eN60-NT and the lower panel for eN60-WT. From these plots, we recover fairly the classes of motions described previously in Figure (5). The winter-summer contrast clearly shows a strong seasonality of submesoscale balanced motions and internal gravity waves. In wintertime, for eN60-WT (simulation with tidal forcing), energy is mostly

concentrated in BMs, near-inertial waves and in the dispersion curve of IGWs while in summertime, energy is mostly concentrated in the mesoscale BMs, near-inertial waves and internal tides. In summary, the variance associated with submesoscale BMs is stronger in winter while that of IGWs is stronger in summer. This out of phase seasonality of submesoscale BMs and IGWs is consistent with the findings of Rocha et al. (2016) and Torres et al. (2018). IGWs are stronger in summer due to shallow mixed layer depth and the intensification of vertical normal modes while submesoscale BMs are stronger in winter because they are driven by winter favored mechanism such as frontogenesis, wind-induced frontal instabilities and mixed layer instability among other processes (Callies et al., 2015b; Qiu et al., 2014; Sasaki et al., 2014; Brannigan et al., 2015; McWilliams, 2016).

Similarly, eN60-NT resolve fairly the same classes of motion as eN60-WT except that IGWs are less energetic in this simulation. In fact, we do not resolve internal tides in eN60-NT with the obvious reason that is connected to the absence of tidal forcing in this simulation. In wintertime, energy is mostly concentrated in BMs, near-inertial waves and dispersion curve of IGWs. This is consistent with winter dynamics in eN60-WT. In summertime, energy is concentrated in mesoscale balanced motions and near-inertial waves. Unlike eN60-WT, the seasonality observed in eN60-NT is associated with stronger submesoscale BMs and IGWs in winter. We see in Figure (6) that the seasonality of IGWs is reversed in eN60-NT (simulation without tidal forcing). How can this be? we know that the classical paradigm for the generation of IGW continuum is that winds produce near-inertial waves, barotropic tidal flow over topographic features creates internal tides and the energy in the dispersion curve are due to nonlinear interactions. Both simulations are forced with realistic high-frequency winds with 3-hourly outputs. These winds are stronger in winter, hence a well resolved near-inertial wave and IGWs dispersion curves in winter. The dynamics in summertime is different between the two runs. For eN60-WT simulation, internal tides generated by tidal motions are amplified by shallow mixed layer in summertime and nonlinearity produce energy in IGWs dispersion curve. For eN60-NT, the mechanism for generating waves in summertime are relatively weak; no tidal forcing and weaker winds, hence a relatively weak wave motions in summer.

The KE spectra integrated over all wavenumbers for the two runs are presented in Figure 7. In summertime the variance at high frequencies is higher in eN60-WT compared to eN60-NT. This is due to the amplification of internal gravity waves by tidal motions. eN60-WT spectra approximately follows the estimated Garrett-Munk spectra in summertime. Clearly visible in eN60-WT spectra are the peaks at inertia frequency and the M_2 tidal frequency. We only recover the peak at inertia frequency in eN60-NT. To a large extent, we now understand the dynamics responsible for the differences in kinetic energy density that we see in the two simulations. In the following sections, we shall discuss how the different classes of motions redistribute

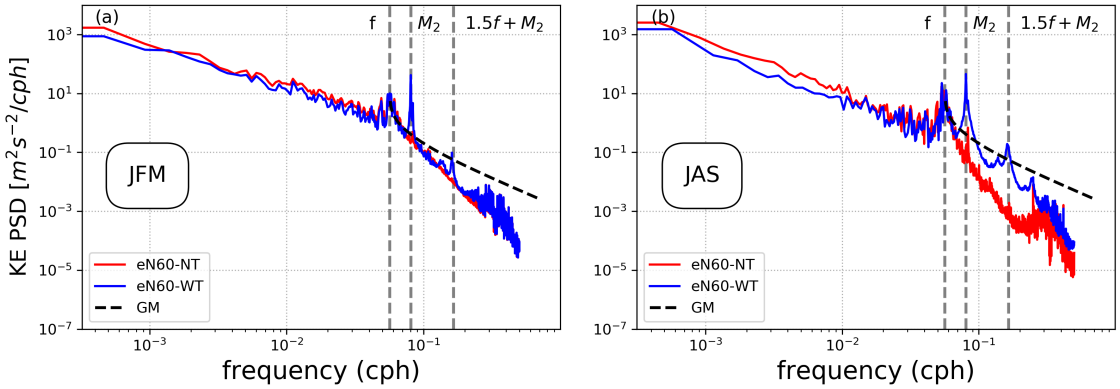

Figure 7: Kinetic energy spectral density integrated over all wavenumbers for eN60-NT (no tides) and eN60-WT (with tides). The two grey dash line represents the inertia frequency and the M2 tidal frequency. The dashed black line represents the estimate of the Garrent Monk spectra computed with reference values of total energy of the internal wavefield and stratification set to $E0 = 6.3e^{-5}m^2s^{-2}$ and $N_0 = 5.2e^{-3}s^{-1}$, respectively. (a) Winter (JFM) and (b) Summer (JAS).

energy in different dynamical regimes

4 Modulation KE forward flux by IGWs

In this section, we are going to discuss the impact of resolving submesoscale and internal tides on the direction of kinetic energy cascade. We do this in spectral space by estimating the net energy passing through each individual wavenumbers. The spectral flux is obtained by integrating the energy transfer (equation 3) from a particular wavenumber k to k_0 (the wavenumber corresponding to the box size).

We present in Figure 8, the annual mean of the spectral flux for the two simulations. The overall shape of the flux is consistent in the two simulations with a net inverse cascade at a scale larger than 50km and a net forward cascade at a scale smaller than 50km. The magnitude of the forward cascade at high wavenumbers in eN60-WT is higher compared to eN60-NT. Given that the difference between the two simulations is the inclusion of tidal forcing in eN60-WT, it is interesting to see that the enhanced wave activity by tidal forcing has an impact on the magnitude of kinetic energy cascade. We understand from previous section that this enhanced wave activity is more pronounced in summertime. In fact, we shall show that the difference in the kinetic energy flux between the two simulations is particularly due to higher magnitude of forward cascade in eN60-WT in summertime. We present in Figure 9, the winter and summer averages of kinetic energy spectral flux. In wintertime and in the two simulations (Figure 9b), the flux is identical across all

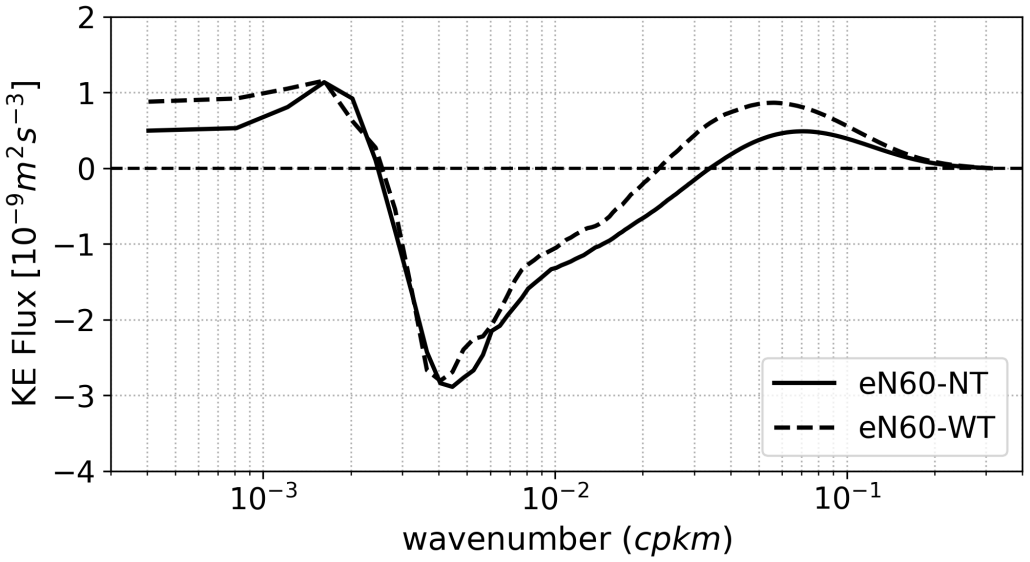

Figure 8: (a) One year average of kinetic energy spectral flux computed from hourly outputs of eN60-NT (no tides) and eN60-WT (with tides)

wavenumbers. The forward cascade starts at around 25km and extends down to a kilometric scale. In summertime (Figure 9a), the magnitude of the forward cascade differs significantly between the two runs at high wavenumbers. The magnitude of the forward flux in eN60-WT is a factor of 4 compared to eN60-NT. This differences in cascade clearly highlights how internal tides enhance forward cascade of kinetic energy at high wavenumbers in summertime.

So far the kinetic energy cascade is based on surface horizontal velocities. Of great interest is to understand the nature of the kinetic energy cascade in the interior of the ocean. We are curious to know if the forward cascade at high wavenumbers is surface confined or not. In Figure (10), we present the spectral flux computed at 32 different vertical levels in the water column. Both in winter and summer, the average kinetic energy spectral flux in the two simulation is characterized by a net inverse cascade that extends down to around 700m in the interior. In wintertime, the forward cascade in eN60-WT (Figure 10a) is strong both at the surface and in the interior. Whereas in eN60-NT (Figure 10c), the forward cascade is confined mostly to the surface. In summertime, the forward cascade in eN60-WT (Figure 10c) span the upper ocean but with a gradual decrease in magnitude as you go down the water column. Whereas in eN60-NT (Figure 10d), the forward cascade is almost zero throughout the upper ocean. A stronger forward cascade (in summertime for eN60-WT) in the interior is an indication that internal tides can serve as a substantial route of kinetic energy to dissipative scale in the ocean.

We have to come to understand that internal tides enhance the energetics of IGWs

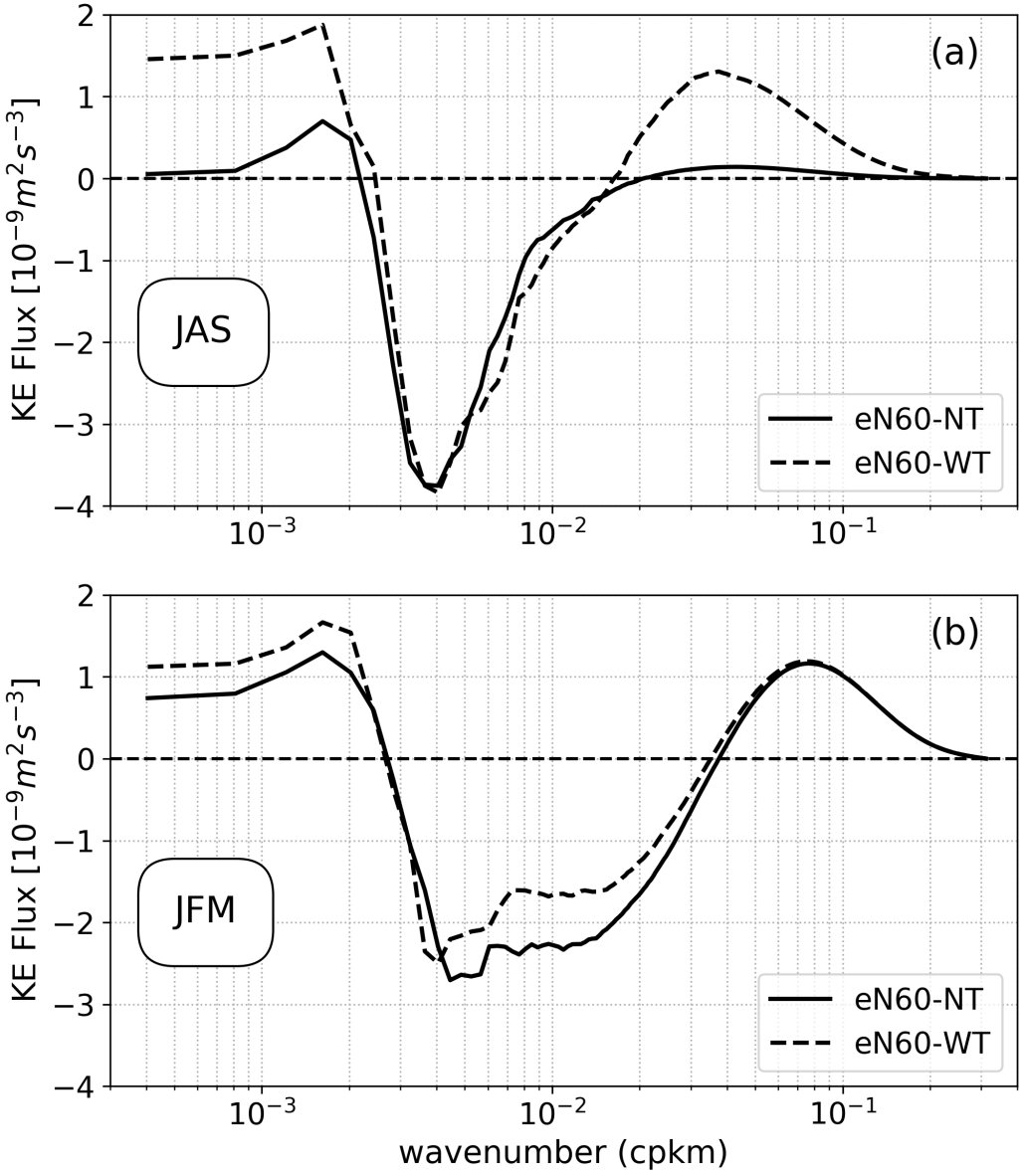

Figure 9: Kinetic energy spectral flux computed from hourly outputs of eN60-NT (no tides) and eN60-WT (with tides). (a) summer : July, August and September (b) winter : Janaury, February and March

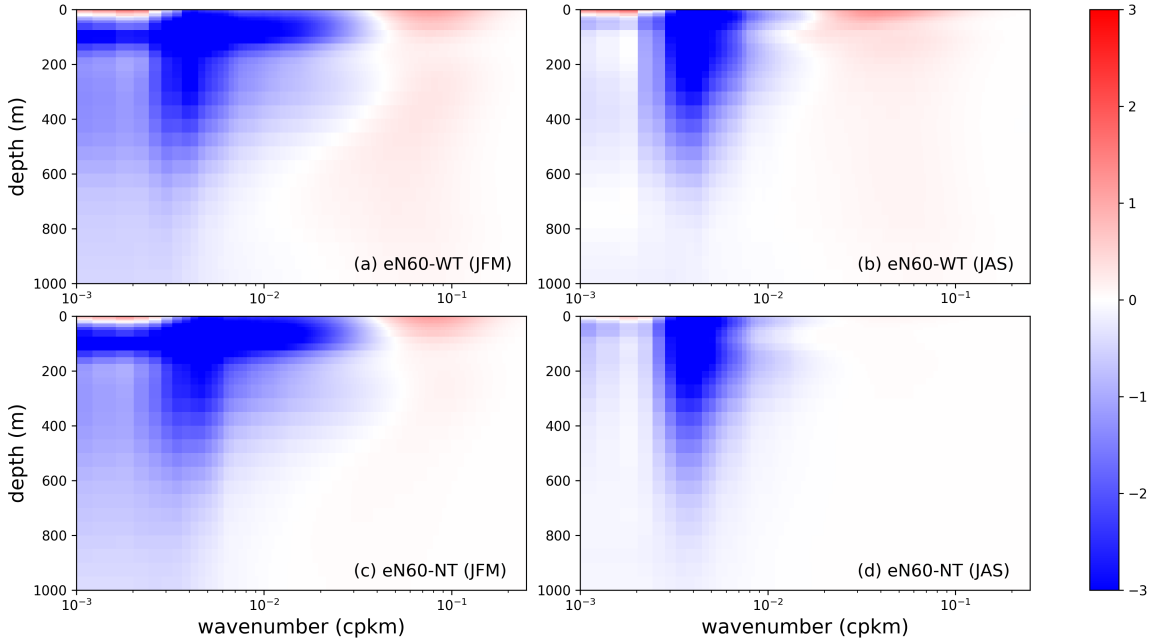

Figure 10: Winter and summer averages of kinetic energy spectral flux as a function of depth for eN60-NT and eN60-WT.

and in particular enhance forward cascade of energy in summertime. To better explain how internal tides modify cross-scale energy exchanges among different classes of motion, we present the kinetic energy transfer in frequency-wavenumber space. We present in Figure 11 the winter and summer averages of kinetic energy spectral transfer in frequency-wavenumber space. In the ω-k spectra, negative values of spectra transfer imply that non-linearity extract energy from these regions to feed other regions with positive values. In other words, sinks of energy are characterized by positive values while a source of energy has negative values.

We start by discussing the spectral transfer in wintertime (left column of Figure 11). In eN60-NT, the largest negative values of the spectral transfer show that energy is being extracted from the balanced motions (source of energy) while near-inertial motions and motions with scale less than 10km are the major sinks of kinetic energy. The rate of non-linear exchanges in eN60-WT is fairly identical with eN60-NT except for the intensification of energy gained by IGWs in eN60-WT. In concise, submesocale motions and internal gravity waves are sinks of kinetic energy in wintertime with the former playing the major role.

The summer spectra differ significantly between the two runs. In eN60-NT, balanced motions are the major source of energy while energy is gained mostly by near-inertial motions. The transfer at high frequencies and wavenumbers is almost zero, i.e high-frequency motions and submesoscale motions are less energetic in eN60-NT in summertime. This is consistent with what we saw in the KE spectra density. In

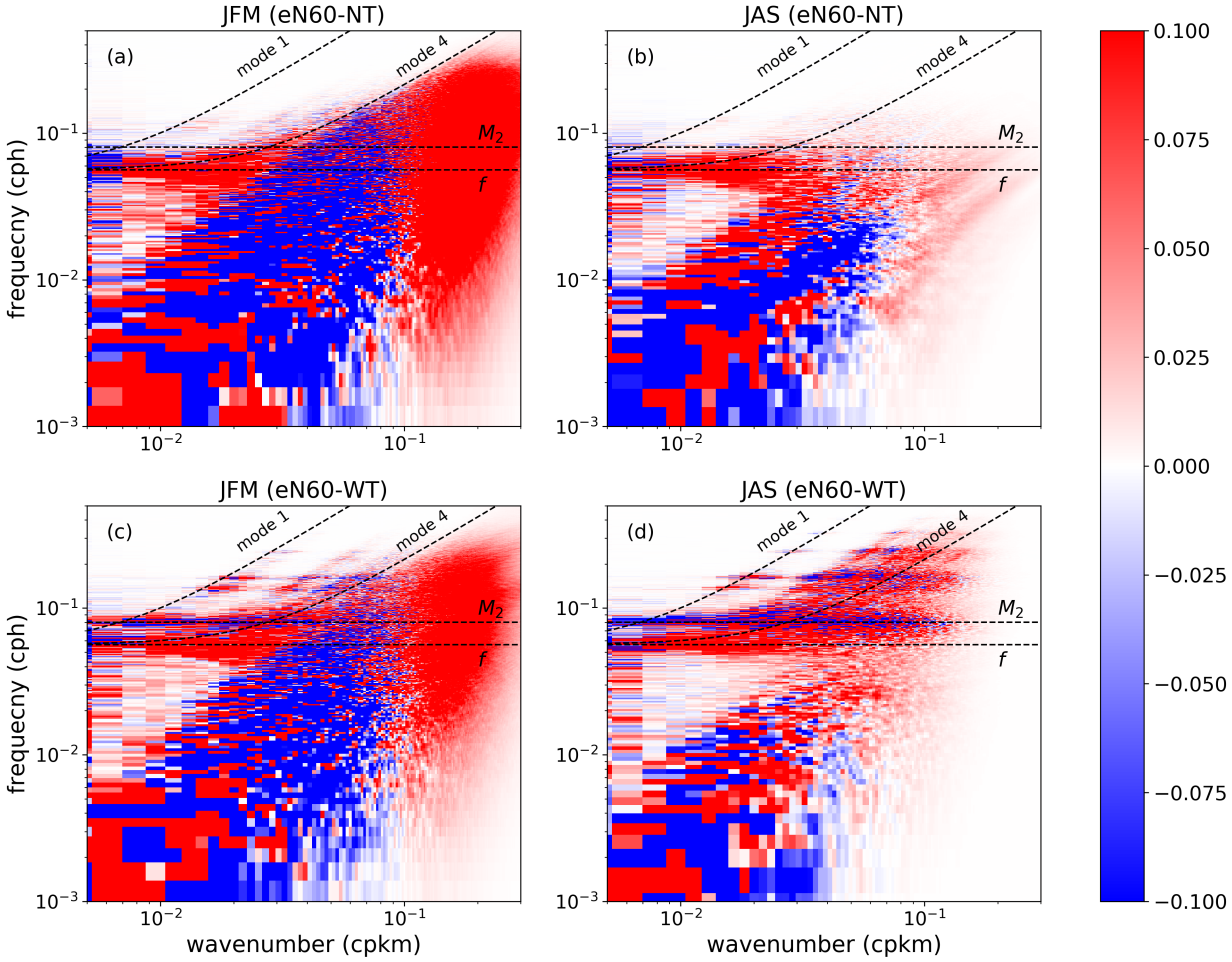

Figure 11: Kinetic energy transfer in frequency-wavenumber space computed from hourly outputs of eN60-NT (no tides) and eN60-WT (with tides) for winter (JFM) and summer (JAS) time.

eN60-WT, the narrative is different. The major source of energy is the mesoscale balanced motions and the internal tides (M_2 semi-diurnal tides). Near-inertial waves, submesoscale BMs and IGWs dispersion curves are seen in Figure (11) to be sinks of energy.

In concise, there are two mechanisms of energy extraction in summertime. (i) In a flow without tidal forcing, near-inertial waves extract energy from balanced motions and (ii) in a flow with tidal forcing, near-inertial waves and IGWs dispersion curves extract energy from internal tides and mesoscale balanced motions. In summary, the forward cascade in eN60-WT, is associated with the transfer of energy by non-linearity from balanced motions and internal tides to near-inertial waves and IGWs dispersion curves. This is possible due to the intensification of IGWs in the presence of tidal motions. The lack of tidal motions in eN60-NT (compared to eN60-WT) shows how effective internal tides are providing a route to energy dissipation in sum-

mertime, both at the surface and in the interior. This strongly emphasizes the need to include tidal forcing in ocean model simulations in order to accurately capture cross-scale energy exchanges at fine-scales.

5 Summary and Conclusion

The role of internal tides on the seasonality of kinetic energy density and transfer is investigated in this study. Our analysis is based on the output of a realistic simulation of the North Atlantic with a horizontal resolution of 1/60°. We used two outputs of this simulation; simulation with/without tidal forcing. These twin experiments permit to investigate how internal tides generated by tidal forcing modify kinetic energy variance, cross-scale exchanges and its seasonality. We found that the seasonality of IGWs is sensitive to tidal forcing. In simulation without tides, IGWs are stronger in winter whereas, in simulation with tides, they are stronger in summer. The latter condition is consistent with the findings of Rocha et al. (2016) and Torres et al. (2018). Also, our result shows that resolving internal tides in the presence of energetic submesoscale motions have strong impact on kinetic energy transfer in summertime. The magnitude of the estimated forward cascade (both at the surface and at depth) in the simulation with tidal forcing is a factor 4 higher compared to the simulation without tidal forcing. Overall, we identified that there are two mechanisms that support kinetic energy forward cascade. Forward cascade due to energetic submesoscale motions in wintertime and forward cascade due to IGWs (enhanced by tidal forcing) in summertime. Our results underscores that at fine-scales, internal tides can provide an effective route to kinetic energy dissipation.

Chapter 6

Conclusion and Perspective

Contents

6.1 Context

In the context of future observing satellite missions, the Surface Water and Ocean Topography (SWOT) altimeter would be a landmark in oceanographic studies. SWOT would provide an unprecedented view of the ocean surface down to 10km - 15km in wavelength and this information would help oceanographers to better understand the dynamics of the ocean at intermediate scales (10km - 200km). This thereby would help bridge the gap between our knowledge of large scale motions (where energy is injected into the ocean) and microscale motions (where energy is dissipated).

In this thesis, we have used numerical simulations (capable of mimicking SWOT resolution) to investigate the impact of oceanic fine-scale motions (particularly submesoscale motions and internal gravity waves) on kinetic energy exchanges in the North Atlantic ocean. Outputs of several North Atlantic simulations based on NEMO and HYCOM ocean model were used in this thesis. We shall present in this chapter, the summary of the main findings of this thesis work, the key differences between NEMO & HYCOM simulations and the implications of our results for future work.

6.2 Thesis results

In chapter 1, we have divided the objective of this thesis into three research themes with each theme answering specific questions. In this section, we shall summarize the results of this thesis in light of these key research questions.

A: Seasonal and regional distribution of fine-scale eddy structures in the North Atlantic ocean.

What are the scales of oceanic eddies at fine-scales?
Our results show that most of the eddies in the North Atlantic with scales < 100km are nonlinear and the spread of eddy nonlinearity increases with latitude. The typical scale of these eddies lies between the Rossby radius and the Rhine scale. This result is consistent with the findings of Eden (2007) who investigated mesoscale eddies with a coarse simulation of the North Atlantic ocean.

What is the depth penetration of submesoscale eddies
The vertical structures of submesoscale eddy motion (diagnosed from the spectral coherence of relative vorticity) varies as a function of the mixed layer depth with higher amplitude in wintertime compared to summer. For eddies with scale > 100km (mesoscale eddies), the vertical scale extends into to the interior beyond 1000m and

does not undergo strong seasonality.

Is the scale of oceanic eddies sensitive to the seasonality of submesoscale motions

Estimates of enstrophy-containing scale the statistics of eddy-scale identified by eddy-detection algorithm showed that and the distribution of the scale of oceanic eddies in the North Atlantic undergoes strong seasonality. We found this seasonality to be directly linked to the emergence of submesoscale eddies that are driven by mixed-layer instability in wintertime. We found the scale of eddies in the North Atlantic to be on average smaller by a factor of 2 in wintertime compared to summertime. A large population of smaller eddies in wintertime reduces the value of the average size of oceanic eddies.

B: Kinetic energy transfer at fine-scale in a regime of energetic submesoscale motions.

Does the seasonality of submesoscale turbulence affect cross-scale kinetic energy exchanges ?

According to our results, kinetic energy exchanges undergo strong seasonality with a stronger forward cascade in winter at scales < 50km. This scale-range corresponds to scales of submesoscale motions. We found the flux at submesoscales to be almost zero in summer.

Is the forward cascade due to submesoscales surface-confined ?

The forward flux due to submesoscales in winter is mostly confined within the mixed-layer. This follows directly from the fact that submesoscales are energetic in winter and are mostly driven by mixed layer instability.

At fine-scale, (using geostrophic current), how accurate is the estimate of kinetic energy cascade?

In this thesis work, we found that the estimate of spectral flux based on geostrophic velocity differs from the results based on total velocity. The magnitude of the forward cascade at high wavenumbers is underestimated by the spectra flux estimated from geostrophic velocity. This result highlights the limitation we might face with kinetic energy exchanges that will be computed form SWOT data.

C: Kinetic energy transfer at fine-scale in a regime of externally forced internal tides

What is the impact of internal tides on kinetic energy distribution at fine-scales

Internal tides have strong impacts on the distribution of kinetic energy in the ocean,

particularly at fine-scales. Our result confirms that internal tides introduced via tidal forcing enhance wave activity. This is pronounced in the diurnal and semi-diurnal tidal frequencies and in general, we see the intensification of variance along the internal gravity waves dispersion curve. This variance is particularly strong in summertime.

How do internal tides modify kinetic energy cascade
Internal tides modify kinetic energy cascade by directly serving as a source of energy that feeds the internal gravity wave continuum in summertime through nonlinear exchanges.

Can internal tides provide a route to kinetic energy dissipation
Internal tides can indeed provide a route to kinetic energy dissipation. Our result shows that non-linear exchanges in the internal gravity wave continuum (due to externally forced internal tides) drives a forward cascade of energy. This process can be classified as a simulated generation of the forward cascade by internal gravity waves because internal gravity waves in this scenario are externally forced by tidal motions.

6.3 Summary on model comparison

In this thesis, we have used 3 numerical simulations of the North Atlantic ocean based on NEMO (NATL60, eNATL60) and HYCOM (HYCOM50). These simulations differ specifically in terms of numerical configuration, vertical resolution, and duration of model spin-up. Their simulation output shows strong similarity in terms of the large scale and mean circulation pattern of the North Atlantic. Also, all three simulations adequately characterized fine-scales dynamics down to 15km in the North Atlantic. This is relevant for the upcoming SWOT mission because information such as the variability of scales of eddy motion would be useful in the calibration of inversion techniques for estimating two-dimensional maps of SSH from SWOT data. However, there are notable differences between the simulations that are worth been highlighted. We shall present below a summary of the comparison between the simulations in terms of the results of this thesis work. This comparison would be useful for numerical ocean modelers that might be interested in knowing the similarity/difference between NEMO and HYCOM simulation output.

Higher amplitude of KE and larger eddies in HYCOM50
From our analysis of surface eddy kinetic energy and velocity spectra, we found that HYCOM50 shows a higher amplitude of kinetic energy level compared to NATL60, particularly along the Gulf stream. Also, the scale of resolved eddies at fine-scales in HYCOM50 seems to be a larger compared to NATL60. We believe that this

disparity between the two simulations in terms of the energy levels and the scale of eddies could be due to a shorter length of spin-up for NATL60 (6 months) compared to HYCOM50 (20 years).

Stronger submesoscale eddy buoyancy flux in NATL60
NATL60 and HYCOM50 simulation reproduce similar statistics of surface relative vorticity. Both simulations capture the seasonality of submesoscale motions diagnosed through the vorticity wavenumber spectra and submesoscale eddy buoyancy fluxes ($w^I b^I$). The magnitude of $w^I b^I$ for the two simulations in the mid-latitude Gulf stream region is very similar. Whereas in the subpolar region, the values for HYCOM50 are slightly smaller compared to NATL60 for both wintertime and summertime despite, HYCOM50 having a deeper mixed layer in this region. The vorticity spectral density for the two simulations is identical except that there is a tendency for HYCOM50 to show a sharp increase in variance at high wavenumber in high EKE regions. This observation suggests that the subgrid-scale parametrization in HYCOM50 is probably weak at damping enstrophy at a kilometric scale.

Stronger KE cascade in HYCOM50
Another major difference between the two simulations is the vertical resolution: 32 hybrid vertical layers in HYCOM50 versus 300 z-levels in NATL60. Initially one would think that the coarser vertical resolution in HYCOM50 could significantly lead to a difference in the representation of the kinetic energy flux compared to NATL60. From the kinetic energy spectral flux as a function of depth, we found that the inverse cascade of energy in HYCOM50 is not surfaced intensified and that having only 32 isopycnal vertical levels is not detrimental to the representation of the dynamics in the ocean interior. Also, we found the vertical penetration of eddies to be essentially identical in the two simulations.

6.4 Future perspective

In this thesis work, we focused on oceanic fine-scales motions and how they affect the distribution and the exchanges of kinetic energy. We have equally investigated the impact of submesoscale turbulence on the variability of scales of oceanic eddies in this regime. The results of this thesis work provides supporting evidence as to the role of fine-scale motions in ocean dynamics as highlighted in the previous sections. However, these results are not without caveats and thereby have room for improvement.

Our results have shown that at fine-scales, submesoscale balanced motions and unbalanced wave motions can provide a route to kinetic energy to dissipative scales. Several diagnostics could be made as an extension to the results of this thesis work.

Torres et al. (2018) showed the isolated contribution of these classes of motions to the kinetic energy density in the frequency-wavenumber domain by first separating the flow into the rotational and divergent part using Helmholtz decomposition and then estimating the spectral density of the individual component. A similar analysis for the kinetic energy spectra flux would illuminate the different spatial-temporal contributions of these classes of motion in kinetic energy exchanges. Additional insight on the impact of submesoscales on kinetic energy exchanges can be gained by estimating the frequency-wavenumber spectra of the buoyancy flux. This would provide information on the amount of energy that is transformed from potential to kinetic energy within the mixed-layer due to energetic submesoscale motions.

The results presented in this thesis are based on the output of an ocean simulation forced with realistic winds. Recent literature suggests that air-sea coupling at fine-scale affects the evolution and energetics of meso and submesoscale eddies. Renault et al. (2016) using a coupled/uncoupled model of the California Upwelling System argued that the ocean-atmosphere interactions have feedback that acts as an oceanic eddy killer. This feedback deflects energy from the geostrophic current into the atmosphere and dampens geostrophic kinetic energy. A possible future study would be to recompute the (kinetic energy transfer) diagnostics in this study using outputs of the ocean-atmosphere coupled model. This sort of future analysis would take into account the direct impact of air-sea interaction on kinetic energy exchanges in the ocean and maybe provide a more accurate estimate of the flux.

The kinetic energy flux presented in this thesis work is based on spectral analysis of the non-linearity term in the kinetic energy equation. The spectral analysis method relies upon an assumption of statistical homogeneity and also requires data pre-condition (detrending and windowing) before the application of Fourier transform. There are few caveats to this, the assumption of homogeneity is not valid every-where in the ocean and secondly, windowing function (if not carefully applied) can introduce artificial length scales into the spectral flux estimates (*see Appendix*). Recently, Aluie et al. (2017) developed a filtering approach based on a coarse-graining method to estimate kinetic energy flux. His method showed great consistency with the spectral method for large-scale kinetic energy flux with a little mismatch in non-homogeneous regions. The method also provides a way to avoid the tendency of spurious length scales in the spectral estimates. However, the result of this method is sensitive to the choice of the kernel used for filtering and it is therefore important to keep this in mind when comparing Aluie's approach to spectral method. Having said that, how these methods compare at fine-scales is currently not clear.

More recently Dewar et al. (2019) investigated cross-scale kinetic energy transfer using a somewhat different approach based on the application of Greens function to the kinetic energy equation. The authors applied this method to an idealized numerical simulation of vortex merger, resulting in the demonstration of the ex-

pected upscale energy cascade. While there is room for improvement, the results of this method provided a complementary view of how kinetic energy is exchanged between different scales of motion. Analysis of kinetic energy flux based on Aluie's and Dewar's method on a submesoscale resolving ocean model would be a promising scientific exercise. The findings of such an analysis coupled with the existing results based on the spectral method would solidify our knowledge of what we should expect from SWOT in terms of kinetic energy exchanges at fine-scales.

As a concluding remark, I would like to stress that the task of understanding the ocean has become a big data problem. The advancement in high-resolution ocean simulations is providing data in the order of petabytes coupled with the daily influx of observation from satellite and in-situ measurements. These large datasets have become more than what our personal computers can handle. The analysis and management of this huge volume of information require the creation of computing platforms and workflows that support reproducible research work. One of such resources currently available for oceanographic studies is PANGEO. PANGEO is a community platform for Big Data geoscience based on an interactive computing platform (Jupyter) and a flexible python analytic library for parallel computing (Dask). We have leveraged on the availability of this scientific tool to provide some of the results presented in this thesis work. Without mincing words, future scientific research; from data collection to finished article would very much depend on collaborative open-source scientific packages and cloud computing resources like PANGEO.

Appendices

Appendix A

Spectral Analysis

A.1 Introduction

This Appendix aims to present the diagnostics tools (based on spectra analysis method) that are used in this thesis work. This section is not intended to give a full nor thorough description of spectra analysis, a more comprehensive description of the spectral method can be found in major statistics textbooks. This present section of my thesis manuscript provides only the elements needed to understand the different spectral methods used in the thesis work.

A.2 Spectra density

Spectral analysis is a statistical method that is used to partition the variance of a time series as a function of frequency/wavenumber. In oceanography, it is efficiently applied to estimate the energy that is associated with different temporal/spatial scales of motions in a given time series. The estimation of the spectral density used in this thesis work is based on the periodogram method i.e a direct transformation of the time series to obtain its Fourier components by using Fast Fourier Transforms. Fourier analysis itself is based on the premise that any infinitely repeated time series with finite length can be represented by a linear summation of cosines and sines, and this approach is particularly effective for representing sinusoidal oscillations, which are frequently encountered in physical oceanography.

A.2.1 1D spectra

To begin, lets consider a time series $\phi(t) = (\phi_0, \phi_1, \phi_2 ... \phi_n)$ sampled at equally spaced time increment such that $t_n = n\Delta t$. This time series can be written in terms of its Fourier component, as;

$$\phi(t) = \bar{\phi(t)} \ + \ \sum_{n=1}^{\infty} [A_n cos(2\pi n f_1 t) + B_n cos(2\pi n f_1 t)] \tag{A.1}$$

where $\bar{\phi(t)}$ is the mean value of the time series, f is the frequency (cycles per unit time) and A_p, B_p are Fourier coefficients. Using exponential function, equation (A.1) can equally be written as

$$\phi(t) = \sum_{n=-\infty}^{\infty} a_n e^{i2\pi f_n t}, \tag{A.2}$$

where a_n, is the spectral amplitude (Fourier coefficient). This spectral amplitude provides a measure of the relative importance of each frequency component to the overall spectral variability. The **spectral density** at each frequency is the square of the spectral amplitude and it is written as

$$E_\phi(f_n) = \frac{a_n^2}{\Delta f} \tag{A.3}$$

In a spatial dataset, time (t) is replaced by the wavelength (λ) and the spectral density can be rewritten as

$$E_\phi(k_n) = \frac{a_n^2}{\Delta k} \tag{A.4}$$

where $k = 1/\lambda$ is defined as the wavenumber (cycles per unit distance).

A.2.2 2D wavenumber spectra

In this thesis, our analysis is based mostly on two-dimensional outputs of numerical ocean simulations with zonal (x) and meridional (y) components. Following a 1D time-series, a 2D time series $\phi(x, y)$ can be represented in terms of its Fourier components as

$$\phi(x,y) = \sum_{m=-\infty}^{\infty} \sum_{n=-\infty}^{\infty} a_{mn} e^{i2\pi(k_m x + l_n y)} = \int_{-\infty}^{\infty} \int_{-\infty}^{\infty} E_\phi(k,l) e^{i2\pi(kx+ly)} dkdl \quad \text{(A.5)}$$

where k and l is the wavenumber in the zonal and meridional direction. The second and third term is the discretized and continuous form of the inverse Fourier Transform. The corresponding spectral density estimate can equally be calculated from the squared coefficients:

$$E_\phi(k_n, l_m) = \frac{|a_{nm}|^2}{\Delta k \Delta l} \quad \text{(A.6)}$$

A common practice in oceanography is to obtain an isotropic 1D wavenumber spectra from a 2D wavenumber spectra for easy interpretation of the results in terms of the variance associated with each wavenumber. Technically, we want to preserve the area under the 2D spectrum such that

$$\int_{-\infty}^{\infty} \int_{-\infty}^{\infty} E_\phi(k,l) dkdl = \int_{-\infty}^{\infty} \int_{-\pi}^{\pi} k_r E_\phi(k_r, \theta) d\theta dk_r \quad \text{(A.7)}$$

where $k_r = \sqrt{k^2 + l^2}$ is the isotropic wavenumber and the extra k_r in the second integral is a geometric factor coming from the change of variables from catersian to polar coordinates. Assuming isotropy implies that $E_\phi(k_r, \theta) = E_\phi(k_r)$ and equation (A.7) becomes

$$\int_{-\infty}^{\infty} \int_{-\infty}^{\infty} E_\phi(k,l) dkdl = \int_{-\infty}^{\infty} k_r E_\phi(k_r) dk_r \quad \text{(A.8)}$$

The right-hand side of equation (A.8) is the 1D isotropic wavenumber spectral density of a 2D spatial datasets. A step by step mathematical description of isotropic averaging of a 2D wavenumber spectra to a 1D wavenumber spectra can be found in (Uchida et al., 2017).

A.3 Frequency - wavenumber spectra

The frequency-wavenumber spectra provide a way to estimate the variance associated with different oceanic motion as a function of their spatial and temporal scale. This type of spectra is used as a means to track propagating sinusoidal patterns in oceanography studies. Lets consider a 2D dataset $\phi(x,t)$ where x and t represents

space and time respectively such that $0 < x < X$ and $0 < t < T$. We can represent ϕ as a function of its Fourier transform as

$$\phi(x,t) = \sum_{n=-\infty}^{\infty} a_n e^{i2\pi f_n t} \quad \text{or} \quad \phi(x,t) = \sum_{m=-\infty}^{\infty} a_m e^{i2\pi k_m x} \tag{A.9}$$

where

$$f_n = \frac{n}{T} \quad \text{and} \quad k_m = \frac{m}{X} \tag{A.10}$$

By extension we can do this process in two dimensions to get :

$$\phi(x,t) = \sum_{n=-\infty}^{\infty} \sum_{m=-\infty}^{\infty} a_{nm} e^{i2\pi(f_n t + k_m x)} \tag{A.11}$$

The corresponding spectral density estimate can be calculated from the squared coefficients as

$$E(k_m, f_n) = \frac{|a_{nm}|^2}{\Delta k \Delta f} \tag{A.12}$$

A.4 Spectra Coherence

Spectra coherence provides information that is analogous to a correlation coefficient. It tells us whether two series are statistically linked at any specific frequency/wavenumber. Spectra coherence between two time-series is calculated based on the estimates of the cross spectra between the two time-series. The cross-spectrum, on the other hand, indicates the shared power between two time-series at each frequency/wavenumber. To illustrates these concepts mathematically, let's consider two time-series $\phi(t)$ and $\mu(t)$ such that $0 < t < T$. In terms of Fourier components, these time series can be written as

$$\phi(t) = \sum_{n=-\infty}^{\infty} a_n e^{i2\pi f_n t}, \tag{A.13}$$

$$\mu(t) = \sum_{n=-\infty}^{\infty} b_n e^{i2\pi f_n t} \tag{A.14}$$

The cross-spectrum, $C_{\psi\mu}(f_n)$ between ϕ & μ is defined as

$$C_{\psi\mu}(f_n) = \frac{\langle a_n^* b_n \rangle}{\Delta f} \tag{A.15}$$

and the spectra coherence, $S_{\psi\mu}(f)$ between the two time-series is estimated as

$$S_{\psi\mu}(f) = \frac{|C_{\psi\mu}(f)|^2}{C_{\phi\phi}(f) * C_{\mu\mu}(f)} \tag{A.16}$$

$S_{\psi\mu}(f)$ satisfy that $0 < S_{\psi\mu} < 1$ where 0 means no coherence and 1 means perfect coherence. $C_{\phi\phi}$ and $C_{\mu\mu}$ in equation (A.16) represents the autospectral density for ϕ and μ respectively and are defined.

$$C_{\phi\phi}(f_n) = E_{\psi}(f_n) = \frac{a_n^2}{\Delta f} \tag{A.17}$$

$$C_{\mu\mu}(f_n) = E_{\mu}(f_n) = \frac{b_n^2}{\Delta f} \tag{A.18}$$

A.5 Spectral flux

In this section, we present the mathematical description of the kinetic energy spectral flux. This flux is due to nonlinear terms in the momentum equation. In a simplified form, the momentum equation can be written as

$$\frac{\partial \mathbf{u}}{\partial t} = -\mathbf{u} \cdot \nabla \mathbf{u} \ + \ \mathbf{OT} \tag{A.19}$$

where $\mathbf{u}$ is the horizontal velocity field and $\mathbf{OT}$ represents other terms in the momentum equation. If we take the Fourier Transform of equation (A.19) then multiplied it by $\widehat{\mathbf{u}}^*$ (where $\widehat{}$ and * represents Fourier transform and its conjugate respectively), then we have

$$\widehat{\mathbf{u}}^* \cdot \frac{\partial \widehat{\mathbf{u}}}{\partial t} = -\widehat{\mathbf{u}}^* \cdot \widehat{[\mathbf{u} \cdot \nabla \mathbf{u}]} \ + \ \widehat{\mathbf{u}}^* \cdot OT \tag{A.20}$$

$$\frac{\partial (\frac{1}{2} \widehat{\mathbf{u}}^* \cdot \widehat{\mathbf{u}})}{\partial t} = -\widehat{\mathbf{u}}^* \cdot \widehat{[\mathbf{u} \cdot \nabla \mathbf{u}]} \ + \ \widehat{\mathbf{u}}^* \cdot OT \tag{A.21}$$

Equation (A.21) is the kinetic energy equation and can be rewritten as

$$\frac{\partial KE}{\partial t} = T_{KE} \; + \; \widehat{\mathbf{u}}^* \cdot OT \tag{A.22}$$

where the kinetic energy spectral density (KE) is defined as

$$KE = \frac{1}{2}\widehat{\mathbf{u}}^* \cdot \widehat{\mathbf{u}} \tag{A.23}$$

$$KE = \frac{1}{2}[\widehat{u}^* \cdot \widehat{u} \; + \; \widehat{v}^* \cdot \widehat{v}] \tag{A.24}$$

and the kinetic energy spectral flux (T_{KE}) is

$$T_{KE} = -\widehat{\mathbf{u}}^* \cdot [\widehat{\mathbf{u} \cdot \nabla \mathbf{u}}] \tag{A.25}$$

$$T_{KE} = -\widehat{u}^* \left(u\widehat{\frac{\partial u}{\partial x}} + v\frac{\partial u}{\partial y} \right) + \widehat{v}^* \left(u\widehat{\frac{\partial v}{\partial x}} + v\frac{\partial v}{\partial y} \right) \tag{A.26}$$

In equation (A.24) and (A.26), u and v represents the zonal and meridional velocity fields respectively, while x and y in equation (A.26) represents the distance between two velocity points in the zonal and meridional direction.

A.6 Spectral analysis approach

The spectra estimate in this thesis work is based mostly on two-dimensional fields of Sea Surface Height (SSH) and horizontal velocities (u, v) in different regions of the North Atlantic Ocean. The spectra densities are estimated following standard spectra analysis procedure and are also consistent with published spectra results. Below is the step-wise approach that was followed in this thesis.

1. **Define rectangular box over a region of interest**: In order to perform spectra analysis in a region, we define a rectangular box that is big enough to accommodate the scale of oceanic motion that is of interest to our study. For example in a 10° x 10° box, the highest wavelength that can be reliably resolved by spectra is 500km i.e approximate half of the box size. So, we can sufficiently resolve fine-scale and large scale dynamics up to 500km in a 10° x 10° box.

2. **Avoid islands or replace them with interpolated values**: Island are represented by big values or NaN in most oceanographic datasets. In some cases, our region of interest might include areas that contain small islands. If the island covers a very small fraction of the domain, one possible way to deal with such a case is to replace the values at the grid point corresponding to the island with an interpolated value. However, if the island covers a significant fraction, it is advisable to consider subdividing the domain to smaller boxes to avoid the island.

3. **Remove the mean and the trend from the time series**: In spectral analysis, it is customary to remove the mean and trend of the time series before the application of FFT. This is because, the Fourier transform of a linear trend puts energy into every possible frequency and this indicates that if you dont detrend your data, any residual trend will give you a red spectrum [1]. If the detrending is not properly done, it can distort the low-frequency component of the spectrum. In a 2D time series like ours, detrending can be implemented by fitting a plane to the time series or removing the trend in both axes of the datasets.

4. **Apply smoothing functions to time-series**: To increase the reliability of spectra results, we can decide to average many spectral results, apply window function directly to the time series or do both. A window is a smoothing function applied to finite observation to minimize leakage in the spectra domain i.e windowing reduces the transfer of energy from one spectral frequency to the neighboring frequencies. Short time series are discontinuous at the boundary and this discontinuity can introduce spectral leakage, because, discrete Fourier transform implicitly assumes that our record repeats again and again, so any discontinuity between the beginning and end of the record can create a step function. Windowing can be used to reduce the order of discontinuity at the boundary. When applied in the time/space domain, the window smoothly brings the values of at the boundary of a time series to zero and thereby making the time series periodic in nature. Several existing window functions can be used depending on the dataset. In this thesis work, given our 2D spatial dataset, we used in different cases Hanning and Tukey windowing to increase the statistical reliability of our spectral estimate.

5. **Compute the Fourier transforms**: Fourier components of a time series can be estimated by applying Fast Fourier Transforms to the time. FFT is readily implemented in may statistical software such as Python, MATLAB, etc. From the Fourier components, we can then calculate the spectral density by taking the square of the components then normalizing by the size of the time series.

[1] A red spectrum is a spectrum whose spectral density decreases with increasing frequency

The implementation of this spectra method for estimating spectral density, frequency-wavenumber spectra, spectra coherence and spectra flux have documented and can be found on this GitHub repository [2]

In order to show the importance of detrending and windowing on the spectral estimate, we present in figure (A.1), a two dimensional map of (a) sea surface height (raw SSH) (b) SSH data detrended in both direction (c) SSH data multiplied by a Tukey widow (c) SSH data detrended in both axises and also multiplied by a Tukey window. The spectra estimate for these different forms of SSH dataset is presented in figure (A.2). The spectra of the raw SSH field differ significantly from the remaining two spectra. The difference between the "detrend + window" spectra and the "window" is due to the higher variance at high wavenumbers in the later. The impact of removing trends is to avoid the distortion of the spectral density, particularly at low wavenumbers. This is evident in the shape of the "windowed SSH" spectra. The peak of this spectra coincides with the lowest wavenumber. This shouldn't be because the lowest wavenumber corresponds to the largest wavelength in the domain and can not have the highest variance due to poor sampling at this scale. So this shows how not detrending introduces artificial energy at the lowest wavenumber.

[2]https://github.com/adeajayi-kunle/PowerSpec/blob/master/PowerSpec.py

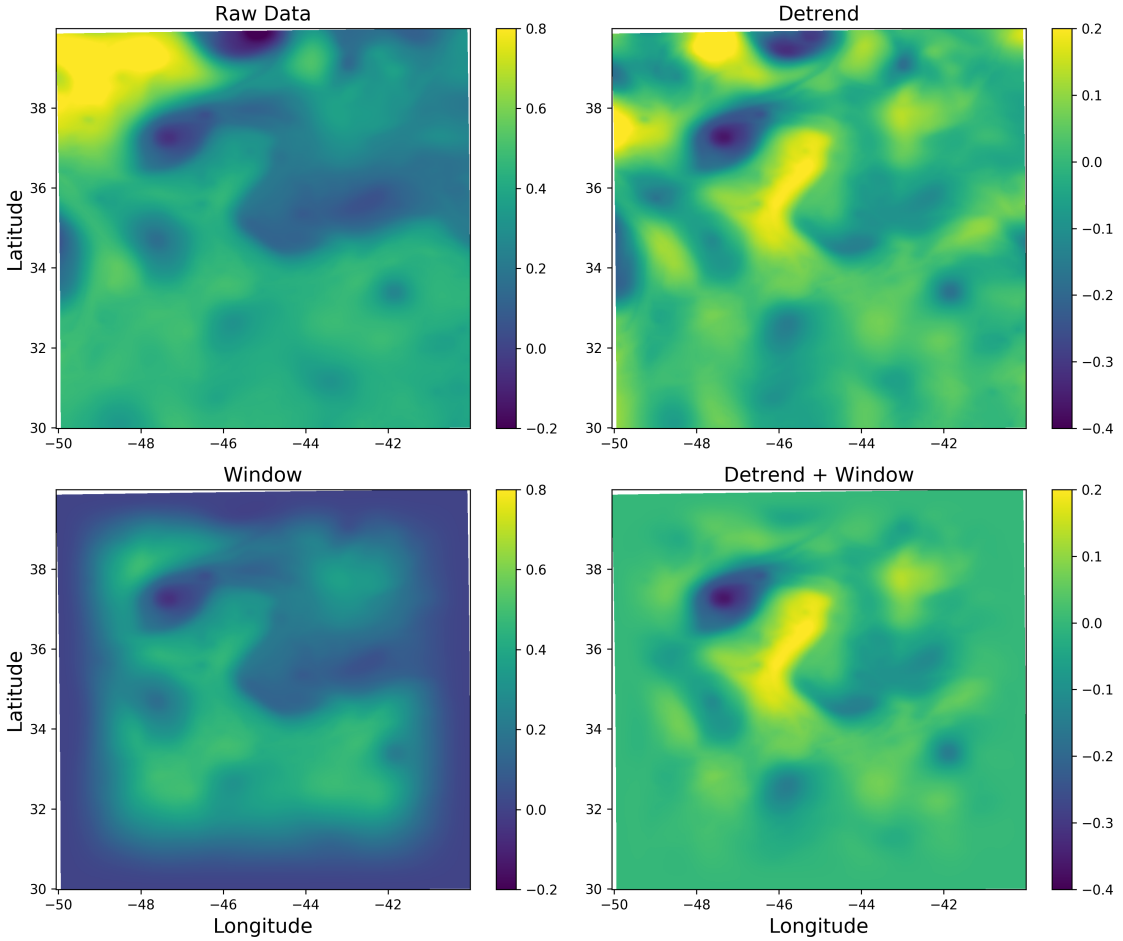

Figure A.1: Snapshot of sea surface height (SSH) (a) raw data (b) data multiplied by Tukey window and (c) data with trend removed and also multiplied by Tukey window.

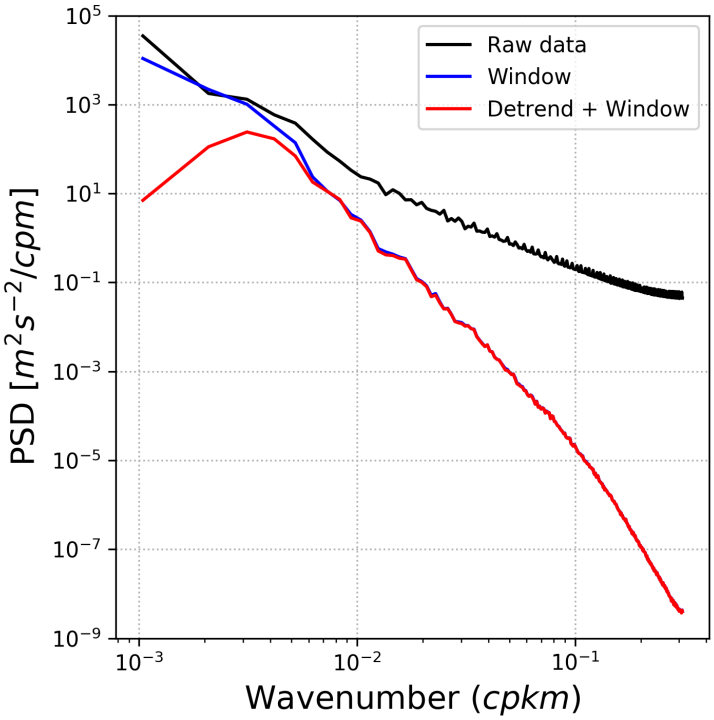

Figure A.2: Power sepctral density estimated using raw SSH data and preconditioned dataset.

Appendix B

Estimation of OSMOSIS Horizontal velocity gradients

This Appendix presents a short description of horizontal velocity gradient computation from OSMOSIS five points mooring array. The gradient estimate is based on a finite difference method, FMD (Bryden and Fofonoff (1977)), which is defined as

$$\frac{\partial Q}{\partial d} = \frac{1}{N}\sum_{i=1}^{N}\left(\frac{Q_c - Q_i}{d_c - d_i}\right) \tag{B.1}$$

In equation (B.1), Q is any scalar quantity, d is the zonal or meridional position of the moorings and subscripts c and i denote the center mooring and the neighboring moorings respectively. From these gradients we diagnosed the vorticity (ζ), strain-rate (α) and divergence (δ) as

$$\zeta = \frac{\partial v}{\partial x} - \frac{\partial u}{\partial y} \tag{B.2}$$

$$\delta = \frac{\partial u}{\partial x} + \frac{\partial v}{\partial y} \tag{B.3}$$

$$\alpha = \left[\left(\frac{\partial u}{\partial x} - \frac{\partial v}{\partial y}\right)^2 + \left(\frac{\partial v}{\partial x} + \frac{\partial u}{\partial y}\right)^2\right]^{1/2} \tag{B.4}$$

where u and v are the zonal and meridional velocity fields while x and y are the zonal and meridional distance between two moorings. The FDM of gradient estimation was validated by comparing the estimate of its vorticity with the vorticity values computed using the Stokes formula (Eq. B.5);

$$\zeta = (\nabla \times \mathbf{u}) \cdot \hat{k} = \frac{1}{A} \oint \mathbf{u}_h \cdot d\mathbf{l} \tag{B.5}$$

with A being the area enclosed by the path, $\mathbf{u}_h$ the horizontal velocity, and d$\mathbf{l}$ the differential pointing in the direction of the closed path.

Bibliography

Ajayi, A., Le Sommer, J., Chassignet, E., Molines, J.M., Xu, X., Albert, A., Cosme, E., 2019. Spatial and Temporal Variability of North Atlantic Eddy Field at Scale less than 100km. In preparation for Journal of Ocean Modelling .

Alice, M., Joel, H., Penny, H., Stuart, C., Adam, B., Andrew, C., 2015. The North Atlantic subpolar circulation in an eddy-resolving global ocean model. Journal of Marine Systems 142, 126–143. doi:http://dx.doi.org/10.1016/j.jmarsys.2014.10.007.

Aluie, H., Hecht, M., Vallis, G.K., 2017. Mapping the Energy Cascade in the North Atlantic Ocean: The Coarse-graining Approach. J. Phys. Oceanogr. , 225–244doi:10.1175/JPO-D-17-0100.1.

Amores, A., Jorda, G., Arsouze, T., Le Sommer, J., 2018. Up to What Extent Can We Characterize Ocean Eddies Using Present-Day Gridded Altimetric Products? Journal of Geophysical Research: Oceans 123.

Antonia, R.A., Shafi, H.S., Zhu, Y., 1996. A note on the vorticity spectrum. Physics of Fluids 8, 2196.

Arbic, B., Flierl, G., 2004. Baroclinically unstable geostrophic turbulence in the limits of strong and weak bottom Ekman friction: application to mid-ocean eddies. J. Phys. Oceanogr. 34, 22572273.

Arbic, B.K., Mitrovica, J.X., MacAyeal, D.R., Milne, G.A., 2008. On the factors behind large Labrador Sea tidesduring the last glacial cycle and the potential implications for Heinrich events. Paleoceanography 23.

Arbic, B.K., Polzin, K.L., Scott, R.B., Richman, J.G., Shriver, J.F., 2013. On Eddy Viscosity, Energy Cascades, and the Horizontal Resolution of Gridded Satellite Altimeter Products. J. Phys. Oceanogr. 43, 283–300. doi:10.1175/JPO-D-11-0240.1.

Balwada, D., Shafer, S., Ryan, A., 2018. Submesoscale vertical velocities enhance tracer subduction in an idealized Antarctic Circumpolar Current. Geophysical Research Letters 45, 97909802. doi:https://doi.org/10.1029/2018GL079244.

Barkan, R., Winters, K.B., McWilliams, J.C., 2017. Stimulated Imbalance and the Enhancement of Eddy Kinetic Energy Dissipation by Internal Waves. J. Phys. Oceanogr. 47, 181–198.

Bates, M., Tulloch, R., Marshall, J., Ferrari, R., 2014. Rationalizing the Spatial Distribution of Mesoscale Eddy Diffusivity in Terms of Mixing Length Theory. Journal of Physical Oceanography 44, 1523 – 1540.

Boccaletti, G., Ferrari, R., Fox-Kemper, B., 2007. Mixed Layer Instabilities and Restratification. Journal of Physical Oceanography 37, 2228 – 2250.

Bower, A.S., Hogg, N., 1996. Structure of the Gulf Streamand its recirculations at 558W. J. Phys. Oceanogr. 26, 10021022. doi:10.1175/1520-0485(1996)026,1002:SOTGSA.2.0.CO;2.

Brannigan, L., Marshall, D.P., Naveira-Garabato, A., George Nurser, A.J., 2015. The seasonal cycle of submesoscale flows. Ocean Modelling .

Brüggemann, N., Eden, C., 2015. Routes to Dissipation under Different Dynamical Conditions. J. Phys. Oceanogr. 45, 2149–2168. doi:10.1175/JPO-D-14-0205.1.

Bryan, F.O., 2008. Introduction: Ocean Modeling-Eddy or Not. Gophysical Mon. Series 177, 1 – 4.

Bryden, H.L., Fofonoff, N.P., 1977. Horizontal divergence and vorticity estimates from velocity and temperature measurements in the MODE region. J. Phys. Ocean. 7, 329 – 337.

Buckingham, C.E., Natasha, L., Stephen, B., Tom, R., Alan, G., Julien Le, S., Adekunle O., A., Naveira Garabato, A.C., 2019. The contribution of surface and submesoscale processes to turbulence in the open ocean surface boundary layer. Submitted to JAMES. .

Buckingham, C.E., Naveira Garabato, A.C., Thompson, A.F., Brannigan, L., Lazar, A., Marshall, D.P., George Nurser, A.J., Damerell, G., Heywood, K.J., Belcher, S.E., 2016. Seasonality of submesoscale flows in the ocean surface boundary layer. Geophys. Res. Lett. doi:10.1002/2016GL068009.

Buhler, O., McIntyre, M., 2005. Wave capture and wave-vortex duality. J. Fluid Mech. 534, 6795.

Callies, J., Ferrari, R., Klymak, J.M., Gula, J., 2015a. Seasonality in submesoscale turbulence. Nature Communication 6, 6862.

Callies, J., Flierl, G., Ferrari, R., Fox-Kemper, B., 2015b. The role of mixed-layer instabilities in submesoscale turbulence. J. Fluid Mech. 788, 5 – 41.

Capet, X., Campos, E.J., Paiva, A.M., 2008a. Submesoscale activity over the Argentinian shelf. Geophysical Research Letters 35, 2 – 6.

Capet, X., Klein, P., Hua, B.L., Lapeyre, G., McWilliams, J.C., 2008b. Surface kinetic energy transfer in surface quasi-geostrophic flows. Journal of Fluid Mechanics 604, 165 – 174.

Capet, X., Mcwilliams, J.C., Molemaker, M.J., Shchepetkin, A.F., 2008c. Mesoscale to Submesoscale Transition in the California Current System. Part I: Flow Structure, Eddy Flux, and Observational Tests. J. Phys. Oceanogr. 38, 29 – 43. doi:10.1175/2007JPO3671.1.

Capet, X., Mcwilliams, J.C., Molemaker, M.J., Shchepetkin, A.F., 2008d. Mesoscale to Submesoscale Transition in the California Current System. Part II: Frontal Processes. J. Phys. Oceanogr. 38, 44 – 64. doi:10.1175/2007JPO3672.1.

Capet, X., Mcwilliams, J.C., Molemaker, M.J., Shchepetkin, A.F., 2008e. Mesoscale to Submesoscale Transition in the California Current System. Part III: Energy Balance and Flux. J. Phys. Oceanogr. 38, 2256 – 2269. doi:10.1175/2008JPO3810.1.

Charney, J., 1971. Geostrophic turbulence. Journal of Atmospheric Sciences 28, 1087–1095.

Chassignet, E.P., Xu, X., 2017. Impact of Horizontal Resolution (1/12 to 1/50) on Gulf Stream Separation, Penetration, and Variability. Journal of Physical Oceanography 47, 1999 – 2021.

Chelton, D.B., DeSzoeke, R., Schlax, M., El Naggar, K., Siwertz, N., 1998. Geographical Variability of the First Baroclinic Rossby Radius of Deformation. Journal of Physical Oceanography 28, 433 – 460.

Chelton, D.B., Schlax, M.G., Samelson, R.M., 2011. Global observations of nonlinear mesoscale eddies. Progress in Oceanography 91, 167 – 216.

Chelton, D.B., Schlax, M.G., Samelson, R.M., DeSzoeke, R., 2007. Global observations of large oceanic eddies. Geophysical Research Letters 34, 1 – 5.

Chi, X., Xiaoming, Z., Xiao-Dong, S., 2016. Work done by atmospheric windson mesoscale ocean eddies. Geo-phys. Res. Lett. 43, 1217412180. doi:doi:10.1002/2016GL071275.

Chris, G., 2003. Internal Tides and Ocean Mixing. Science 301, 1858–1859. doi:DOI:10.1126/science.1090002.

Chris, W., 2016. Does the wind systematically energize or damp ocean eddies? Geophys. Res. Lett. 43, 1253812542,. doi:doi:10.1002/2016GL072215.

Crueger, T., Roeckner, E., Raddatz, T., Schnur, R., Wetzel, P., 2008. Ocean dynamics determine the response of oceanic CO2 uptake to climate change. Clim. Dyn. 31, 151–168. doi:10.1007/s00382-007-0342-x.

Danilov, S., Gurarie, D., 2002. Rhines scale and spectra of the β-plane turbulence with bottom drag. Physical Review E - Statistical Physics, Plasmas, Fluids, and Related Interdisciplinary Topics 65, 5 – 7.

Danioux, E., Vanneste, J., Klein, P., Sasaki, H., 2012. Spontaneous inertia-gravity-wave generation by surface-intensified turbulence. Journal of Fluid Mechanics 699, 153173.

D'Asaro, E.A., 1985. The Energy Flux from the Wind to Near-Inertial Motions in the Surface Mixed Layer. J. Phys. Oceanogr. 15, 1043 1059.

Dascaliuc, R., Grujić, Z., 2013. Coherent Vortex Structures and 3D Enstrophy Cascade. Communications in Mathematical Physics 317, 547 – 561.

Dewar, W., Jamet, Q., Ajayi, A., Le Sommer, J., Penduff, T., Hogg, A., 2019. On Energy Cascades in General Flows. Submitted to JAMES .

Ducet, N., Traon, P.L., 2001. A comparison of surface eddy kinetic energy and Reynolds stresses in the Gulf Stream and the Kuroshio Current systems from merged TOPEX/Poseidon and ERS-1/2 altimetric data. J. Geophys. Res. 106, 16,603–16,622.

Ducousso, N., Le Sommer, J., Molines, J.M., Bell, M., 2017. Impact of the symmetric instability of the computational kind at mesoscale- and submesoscale-permitting resolutions. Ocean Modelling 120.

Dufau, C., Orsztynowicz, M., G., D., R., M., P.Y., L.T., 2016. Mesoscale resolution capability of altimetry: Present and future. J. Geophys. Res. Oceans 121, 1–18. doi:10.1175/JPO-D-11-0240.1.

Dussin, R., Barnier, B., Brodeau, L., Molines, J.M., 2018. The making of the DRAKKAR forcing set DFS5. Drakker .

Eden, C., 2007. Eddy length scales in the North Atlantic Ocean. Journal of Geophysical Research 112, C06004.

Escudier, R., Renault, L., Pascual, A., Brasseur, P., Chelton, D.B., Beuvier, J., 2016. Eddy properties in theWestern Mediterranean Sea from satellite altimetry and a numerical simulation. Journal of Geophysical Research 121, 3990 – 4006.

Faghmous, J.H., Frenger, I., Yao, Y., Warmka, R., Lindell, A., Kumar, V., 2015. A daily global mesoscale ocean eddy dataset from satellite altimetry. Scientific Data 2, 1 – 16.

Ferrari, R., Wunsch, C., 2009. Ocean Circulation Kinetic Energy: Reservoirs, Sources, and Sinks. Annu. Rev. Fluid Mech. 41, 253–282. doi:10.1146/annurev.fluid.40.111406.102139.

Flierl, G., 1978. Models of vertical structure and the calibration of two-layer models. Dyn. Atmos. Oceans. 2, 341381.

Fox-Kemper, B., Ferrari, R., Hallberg, R., 2008. Parameterization of mixed layer eddies. Part I: theory and diagnosis. . Journal of Physical Oceanography 6, 1145 – 1165.

Fresnay, S., Ponte, A.L., Le Gentil, S., Le Sommer, J., 2018. Reconstruction of the 3-D Dynamics From Surface Variables ina High-Resolution Simulation of North Atlantic. Journal of Geophysical Research: Oceans 123.

Fu, L.L., Chelton, D.B., Le Traon, P.Y., Morrow, R., 2010. Eddy Dynamics From Satellite Altimetry. Oceanography 23, 14–25.

Fu, L.L., Ferrari, R., 2008. Observing oceanic submesoscale processes from space. Eos, Transactions, American Geophysical Union 48, 488.

Fu, L.L., Flierl, G., 1980. Nonlinear energy and enstrophy transfers in a realistically stratified ocean. Dyn. Atmos. Oceans 4, 219246.

Fu, L.L., Ubelmann, C., 2014. On the transition from profile altimeter to swath altimeter for observing global ocean surface topography. J. Atmos. Oceanic Technol 31, 560 568.

Gertz, A., Straub, D.N., 2009. Near-Inertial Oscillations and the Damping of Midlatitude Gyres: A Modeling Study. J. Phys. Oceanogr. 39, 2338–2350. doi:10.1175/2009jpo4058.1.

Gill, A.E., Green, J.S.A., Simmons, A.J., 1974. Energy partition in the large-scale ocean circulation and the produc- tion of mid-ocean eddies. Deep-Sea Res. 21, 499528.

Gille, S., Yale, M., Sandwell, D., 2000. Global correlation of mesoscale ocean variability with seafloor roughness from satellite altimetry. Geophys. Res. Lett. 27, 12511254.

Gula, J., Molemaker, J., McWilliams, J.C., 2016. Submesoscale Dynamics of a Gulf Stream Frontal Eddy in the South Atlantic Bight. Journal of Physical Oceanography 46, 305 – 325.

Held, I.M., Pierrehumbert, R.T., Garner, S.T., Swanson, K.L., 1995. Surface quasi-geostrophic dynamics. Journal of Fluid Mechanics 282, 1 – 20.

Hoskins, B., Bretherton, F., 1972. Atmospheric frontogenesis models: mathematical formulation and solution. J. Atmos. Sci. 29, 1137.

Hua, B., McWilliams, J., Owens, W., 1986. An objective analysis ofthe POLYMODE local dynamics experiment II: stream function and potential vorticity. . Phys. Oceanogr. 16, 506522.

Jacques, V., Pierre, S., Juliette, L., Jocelyne, N., Nathalie, S., Amandine, G., Nicolas, P., Sophie, C.F., Rashmi, S., R. M., G., Murthy, D.V.A.R., James, R., David, G., Ananda, P., Frdrique, R., P. K., G., 2015. The SARAL/AltiKa Altimetry Satellite Mission. Marine Geodesy 38, 2–21. doi:10.1080/01490419.2014.1000471.

Khatri, H., Sukhatme, J., Kumar, A., Verma, M.K., 2018. Surface Ocean Enstrophy, Kinetic Energy Fluxes and Spectra from Satellite Altimetry. J. Geophys. Res. Ocean. doi:10.1029/2017JC013516.

Kjellsson, J., Zanna, L., 2017. The Impact of Horizontal Resolution on Energy Transfers in Global Ocean Models. Fluids 2, 45. doi:10.3390/fluids2030045.

Klein, P., Bach, L.H., Xavier, C., 2003. Emergence of cyclonic structures due to the interaction between nearinertial oscillations and mesoscale eddies. Quaterly Journal ofthe Royal Meteorologicial Society 129, 1 – 20. doi:10.1029/2018EA000492.

Klein, P., Hua, B.L., Lapeyre, G., Capet, X., Le Gentil, S., Sasaki, H., 2008. Upper Ocean Turbulence from High-Resolution 3D Simulations. Journal of Physical Oceanography 38, 1748 – 1763.

Klein, P., Isem-Fontanet, J., Lapeyre, G., Roullet, G., Danioux, E., Chapron, B., Le Gentil, S., Sasaki, H., 2009. Diagnosis of vertical velocities in the upper ocean from high resolution sea surface height. Geophys. Res. Lett. 36, 1–5. doi:10.1029/2009GL038359.

Klein, P., Lapeyre, G., Siegelman, L., Qiu, B., Fu, L.L., Torres, H., Su, Z., Menemenlis, D., Le Gentil, S., 2019. Ocean-Scale Interactions From Space. Earth Sp. Sci. 6, 795–817. doi:10.1029/2018EA000492.

Klocker, A., Abernathey, R., 2014. Global Patterns of Mesoscale Eddy Properties and Diffusivities. Journal of Physical Oceanography 44, 1030 – 1046.

Klocker, A., Marshall, D.P., Keating, S.R., Read, P.L., 2016. A regime diagram for ocean geostrophic turbulence. Journal of the Royal Meteorological Society .

Kraichnan, R.H., Montgomery, D., 1980. Two-dimensional turbulence. Reports on Progress in Physics 43, 547 – 619.

Lahaye, N., Gula, J., Roullet, G., 2019. Sea Surface Signature of Internal Tides. Geophys. Res. Lett. 46, 3880–3890. doi:10.1029/2018GL081848.

Lapeyre, G., Klein, P., 2006. Dynamics of the Upper Oceanic Layers in Terms of Surface Quasigeostrophy Theory. J. Phys. Oceanogr. 36, 165–176. doi:10.1175/JPO2840.1.

Le Sommer, J., Molines, J.M., Albert, A., Brodeau, L., Ajayi, A.O., Gomez Navarro, L., Cosme, E., Penduff, T., Barnier, B., Verron, J., Brasseur, P., Rampal, P., Chassignet, E., 2019. NATL60: A North Atlantic ocean circulation model dataset based on NEMO for preparing SWOT altimeter mission, in prep. In preparation for Geoscientific Model Development. .

Le Traon, P.Y., 1993. Comment on Mesoscale variability in the Atlantic ocean from Geosat altimetry and WOCE high resolu- tion numerical modeling by D. Stammer and C.W. Bning. Journal of Physical Oceanography 23, 2729 2732.

Le Traon, P.Y., Klein, P., Hua, B.L., Dibarboure, G., 2008. Do altimeter data agree with interior or surface quasi- geostrophic theory? Journal of Physical Oceanography 5, 1137 1142.

Le Traon, P.Y., Rouquet, M.C., Boissier, C., 1990. Spatial scales of mesoscale variability in the North Atlantic as deduced from Geosat data. Journal of Geophysical Research 95, 20267.

McWilliams, J.C., 1985. Submesoscale, Coherent Vortices in the Ocean. Reviews of Geophysics 23, 165 – 182.

McWilliams, J.C., 2016. Submesoscale currents in the ocean. Proc. R. Soc. A 472, 20160117.

Mensa, J.A., Garraffo, Z., Griffa, A., Ozgokmen, T.M., Haza, A., Veneziani, M., 2013. Seasonality of the submesoscale dynamics in the Gulf Stream region. Ocean Dynamics 63, 923 – 941.

Molemaker, M., McWilliams, J., Capet, X., 2010. Balanced and unbalanced routes to dissipation in an equili- brated eddy flow. J. Fluid Mech. 654, 3563.

Molemaker, M., McWilliams, J., Yavneh, I., 2005. Baroclinic instability and loss of balance. J. Phys. Oceanogr. 35, 15051517.

Morris, S.C., Foss, J.F., 2005. Vorticity spectra in high Reynolds number anisotropic turbulence. Physics of Fluids 17, 1 – 4.

Moum, J.N., 1996. Energy-containing scales of turbulence in the ocean thermocline. Journal of Geophysical Research: Oceans 101, 14095 – 14109.

Müller, M., Arbic, B.K., Richman, J.G., Shriver, J.F., Kunze, E.L., Scott, R.B., Wallcraft, A.J., Zamudio, L., 2015. Toward an internal gravity wave spectrum in global ocean models. Geophys. Res. Lett. 42, 34743481.

Muller, P., 1976. Diffusion of momentum and mass by internal gravity waves. J. Fluid Mech. 77, 789823.

Nagai, T., Tandon, A., Kunze, E., Mahadevan, A., 2015. Spontaneous Generation of Near-Inertial Waves by the Kuroshio Front. J. Phys. Oceanogr. 45, 2381–2406. doi:10.2139/ssrn.2906136.

Naveira, G., Polzin, K., King, B., Heywood, K., Visbeck, M., 2004. Widespread intense turbulent mixing in the Southern Ocean. Science 303, 210233.

Nikurashin, M., Ferrari, R., 2010. Radiation and Dissipation of Internal Waves Generated by Geostrophic Motions Impinging on Small-Scale Topography: Theory. J. Phys. Oceanogr. 40, 2025–2042. doi:10.1175/2010JPO4315.1.

Nikurashin, M., Vallis, G.K., Adcroft, A., 2013. Routes to energy dissipation for geostrophic flows in the Southern Ocean. Nat. Geosci. 6, 48–51. doi:10.1038/ngeo1657.

Ohkitani, K., 1991. Wavenumber space dynamics of enstrophy cascade in a forced two-dimensional turbulence. Physics of Fluids A 3, 1598 – 1611.

Painter, S.C., Pidcock, R.E., Allen, J.T., 2010. A mesoscale eddy driving spatial and temporal heterogeneity in the productivity of the euphotic zone of the northeast Atlantic. Deep Sea Res. Part II:Top. Stud. Oceanogr. 57, 1281–1292. doi:10.1175/jpo-d-18-0253.1.

Qiu, B., Chen, S., Klein, P., Sasaki, H., Sasai, Y., 2014. Seasonal Mesoscale and Submesoscale Eddy Variability along the North Pacific Subtropical Countercurrent. Journal of Physical Oceanography 44, 3079 – 3098.

Qiu, B., Chen, S., Klein, P., Wang, J., Torres, H., Fu, L.L., Menemenlis, D., 2018. Seasonality in Transition Scale from Balanced to Unbalanced Motions in the World Ocean. J. Phys. Oceanogr. , JPO–D–17–0169.1.

Qiu, B., Nakano, T., Chen, S., Klein, P., 2017. Submesoscale transition from geostrophic flows to internal waves in the northwestern Pacific upper ocean. Nat. Commun. 8, 1–10. doi:10.1038/ncomms14055.

Renault, L., Molemaker, M.J., Mcwilliams, J.C., Shchepetkin, A.F., Lemarié, F., Chelton, D., Illig, S., Hall, A., 2016. Modulation of wind work by oceanic current interaction with the atmosphere. J. Phys. Oceanogr. 46, 1685–1704. doi:10.1175/JPO-D-15-0232.1.

Rhines, P.B., 1975. Waves and turbulence on a beta-plane. Journal of Fluid Mechanic 69, 417 443.

Rhines, P.B., 1979. Geostrophic turbulence. Annual Review of Fluid Mechanics 11, 401 441.

Richardson, P.L., 1985. Average velocity and transport of the Gulf Stream near 558W. J. Mar. Res. 43, 83111. doi:10.1357/002224085788437343.

Rocha, C.B., Gille, S.T., Chereskin, T.K., M., D., 2016. Seasonality of submesoscale dynamics in the Kuroshio Extension. Geophysical Research Letters 43, 11304 – 11311.

Rocha, C.B., Wagner, G.L., Young, W.R., 2018. Stimulated generation: Extraction of energy from balanced flow by near-inertial waves. J. Fluid Mech. 847, 417–451.

Salmon, R., 1980. Baroclinic instability and geostrophic turbulence. Geophys. Astrophys. Fluid Dyn. 15, 167211.

Salmon, R., 1998. Lectures on Geophysical Fluid Dynamics. JNew York: Oxford Univ. Press. 142, 378 pp.

Sasaki, H., Klein, P., 2012. SSH Wavenumber Spectra in the North Pacific from a High-Resolution Realistic Simulation. J. Phys. Oceanogr. 42, 1233–1241. doi:10.1175/JPO-D-11-0180.1.

Sasaki, H., Klein, P., Qiu, B., Sasai, Y., 2014. Impact of oceanic scale- interactions on the seasonal modulation of ocean dynamics by the atmosphere. Nature Communication 5, 5636.

Sasaki, H., Klein, P., Sasai, Y., Qiu, B., 2017. Regionality and seasonality of submesoscale and mesoscale turbulence in the North Pacific Ocean. Ocean Dynamics 67, 1195 – 1216.

Schlösser, F., Eden, C., 2007. Diagnosing the energy cascade in a model of the North Atlantic. Geophys. Res. Lett. 34, 1–5. doi:10.1029/2006GL027813.

Scott, R.B., 2001. Evolution of energy and enstrophy containing scales in decaying, two-dimensional turbulence with friction. Physics of Fluids 13, 2739 – 2742.

Scott, R.B., Arbic, B.K., 2007. Spectral Energy Fluxes in Geostrophic Turbulence: Implications for Ocean Energetics. J. Phys. Oceanogr. 37, 673–688. doi:10.1175/JPO3027.1.

Scott, R.B., Wang, F., 2005. Direct Evidence of an Oceanic Inverse Kinetic Energy Cascade from Satellite Altimetry. J. Phys. Oceanogr. 35, 1650–1666. doi:10.1175/JPO2771.1.

Sen, A., Scott, R., Arbic, B., 2008. Global energy dissipation rate of deep-ocean low-frequency flows by quadratic bottom boundary layer drag: computations from current-meter data. Geophys. Res. Lett. 35, L09606.

Shakespeare, C.J., Hogg, A.M., 2017. Spontaneous Surface Generation and Interior Amplification of Internal Waves in a Regional-Scale Ocean Model. J. Phys. Oceanogr. 47, 811–826.

Shakespeare, C.J., Taylor, J.R., 2014. The spontaneous generation of inertia-gravity waves during frontogenesis forced by large strain: Theory. J. Fluid Mech. 757, 817 – 853.

Shcherbina, A.Y., D'Asaro, E.A., Lee, C.M., Klymak, J.M., Molemaker, M.J., McWilliams, J.C., 2013. Statistics of vertical vorticity, divergence, and strain in a developed submesoscale turbulence field. Geophys. Res. Lett. 40, 47064711. doi:10.1002/grl.50919.

Smith, S., Vallis, G., 2002. The Scales and Equilibration of Mid Ocean Eddies: Forced Dissipative Flow. J. Phys. Oceanogr. 32, 1699–1720.

Soufflet, Y., Marchesiello, P., Lemari, F., Jouanno, J., Capet, X., Debreu, L., Benshila, R., 2016. On effective resolution in ocean models. Ocean Model. 98, 36–50. doi:10.1016/j.ocemod.2015.12.004.

St. Laurent, L.C., Garrett, C., 2002. The role of internal tides in mixing the deep ocean. J. Phys. Oceanogr. 32, 2882–2899. doi:10.1175/1520-0485(2002)032<2882:TROITI>2.0.CO;2.

Stammer, D., 1997. Global characteristics of ocean variability estimated from regional TOPEX/ POSEIDON altimeter measurements. Journal of Physical Oceanography 27, 1743 – 1769.

Stammer, D., Böning, C.W., 1992. Mesoscale Variability in the Atlantic Ocean from Geosat Altimetry and WOCE High-Resolution Numerical Modeling.

Su, Z., Jinbo, W., Patrice, K., Andrew, T., Dimitris, M., 2018. Ocean submesoscales as a key component of the global heat budget. Nature Communications 9:775, 1 8. doi:https://doi.org/10.1038/s41467-018-02983-w.

Thomas, L., 2008. Submesoscale processes and dynamics. Geophysical Monograph Series 177. doi:https://doi.org/10.1029/177GM04.

Thomas, L., Ferrari, R., 2008. Friction, Frontogenesis, and the Stratification of the Surface Mixed Layer. J. Phys. Oceanogr. 38, 2501–2518. doi:10.1175/2008JPO3797.1.

Thomas, L.N., 2017. On the modifications of near-inertial waves at fronts: implications for energy transfer across scales. Ocean Dyn. 67, 1335–1350.

Thompson, A., Lazar, A., Buckingham, C., Naveira Garabato, A., Damerell, G.M., Heywood, K.J., 2016. Open-Ocean Submesoscale Motions: A Full Seasonal Cycle of Mixed Layer Instabilities from Gliders. Journal of Physical Oceanography 46, 1285 – 1307.

Torres, H.S., Klein, P., Menemenlis, D., Qiu, B., Su, Z., Wang, J., Chen, S., Fu, L.L., 2018. Partitioning Ocean Motions Into Balanced Motions and Internal Gravity Waves: A Modeling Study in Anticipation of Future Space Missions. J. Geophys. Res. Ocean. doi:10.1029/2018JC014438.

Tulloch, R., John, M., Chris, H., 2011. Scales, Growth Rates, and Spectral Fluxes of Baroclinic Instability in the Ocean. J. Phys. Oceanogr. 41, 1057–1076. doi:10.1175/2011JPO4404.1.

Uchida, T., Abernathey, R., Smith, S., 2017. Seasonality of eddy kinetic energy in an eddy permitting global climate model. Ocean Modelling 118, 41 – 58.

Uppala, S.M., Kållberg, P.W., Simmons, A.J., Andrae, U., da Costa Bechtold, V., Fiorino, M., Gibson, J.K., Haseler, J., Hernandez, A., Kelly, G.A., Li, X., Onogi, K., Saarinen, S., Sokka, N., Allan, R.P., Andersson, E., Arpe, K., Balmaseda, M.A., Beljaars, A.C., van de Berg, L., Bidlot, J., Bormann, N., Caires, S., Chevallier, F., Dethof, A., Dragosavac, M., Fisher, M., Fuentes, M., Hagemann, S., Hólm, E., Hoskins, B.J., Isaksen, L., Janssen, P.A., Jenne, R., McNally, A.P., Mahfouf, J.F., Morcrette, J.J., Rayner, N.A., Saunders, R.W., Simon, P., Sterl, A., Trenberth, K.E., Untch, A., Vasiljevic, D., Viterbo, P., Woollen, J., 2005. The ERA-40 re-analysis. Q. J. R. Meteorol. Soc. 131, 2961–3012. doi:10.1256/qj.04.176.

Vergara, O., Rosemary, M., Marie-Isabelle, P., Dibarboure, G., Clement, U., 2019. Revised Global Wave Number Spectra From Recent Altimeter Observations. Journal of Geophysical Research : Oceans doi:https://doi.org/10.1029/2018JC014844.

Vic, C., Naveira Garabato, A.C., Green, J.A., Waterhouse, A.F., Zhao, Z., Melet, A., de Lavergne, C., Buijsman, M.C., Stephenson, G.R., 2019. Deep-ocean

mixing driven by small-scale internal tides. Nat. Commun. 10. doi:10.1038/s41467-019-10149-5.

Wunsch, C., 2007. The past and future ocean circulation from a contemporary perspective. Geophys. Monogr. Ser. 173, 53–74. doi:10.1029/173GM06.

Wunsch, C., Ferrari, R., 2004. Vertical mixing, energy, and the general circulation of the oceans. Annu. Rev. Fluid Mech. 36, 281 – 314.

Xu, Y., Fu, L.L., 2011. Global Variability of the Wavenumber Spectrum of Oceanic Mesoscale Turbulence. J. Phys. Oceanogr. 41, 802–809. doi:10.1175/2010JPO4558.1.

Yu, X., Naveira Garabato, A.C., Martin, A.P., Buckingham, C.E., Brannigan, L., Su, Z., 2019. An Annual Cycle of Submesoscale Vertical Flow and Restratification in the Upper Ocean. J. Phys. Oceanogr. 49, 1439–1461. doi:10.1175/jpo-d-18-0253.1.